

TWO-DIMENSIONAL MATERIALS: FROM BERRY CURVATURE
TO WRAPPING A MICROSPHERE

A Dissertation

Presented to the Faculty of the Graduate School
of Cornell University

In Partial Fulfillment of the Requirements for the Degree of
Doctor of Philosophy

by

Kathryn Lorraine McGill

August 2018

© 2018 Kathryn Lorraine McGill

TWO-DIMENSIONAL MATERIALS: FROM BERRY CURVATURE TO WRAPPING A MICROSHERE

Kathryn Lorraine McGill, Ph. D.

Cornell University 2018

The study of atomically-thin, truly two-dimensional (2D) materials has morphed into its own field since the experimental isolation of graphene and similar 2D materials in 2005. Graphene, as a single layer of carbon atoms with a unique band structure, and monolayer molybdenum disulfide (MoS_2), a three-atom-thick semiconductor, have been of particular interest both for the physics accessible in 2D crystals and the applications achievable with highly flexible materials. This dissertation presents a variety of experiments exploring the optoelectronic and mechanical properties of both monolayer MoS_2 and graphene. In particular, we present three studies: (1) the experimental realization of the valley Hall effect, an effect based on the Berry curvature of a material's energy bands, in monolayer MoS_2 ; (2) methods for directly measuring the bending stiffness of graphene (and related 2D materials); and (3) an investigation of the wrapping of microspherical droplets by monolayer MoS_2 . We conclude by discussing the future outlook of both “valleytronics” and microencapsulation by 2D materials.

BIOGRAPHICAL SKETCH

Kathryn Lorraine McGill fell in love with physics with the help of her extraordinary high school A.P. Physics teacher, Mr. Miles. She was fortunate to pursue her bachelor's degree in physics at the College of Creative Studies, otherwise known as "The Graduate School for Undergraduates", at the University of California, Santa Barbara. She completed both her master's degree and Ph.D. in physics at Cornell University, working for Paul L. McEuen and investigating "anything, as long as it's small." While in graduate school, she also discovered and fed an avid interest in physics outreach and communication by producing and hosting her own YouTube channel, *The Physics Factor*. She is looking forward to joining the faculty at the University of Florida as a physics lecturer, where she plans to make great use of the Department of Physics' media lab, the Lightboard.

To my family.

ACKNOWLEDGMENTS

The McEuen Group has been a wonderful home from which to pursue my Ph.D. in physics. Many thanks to McEuen members, past and present, with especial thanks to Peter Rose and Michael Reynolds: you have no idea how big a part you played in helping me earn my degree. Thank you for being both excellent scientists and excellent people. Thank you Melina Blees and Pinshane Huang, fearless physics women and compassionate mentor-friends. Thank you, Sam Roberts, for our many chats about both physics and life, and how to best put the two together. Thank you, Sam Norris: you became an important part of my support network from day one of our meeting. And of course, thank you Paul – for truly being an advisor, not just “that person I work for.” You have such an inciteful mind, cutting through the distracting and the extraneous in the practice of physics research, scientific talks, and life in general. Thank you for all of your guidance and support; as I start advising students, I hope to bring them the same clarity of thought that you have always provided to me.

Thank you to my committee members, Daniel C. Ralph and Tomás A. Arias, for your insight into my research from your tangential points of view. Additionally, I am grateful to both the IGERT and NSF graduate fellowships for funding most of my time at Cornell. I also could not have finished my Ph.D. without the health leave granted by the Cornell University Graduate School, a remarkable program for which I will ever be thankful.

Thank you to the staff of Rideau Analytics, who welcomed me into their office when I kicked off my dissertation writing. I have never had a more productive writing experience than during my week at Rideau; thank you so much!

Thank you to all of the friends I've made here at Cornell. Your friendship has been both inspiring and supportive; I couldn't ask for a better group of people to trek through grad school with. (And what a trek it was!) In particular, many thanks and much love to Veronica Pillar. You have been an integral part of my grad life, from the highs of first-year shenanigans to the lows necessitating my health leave. So many thank-yous for your friendship – all of them, in fact.

Shout-out to Ellie Newton-Sowerine, fellow CCS physics girl and friend from day one of college orientation. What would our freshmen selves think of us now, two lady physicists staying in the physics pipeline? I think they'd be pretty pleased with how we've turned out – though perhaps a *little* disappointed that we didn't become astronauts.

To all of the Cloyds, a huge thank you. John & Susan, thank you for our many discussions about life and its struggles – grad school very much included. I have learned so much from you about managing life in all of its ups and downs. Allie, thank you for always being my cheerleader, no matter what problem – in physics, or in life – might be plaguing me at the time.

Thank you Carolyn, Tom, and Ellie Adams, for welcoming me into your home when I needed it most. Your love and generosity continue to overwhelm me.

Finally, I thank my family, to whom this dissertation is dedicated. It is impossible to state the extent of my thankfulness for your love and support.

TABLE OF CONTENTS

BIOGRAPHICAL SKETCH.....	iii
DEDICATION.....	iv
ACKNOWLEDGEMENTS.....	v
LIST OF FIGURES.....	x
PREFACE.....	xi
CHAPTER 1: THE WORLD OF TWO-DIMENSIONAL MATERIALS	
1.1 Introduction	12
1.2 Outline of this dissertation.....	13
References.....	13
CHAPTER 2: ORIGINS OF THE VALLEY HALL EFFECT	
2.1 Introduction	15
2.2 The valley index	15
2.3 The anomalous Hall effect	16
2.4 The Berry curvature in crystalline solids.....	19
2.5 The intrinsic contribution to the anomalous Hall effect	21
2.6 Extrinsic contributions to the anomalous Hall effect.....	23
2.7 Distinguishing contributions to the anomalous Hall effect	23
2.8 On the suitability of MoS ₂ to demonstrate the valley Hall effect.....	24
References.....	27

CHAPTER 3: THE VALLEY HALL EFFECT IN MOLYBDENUM DISULFIDE TRANSISTORS

3.1	Introduction	29
3.2	Experimental approach to measuring the valley Hall effect	29
3.3	MoS ₂ device fabrication	31
3.4	Characterization of MoS ₂ transistors.....	34
3.5	Experiment setup.....	38
3.6	The valley Hall voltage response of MoS ₂ transistors.....	41
3.7	Scanning Hall voltage microscopy.....	43
3.8	Control Experiments.....	45
3.9	Measurement of the Valley Hall Conductivity.....	50
3.10	Conclusions and research outlook.....	53
	References.....	55

CHAPTER 4: MEASURING THE BENDING STIFFNESS OF GRAPHENE

4.1	Introduction	58
4.2	Experimental approach to measuring the bending stiffness	59
4.3	Fabrication and characterization of graphene devices	61
4.4	Radiation pressure measurement method	66
4.5	Thermal motion measurement method	68
4.6	Comparison with gravitational measurement method.....	71
4.7	Comparison with theoretical predictions.....	71
4.8	Applications and future directions	75
	References.....	76

CHAPTER 5: ENCAPSULATION OF MICRODROPLETS WITH TWO- DIMENSIONAL MATERIALS

5.1	Introduction	80
5.2	MoS ₂ sheet fabrication	82
5.3	Experiment setup.....	87

5.4	Wrapping microdroplets with monolayer MoS ₂	90
5.5	Conclusions and research outlook.....	96
	References.....	99
CHAPTER 6: OUTLOOK FOR TWO-DIMENSIONAL MATERIALS RESEARCH		
	102
	References.....	103
APPENDICES		
A	Derivation of the Berry Curvature	104
	References.....	107
B	Derivation of the intrinsic anomalous Hall effect in crystalline solids	108
	References.....	110
C	Derivation of the valley Hall conductivity in monolayer molybdenum disulfide.....	111
	References.....	116
	BIBLIOGRAPHY.....	118

LIST OF FIGURES

Figure 2.1: Band structure of MoS ₂	17
Figure 2.2: Contributions to the AHE.....	20
Figure 2.3: Crystal structure of MoS ₂	25
Figure 3.1: Optical selection rules in monolayer MoS ₂	30
Figure 3.2: Monolayer MoS ₂ device design	32
Figure 3.3: Typical conductivity of monolayer MoS ₂ devices	35
Figure 3.4: Typical photoconductivity of monolayer MoS ₂ devices.....	37
Figure 3.5: Schematic of the VHE experiment setup	40
Figure 3.6: The VHE in monolayer MoS ₂	42
Figure 3.7: Scanning voltage microscopy of the VHE in monolayer MoS ₂ ..	44
Figure 3.8: Characterization of bilayer MoS ₂ devices.....	46
Figure 3.9: Response of monolayer vs. bilayer MoS ₂ devices	48
Figure 3.10: On- vs. off-resonance excitation in monolayer MoS ₂ devices...	49
Figure 3.11: Photodoping dependence of monolayer MoS ₂ devices.....	51
Figure 3.12: Comparison of experimental and theoretical Hall conductivity	54
Figure 4.1: Release of graphene cantilevers from substrate	60
Figure 4.2: Graphene characterization	63
Figure 4.3: AFM of graphene samples.....	65
Figure 4.4: Measuring the bending stiffness of graphene.....	67
Figure 4.5: Thermal motion bending stiffness measurement.....	70
Figure 4.6: Comparison of bending stiffness measurement methods.....	72
Figure 5.1: Macroscopic wrapping of liquid drop by highly-bendable sheet	83
Figure 5.2: Image of initial wrapping sheet shapes.....	85
Figure 5.3: Cuvette for side and bottom co-viewing of wrapping events	86
Figure 5.4: Setup for manipulating wrapped microdroplets.....	88
Figure 5.5: Time lapse of a wrapping event	91
Figure 5.6: A variety of microdroplet wrappings.....	93
Figure 5.7: Hausdorff distance as a function of radius ratio	95
Figure 5.8: Folding via wrapping	98

“At some point, everything's going to go south on you...everything's going to go south and you're going to say, this is it. This is how I end. Now you can either accept that, or you can get to work. That's all it is. You just begin. You do the math. You solve one problem...and you solve the next one...and then the next. And If you solve enough problems, you get to come home.”

- *The Martian* (2015)

CHAPTER 1

THE WORLD OF TWO-DIMENSIONAL MATERIALS

1.1 Introduction

This dissertation covers a wide range of the physics of two-dimensional (2D) materials, a young field kickstarted in 2005 by the isolation of atomically thin materials, such as the one-atom-thick graphene and the three-atom-thick molybdenum disulfide (MoS_2)¹. Since this time, scientists have conducted experiments ranging from the optoelectronics^{2,3} to the mechanics⁴ of these materials.

In this dissertation we examine both graphene and MoS_2 across several areas of interest: (1) “valleytronics”, a sub-field exploring the properties and controllability of the so-called “valley” designation of the band electrons in a crystal (in analogy and addition to the charge and spin of the electrons); (2) direct measurement of the bending stiffness of 2D materials; and (3) wrapping at the microscale. Due to the breadth of this dissertation, detailed introductions to these subjects are left to the individual chapters exploring them.

1.2 Outline of this dissertation

This dissertation presents experiments conducted on both monolayer MoS₂ and graphene, covering “curvature” of all sorts: from the Berry curvature to the wrapping of microspheres.

To begin, in Ch. 2 we discuss in-depth the origins of the valley Hall effect (VHE) as a specific case of the more general anomalous Hall effect (AHE) arising from the Berry curvature found in certain crystalline energy bands. From here, in Ch. 3, we present our measurement⁵ of the VHE as a photoinduced AHE in monolayer MoS₂.

In Ch. 4 we switch gears into the world of mechanics to consider the measurement of bending stiffness in 2D materials by specifically measuring the bending stiffness of graphene⁶. In Ch. 5 we extend our exploration of bending by considering the case of a microdroplet wrapped by a 2D material, namely, in our experiment, monolayer MoS₂.

Finally, in Ch. 6, we close with some remarks on the outlook for research in 2D materials.

References

1. Novoselov, K. S. *et al.* Two-dimensional atomic crystals. *Proc. Natl. Acad. Sci. U. S. A.* **102**, 10451–10453 (2005).

2. Bonaccorso, F., Sun, Z., Hasan, T. & Ferrari, A. C. Graphene photonics and optoelectronics. *Nat. Photonics* **4**, 611–622 (2010).
3. Wang, Q. H., Kalantar-Zadeh, K., Kis, A., Coleman, J. N. & Strano, M. S. Electronics and optoelectronics of two-dimensional transition metal dichalcogenides. *Nat. Nanotechnol.* **7**, 699–712 (2012).
4. Lee, C., Wei, X., Kysar, J. W. & Hone, J. Measurement of the Elastic Properties and Intrinsic Strength of Monolayer Graphene. *Science* **321**, 385–388 (2008).
5. Mak, K. F., McGill, K. L., Park, J. & McEuen, P. L. The valley Hall effect in MoS₂ transistors. *Science* **344**, 1489–1492 (2014).
6. Bles, M. K. *et al.* Graphene kirigami. *Nature* **524**, 204–207 (2015).
7. McHale, G., Newton, M. I., Shirtcliffe, N. J. & Galdi, N. R. Capillary origami: superhydrophobic ribbon surfaces and liquid marbles. *Beilstein J. Nanotechnol.* **2**, 145–151 (2011).
8. Bae, J., Ouchi, T. & Hayward, R. C. Measuring the Elastic Modulus of Thin Polymer Sheets by Elastocapillary Bending. *ACS Appl. Mater. Interfaces* **7**, 14734–14742 (2015).
9. Paulsen, J. D. *et al.* Optimal wrapping of liquid droplets with ultrathin sheets. *Nat. Mater.* **14**, 1206–1209 (2015).
10. Huang, J. *et al.* Capillary wrinkling of floating thin polymer films. *Science* **317**, 650–653 (2007).

CHAPTER 2

ORIGINS OF THE VALLEY HALL EFFECT

2.1 Introduction

In this chapter we will review the physical origins of the valley Hall effect (VHE), which can arise due to both intrinsic and extrinsic mechanisms in a crystal. The *intrinsic* contribution to the VHE in a material is the result of broken inversion symmetry in its crystal structure; the *extrinsic* contributions result from the presence of defects. We will explore both types of contribution, and we'll close with a brief overview of why monolayer molybdenum disulfide (MoS_2) is our material of choice for the VHE experiment.

2.2 The valley index

In examining the origins of the VHE, we must first understand what is known as the “valley index” of an electron (or hole, as the case may be). To begin, we zoom out and consider our modern technological society. We are overwhelmingly familiar with the charge degree of freedom (DOF): it is the foundation on which our myriad electronic devices are based. The spin DOF is likewise reasonably well-known as it is at the heart of magnetic

devices, such as memory drives. The “valley” index is yet a third possible DOF for charge carriers in certain materials (specifically, as we will see, in crystals with broken inversion symmetry). The name “valley” refers to the shape of the bands at the material’s conduction band structure minima.

Figure 2.1 shows an example of these valleys in the band structure of MoS₂ calculated from density functional theory (DFT)¹. These systems are predicted to exhibit a measurable voltage in the charge DOF whose sign depends on the valley index of the accumulated Hall carriers².

2.3 The anomalous Hall effect

The VHE is a specific case of the phenomenon known as the anomalous Hall effect (AHE). In 1879, Edwin Hall observed that a transverse current develops when a current-carrying (non-ferromagnetic) conductor is placed in a perpendicular magnetic field³. This “Hall effect” is straightforwardly explained by the action of the Lorentz force on the electrons in the conductor, and it has an associated Hall conductivity σ_H . However, upon performing the same experiment with ferromagnetic conductors, Hall reported that the transverse current was an order of magnitude larger^{4,5}. The origins of this extra, “anomalous” current puzzled scientists for the better part of the last century⁶. The anomalous current can

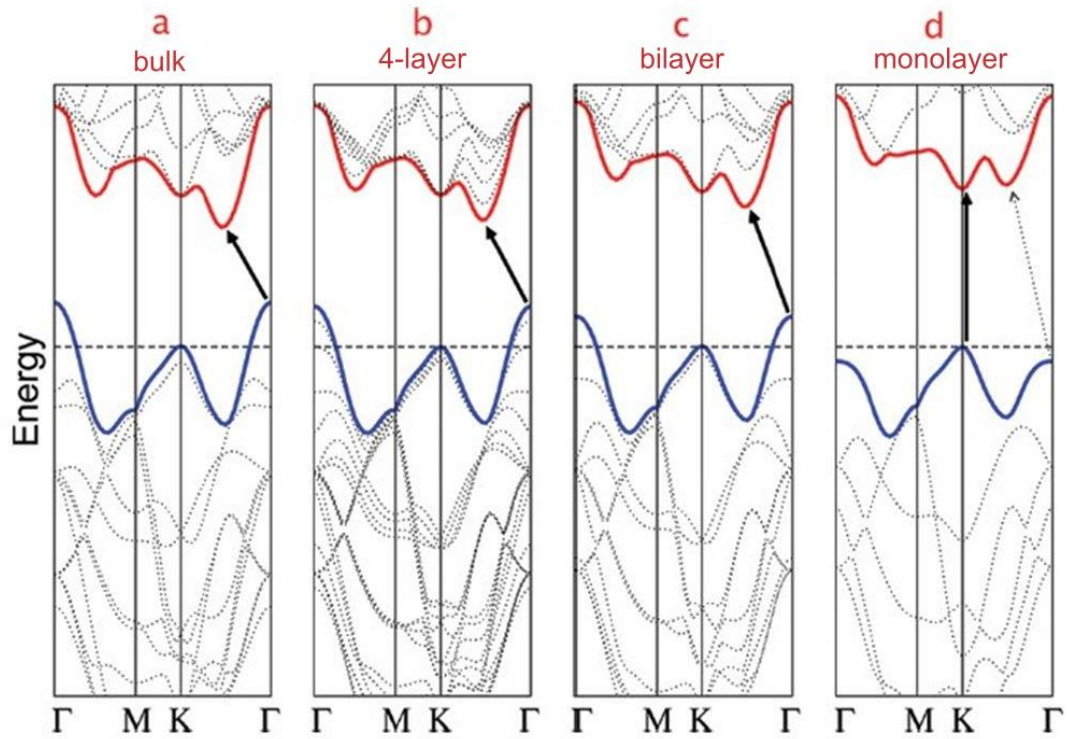


Figure 2.1: Band structure of MoS₂

DFT calculations for the band structure of (a) bulk, (b) four-layer, (c) bilayer, and (d) monolayer MoS₂. The solid arrows indicate the lowest energy transitions between the valence and conduction bands. The lowest-energy transition in bulk MoS₂ (a) is an indirect transition at the Γ point, whereas the lowest-energy transition in monolayer MoS₂ (d) is a direct transition of ~ 1.9 eV at the K point. The shape of the conduction band at this point looks like a valley, leading to the name “valley index”. Figure after Splendiani *et al.* (2010)¹.

be framed as having its own associated conductivity σ_H^a . As we will see, it is generally viewed as being composed of three components: an intrinsic term and two extrinsic terms.

A succinct understanding of the intrinsic (i.e. based on a perfect crystal) contribution to the AHE was finally achieved after Sir Michael Berry published a paper in 1984 on a quantum phase factor now known as the Berry phase⁷, a detailed derivation of which is provided in App. A. The Berry phase γ_n is written as the path integral in $\boldsymbol{\lambda}$ space

$$\gamma_n = \int_C d\boldsymbol{\lambda} \cdot \mathbf{A}_n(\boldsymbol{\lambda}) \quad (2.1)$$

where

$$\mathbf{A}_n(\boldsymbol{\lambda}) = i\langle n(\boldsymbol{\lambda}) | \nabla_{\boldsymbol{\lambda}} | n(\boldsymbol{\lambda}) \rangle \quad (2.2)$$

is called the Berry connection, $\boldsymbol{\lambda}$ is the parameter space through which the system adiabatically moves in time, and the $|n(\boldsymbol{\lambda})\rangle$ are the eigenkets of the system. The Berry connection functions as a vector potential, allowing us to write the magnetic-like Berry curvature $\boldsymbol{\Omega}_n$ as

$$\boldsymbol{\Omega}_n(\boldsymbol{\lambda}) = \nabla_{\boldsymbol{\lambda}} \times \mathbf{A}_n(\boldsymbol{\lambda}) \quad (2.3)$$

In general the Berry curvature is considered the fundamental quantity⁸, and it is viewed as the source of the intrinsic contribution to the AHE, so-named because it is inherently present in a pristine crystal.

However, defects in a crystal can also alter the velocities of the electrons in the same manner as does the Berry curvature; such contributions are dubbed the extrinsic contributions to the AHE⁶. In general these contributions can be split into two categories: the skew contribution and the side-jump contribution, both of which are detailed in Sec. 2.6. Thus, the entire anomalous Hall conductivity σ_H^a can be written as

$$\sigma_H^a = \sigma_H^{in} + \sigma_H^{sk} + \sigma_H^{sj} \quad (2.4)$$

where σ_H^{in} is the intrinsic contribution, σ_H^{sk} the extrinsic skew contribution, and σ_H^{sj} the extrinsic side-jump contribution (see visualizations in Fig. 2.2).

2.4 The Berry curvature in crystalline solids

The Berry curvature appears readily in crystalline solids. In these systems the parameter space is reciprocal space, or \mathbf{k} -space, and the basis kets are the periodic parts of the Bloch wavefunctions, $|u_n(\mathbf{k})\rangle$. Using Eqs. 2.2 and 2.3, the Berry curvature is thus

$$\boldsymbol{\Omega}_n(\mathbf{k}) = \nabla_{\mathbf{k}} \times i\langle u_n(\mathbf{k}) | \nabla_{\mathbf{k}} | u_n(\mathbf{k}) \rangle \quad (2.5)$$

From Eq. 2.5 it is clear that the Berry curvature is an intrinsic property of the band structure of crystalline solids. In particular, crystals with broken time-reversal or inversion symmetry have nonzero Berry curvatures (see Sec. 2.6 below).

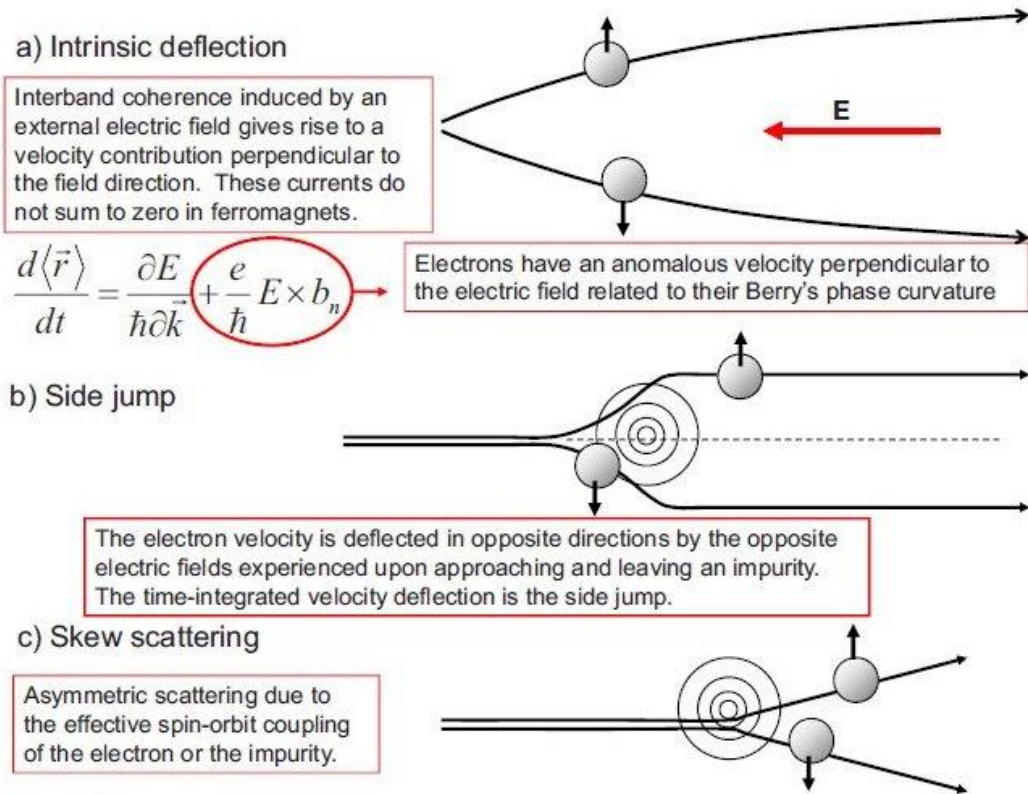


Figure 2.2: Contributions to the AHE

Cartoons demonstrating the (a) intrinsic, (b) side-jump, and (c) skew-scattering contributions to the AHE. Figure from Nagaosa, Sinova, Onoda, MacDonald, and Ong (2010)⁶.

2.5 The intrinsic contribution to the anomalous Hall effect

Several methods have been developed to explore the intrinsic contribution to the AHE (see Nagaosa, Sinova, Onoda, MacDonald, and Ong (2010)⁶ for a complete overview); the semiclassical derivation based on wave packet dynamics is presented in App. B. Briefly, we subject our Bloch electrons to a Hamiltonian that includes the perturbative electric potential $\varphi(\mathbf{r})$:

$$\hat{H} = \frac{\hat{\mathbf{p}}^2}{2m} + V(\mathbf{r}) - e\varphi(\mathbf{r}) \quad (2.6)$$

The velocity of our Bloch electrons is then

$$\mathbf{v}_n(\mathbf{k}) = \frac{\partial \varepsilon_n(\mathbf{k})}{\hbar \partial \mathbf{k}} - \frac{e}{\hbar} \mathbf{E} \times \boldsymbol{\Omega}_n(\mathbf{k}) \quad (2.7)$$

The second term in Eq. 2.6, dependent on the Berry curvature $\boldsymbol{\Omega}_n(\mathbf{k})$ (defined in Eq. 2.5), is always transverse to the applied electric field \mathbf{E} and will give rise to a Hall current in materials for which $\boldsymbol{\Omega}_n(\mathbf{k})$ is non-zero. $\boldsymbol{\Omega}_n(\mathbf{k})$ can thus be viewed as a magnetic-like driver of electron motion, resulting from the hopping of the electrons about the host atoms (see, for example, Fig. 3.1). This term does not appear in the foundational solid state physics textbooks by Ashcroft and Mermin (1976)⁹ or Kittel (2005)¹⁰, emphasizing the truly unexpected – or “anomalous” – nature of this term.

For materials in which we can ignore spin-orbit coupling (as we do in

our monolayer MoS₂ experiment in Ch. 3), we can learn about the general form of $\mathbf{\Omega}_n(\mathbf{k})$ by performing a symmetry analysis¹¹ of Eq. 2.7. First, let us consider the requirements of time reversal symmetry. Under time reversal \mathbf{E} is invariant, and \mathbf{v}_n and \mathbf{k} change sign. Time-reversal symmetry thus requires that

$$\mathbf{\Omega}_n(-\mathbf{k}) = -\mathbf{\Omega}_n(\mathbf{k}) \quad (2.8)$$

However, under spatial inversion \mathbf{v}_n , \mathbf{k} , and \mathbf{E} all change sign, so spatial inversion symmetry requires that

$$\mathbf{\Omega}_n(-\mathbf{k}) = \mathbf{\Omega}_n(\mathbf{k}) \quad (2.9)$$

It is clear that Eqs. 2.8 and 2.9 cannot both be true within a single system. Thus, for crystals with simultaneous spatial and time inversion symmetry, the Berry curvature vanishes and there is no anomalous Hall current. The AHE will *only* make an appearance in crystals with *either* broken time reversal *or* broken spatial inversion symmetry. Broken time-reversal symmetry, which occurs spontaneously in ferromagnets, results in the typical (charge) AHE¹¹, while broken spatial inversion symmetry allows for a “valley” AHE, based on the valley DOF of charge carriers (arising in materials such as monolayer MoS₂)¹².

2.6 Extrinsic contributions to the anomalous Hall effect

In addition to the intrinsic origins of the AHE discussed above, it is important to consider two extrinsic mechanisms that can also give rise to anomalous Hall currents (see Fig. 2.2). These are known as the skew-scattering and side-jump contributions to the AHE. (Note that the side-jump term actually encompasses several related mechanisms⁶, but for the purposes of this dissertation, we will only discuss the original side-jump mechanism, illustrated in Fig. 2.2(b).)

The side-jump mechanism proposed by Berger (1970)¹³ and depicted in Fig. 2.2(b) arises from the interaction of the incident electron with the local electric fields of an impurity in the material. The side-jump conductivity (σ_H^{sj}) is independent of τ , the Bloch electron transport lifetime. In contrast the skew-scattering mechanism proposed by Smit (1958)¹⁴ arises from the effective spin-orbit coupling between the incident electron and an impurity, as illustrated in Fig. 2.2(c) Smit (1958) showed that for skew scattering, $\sigma_H^{sk} \propto \tau \propto \sigma_{xx}$, where σ_{xx} is the longitudinal conductivity.

2.7 Distinguishing contributions to the anomalous Hall effect

Given that both σ_H^{in} and σ_H^{sj} are independent of τ (and by extension, of σ_{xx}), experimentally distinguishing the relative magnitudes of the AHE

components defined in Eq. 2.4 remains challenging⁶. Although σ_H^{sk} is expected to dominate for clean samples at low temperatures, in which the relaxation times can be extremely large, dirty samples at high temperatures have very short τ and should be dominated by some mixture of σ_H^{in} and σ_H^{sj} . Empirically, we can thus only separate σ_H into contributions that vary linearly with σ_{xx} (i.e. σ_H^{sk}) and contributions that are independent of σ_{xx} (i.e. σ_H^{in} and σ_H^{sj}). Generally, σ_H^{sk} is only important in high-mobility materials. According to Nagaosa, *et al.* (2010)⁶, and based on the work of Sinitsyn, *et al.*, (2007)¹⁵, $\sigma_H^{sj} = -2\sigma_H^{in}$ in band structures where the Berry curvature is constant (which, as we will see in Sec. 2.8, is the case in our experiment).

2.8 On the suitability of MoS₂ to demonstrate the valley Hall effect

The AHE experiments presented in this dissertation make use of monolayer MoS₂ as the material of interest for demonstrating the particular case of the VHE. The two-dimensional (2D) crystal monolayer MoS₂ is a suitable choice of material for this demonstration for a number of reasons^{12,16}:

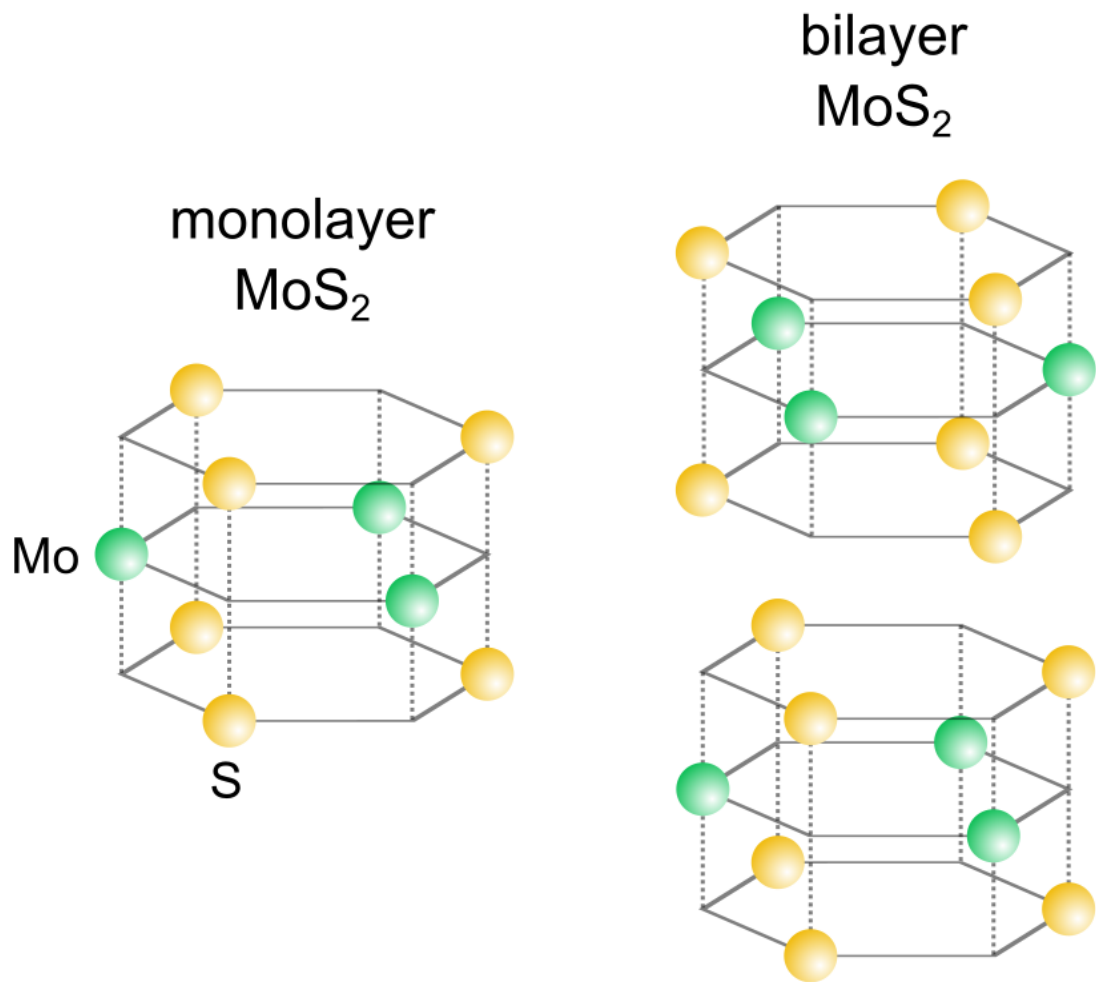


Figure 2.3: Crystal structure of MoS₂

The crystal structures of (left) monolayer and (right) bilayer MoS₂, shown a side view. The side view makes the inversion symmetry of bilayer MoS₂ clear, in contrast to the *broken* inversion symmetry of monolayer MoS₂.

1. It is a crystal with broken inversion symmetry (and simultaneously *not* a material with broken time reversal symmetry), thus meeting the symmetry requirements of the VHE (see Fig. 2.3(a)).
2. Its bilayer form *is* symmetric under inversion, providing a straightforward control experiment (see Fig. 2.3(b)).
3. It is a direct band gap semiconductor with a band gap of 1.9 eV at the K and K' valleys in the Brillouin zone, allowing for the use of optically-driven transitions of the valley carriers (see Fig. 2.1).
4. It has a relatively low mobility, thus excluding σ_H^{sk} from consideration in the generated effect.
5. We expect to measure a change in conductivity due to the photoexcited valley Hall effect, with magnitude equal to

$$\delta\sigma_H^v = -\frac{e^2}{h} \frac{2\pi\hbar^2}{m_b E_g} \delta n_c \quad (2.10)$$

where m_b is the electron band mass, E_g is the band gap, and δn_c is the carrier imbalance between the K and K' valleys. A full derivation of Eq. 2.10 is presented in App. C.

With this we conclude our exploration of the origins of the VHE, and, with these last several points in mind, we turn our attention in Ch. 3 to the experimental realization of the VHE in monolayer MoS₂.

References

1. Splendiani, A. *et al.* Emerging Photoluminescence in Monolayer MoS₂. *Nano Letters* **10**, 1271–1275 (2010).
2. Xiao, D., Liu, G.-B., Feng, W., Xu, X. & Yao, W. Coupled Spin and Valley Physics in Monolayers of MoS₂ and Other Group-VI Dichalcogenides. *Physical Review Letters* **108**, 196802 (2012).
3. Hall, E. H. On a New Action of the Magnet on Electric Currents. *American Journal of Mathematics* **2**, 287 (1879).
4. Hall, E. H. XXXVIII On the new action of magnetism on a permanent electric current. *Philosophical Magazine Series 5* **10**, 301–328 (1880).
5. Hall, E. H. XVIII On the “Rotational Coefficient” in nickel and cobalt. *Philosophical Magazine Series 5* **12**, 157–172 (1881).
6. Nagaosa, N., Sinova, J., Onoda, S., MacDonald, A. H. & Ong, N. P. Anomalous Hall effect. *Reviews of Modern Physics* **82**, 1539–1592 (2010).
7. Berry, M. V. Quantal Phase Factors Accompanying Adiabatic Changes. *Proceedings of the Royal Society A: Mathematical, Physical and Engineering Sciences* **392**, 45–57 (1984).
8. Kuratsuji, H. & Iida, S. Effective Action for Adiabatic Process Dynamical Meaning of Berry and Simon’s Phase. *Progress of theoretical physics* **74**, 439–445 (1985).
9. Ashcroft, N. W. & Mermin, N. D. *Solid State Physics*. (Brooks/Cole, Cengage Learning, 1976).
10. Kittel, C. *Introduction to Solid State Physics*. (John Wiley & Sons, Inc., 2005).

11. Xiao, D., Chang, M.-C. & Niu, Q. Berry phase effects on electronic properties. *Reviews of Modern Physics* **82**, 1959–2007 (2010).
12. Xiao, D., Yao, W. & Niu, Q. Valley-Contrasting Physics in Graphene: Magnetic Moment and Topological Transport. *Physical Review Letters* **99**, 236809 (2007).
13. Berger, L. Side-jump mechanism for the Hall effect of ferromagnets. *Physical Review B* **2**, 4559 (1970).
14. Smit, J. The spontaneous Hall effect in ferromagnetics II. *Physica* **24**, 39–51 (1958).
15. Sinitsyn, N. A., MacDonald, A. H., Jungwirth, T., Dugaev, V. K. & Sinova, J. Anomalous Hall effect in a two-dimensional Dirac band: The link between the Kubo-Streda formula and the semiclassical Boltzmann equation approach. *Physical Review B* **75**, 045315 (2007).
16. Mak, K. F., Lee, C., Hone, J., Shan, J. & Heinz, T. F. Atomically Thin MoS₂: A New Direct-Gap Semiconductor. *Physical Review Letters* **105**, 136805 (2010).

CHAPTER 3

THE VALLEY HALL EFFECT IN MOLYBDENUM DISULFIDE TRANSISTORS

3.1 Introduction

In the previous chapter, we explored the origins of the valley Hall effect (VHE) as a particular manifestation of the anomalous Hall effect (AHE). Specifically, the VHE appears in crystals, such as monolayer molybdenum disulfide (MoS_2), with broken inversion symmetry. In this chapter we present an expansion of our work experimentally demonstrating the VHE: Mak, McGill, Park, and McEuen (2014)¹. We begin by overviewing anticipated observations, given the criteria presented in Sec. 2.8.

3.2 Experimental approach to measuring the valley Hall effect

As summarized in Sec. 2.8, monolayer MoS_2 is an excellent candidate for the detection of the VHE – or more precisely, the photoinduced AHE. It has broken inversion symmetry² (Fig. 2.3), and its optical pumping rules (Fig. 3.1) are such that electrons are excited in the K and K' valleys by right-handed and left-handed circularly polarized light at 1.9 eV, respectively^{3,4}. Thus, we expect to generate a population imbalance in photoexcited carriers between the K and K' valleys (depending on the handedness of the incident

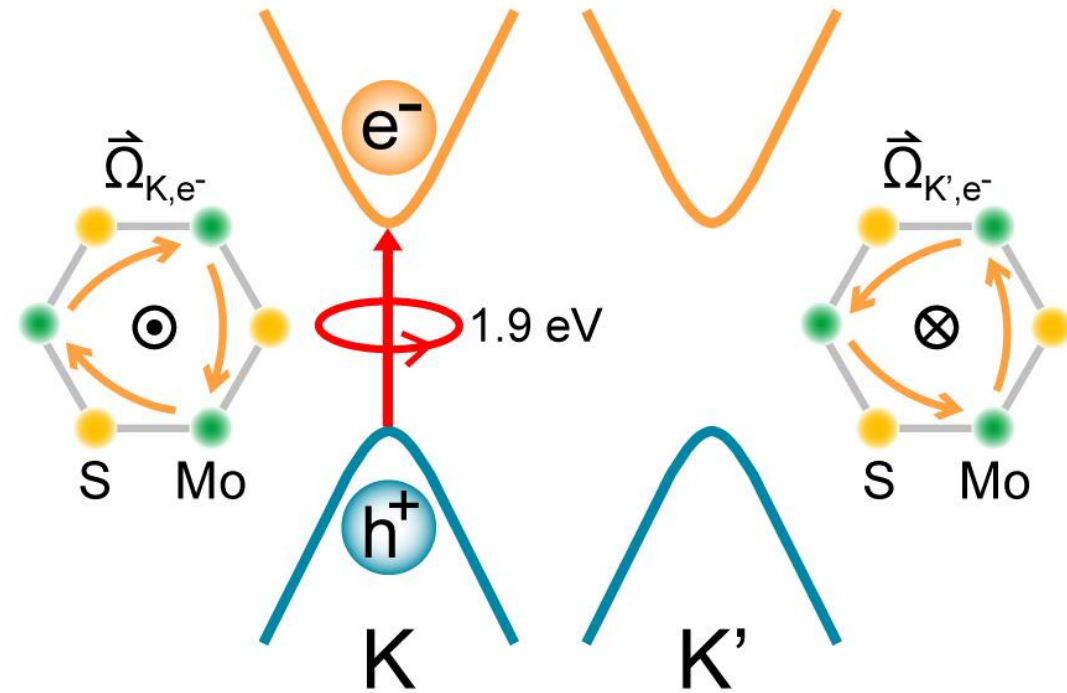


Figure 3.1: Optical selection rules in monolayer MoS₂

The valley-dependent optical selection rules are such that right-handed light at 1.9 eV excites electrons in the K valley and 1.9 left-handed light excites K' electrons in monolayer MoS₂. In the depiction of the MoS₂ lattice to the left and right of the K and K' valleys, respectively, the orange arrows represent the clockwise and counterclockwise hopping motion (respectively) of the electrons around the Mo atoms. Note that the electrons at the two valleys possess opposite Berry curvatures $\vec{\Omega}$. Figure from Mak, McGill, Park, and McEuen (2014)¹.

light) and to measure that imbalance as an AHE. Likewise, linearly polarized light should not generate such a population imbalance. Moreover, bilayer MoS₂ is inversion symmetric (as shown in Fig. 2.3), so we do not expect to observe a Hall separation of valley carriers in bilayer devices. It is important to note that the tools we are using to measure the VHE are all based on the charge degree of freedom (DOF) – that is, we are able to directly detect (charge) voltages but cannot directly measure “valley voltages”. Fortunately, by selectively photoexciting electrons in MoS₂ using its optical selection rules^{3,4}, we expect to measure a (charge) Hall voltage that can *only* be present as a result of the separation of charge carriers based on their *valley* index. Furthermore, as shown in Fig.3.2, we expect the Hall conductivity to be comprised of both the intrinsic and the side-jump contributions. We thus expect to measure a valley Hall conductivity proportional to the carrier imbalance between the K and K’ valleys, as introduced in Eq. 2.10.

3.3 MoS₂ device fabrication

To study the VHE, we designed MoS₂ transistors to have a 4-contact Hall bar geometry, as shown in Fig. 3.2. We have two reasons for designing our Hall bar devices with the long Hall probes and short photoconduction

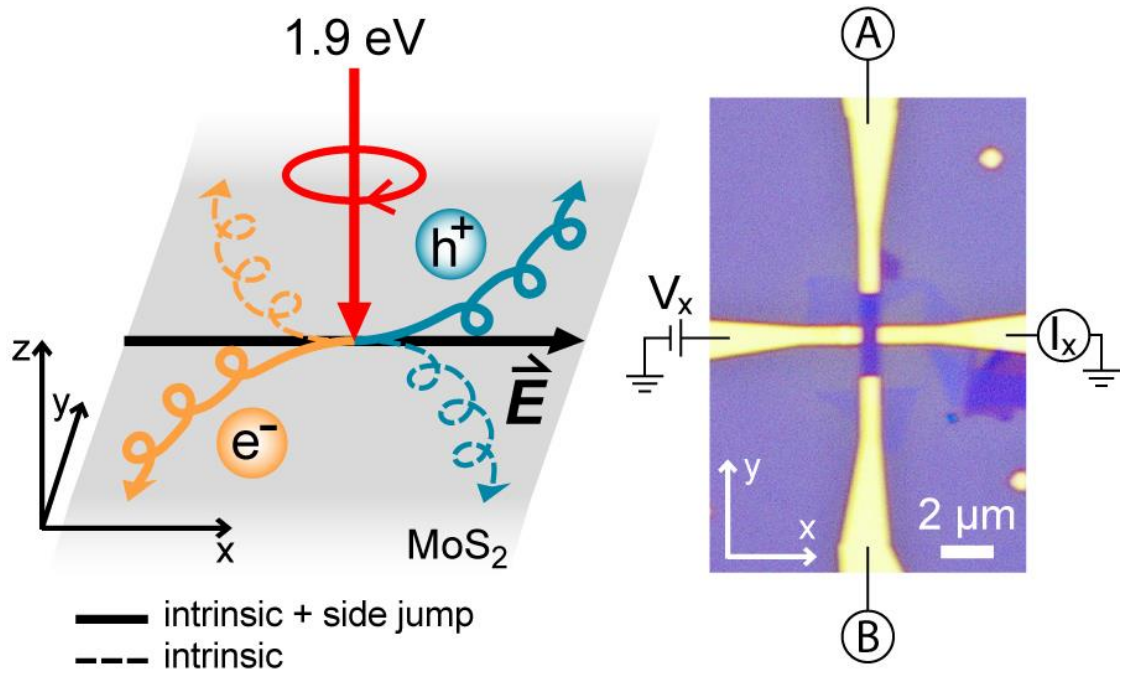


Figure 3.2: Monolayer MoS₂ device design

(left) Schematic of a photoinduced AHE driven by a net valley polarization. The dotted lines show the path of the electrons from the intrinsic effect alone; the solid lines show the result of the intrinsic and side-jump effects together, as explained in Sec. 2.7 (right) An image of a typical monolayer MoS₂ Hall bar device and the wiring scheme used for the measurement, more fully depicted in Fig. 3.5. In our catalog of devices, this is device M1. Figure from Mak *et al.* (2014)¹.

channels shown in the picture:

1. We want the photocurrent to be produced near the center of the device so that we can reasonably attribute any voltage detected by the Hall probe to the motion of the Hall carriers, rather than to photoexcited carriers from the photoconduction channel.
2. By focusing our laser on the center of the device and moving the Hall probes away from the device center, we reduce the background photovoltage generated at the metal-semiconductor probe contacts.

To begin fabrication, we mechanically exfoliated MoS₂ monolayers from bulk MoS₂ crystals (SPI Supplies) onto silicon (Si) substrates coated by 300 nm of silicon dioxide (SiO₂). Monolayer samples were identified using a combination of optical contrast and photoluminescence spectroscopy⁵. We used standard electron beam lithography techniques to define metal contact areas on our exfoliated samples. Electron beam evaporation was then used to deposit 0.5 nm titanium (Ti)/50 nm gold (Au) as contacts, followed by a standard methylene chloride/acetone lift-off procedure. Using electron beam lithography to create an etch mask, we defined the Hall bar geometry using a ten-second low-pressure sulfur hexafluoride (SF₆) plasma etch. Finally, the

device was laser annealed in high vacuum^{6,7} ($\sim 10^{-6}$ torr) at 120 °C for ~ 10 hr before measurement. We investigated multiple devices in this study: six monolayer MoS₂ devices, labeled as M1-M6, and two bilayer MoS₂ devices, labeled as B1 and B2.

3.4 Characterization of MoS₂ transistors

We begin our experiments by optoelectrically characterizing our devices. Device M1 is shown in the schematic presented in Fig. 3.2. The gate voltage (V_g)-dependence of its conductivity (σ_{xx}), extracted from both two- and four-point measurements, is shown in Fig. 3.3. We observe the usual n-type field effect transistor behavior⁸. To measure the two-point conductivity, we apply a bias of $V_x = 0.5$ V to the short channel of the device and monitor the source-drain current I_x . We measure the four-point conductivity by swapping the drain and B contacts on the device, as shown in Fig. 3.5 and taking into account a geometric factor⁹ of $\ln 2 / \pi$. The two- and four-point conductivities are similar in magnitude, indicating near-ohmic contacts in the device⁶. (Although the I_x - V_x curves show the presence of Schottky barriers at small bias (Fig. 3.3, inset), this has little influence on our measurements at high bias: we typically take measurements at $V_x=0.5$ V.) A four-point carrier mobility of $100 \text{ cm}^2 \text{ V}^{-1} \text{ s}^{-1}$ and a two-point carrier mobility of

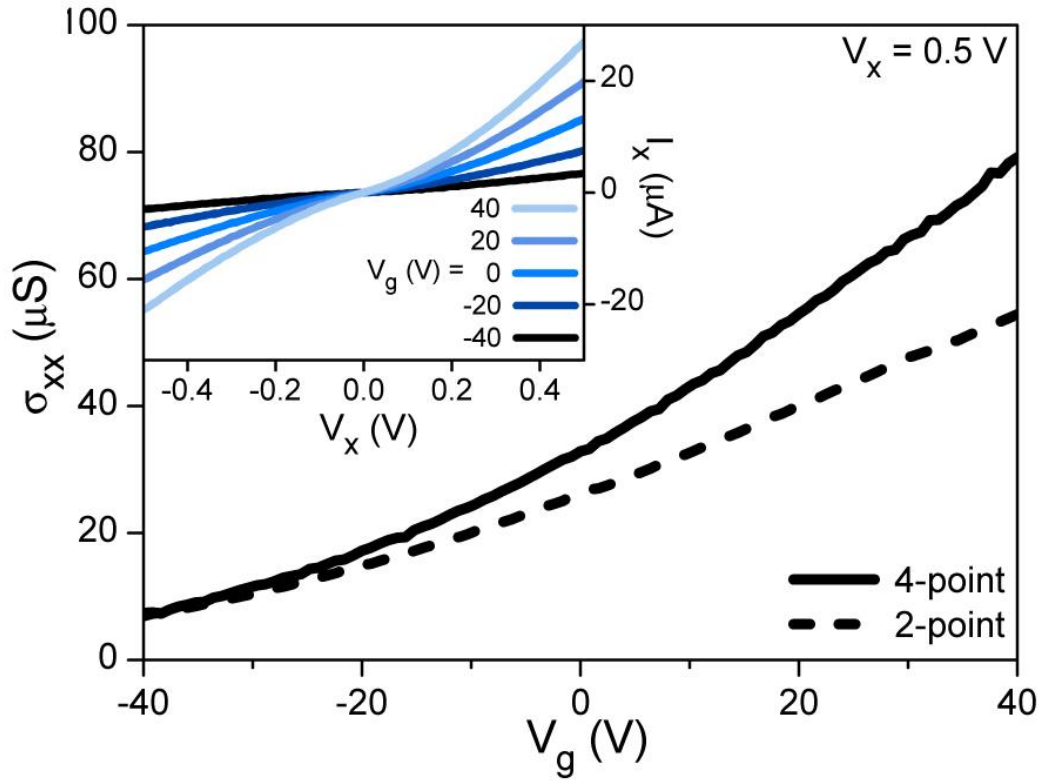


Figure 3.3: Typical conductivity of monolayer MoS₂ devices

(main) Two-point (dashed) and four-point (solid) conductivities as a function of gate voltage V_g at source-drain voltage $V_x = 0.5$ V for the device M1 pictured in Fig. 3.2.

(inset) Source-drain current I_x as a function of V_x at a variety of V_g values. Close to $V_x = 0$ V the I_x - V_x curves are nonlinear due to the presence of Schottky barriers; however, we conduct our experiments far from $V_x = 0$ V, in the linear regions of the I_x - V_x curves. (Typically, we take measurements at $V_x = 0.5$ V.) Figure from Mak *et al.* (2014)¹.

$60 \text{ cm}^2 \text{ V}^{-1} \text{ s}^{-1}$ are extracted at high V_g , where the σ_{xx} - V_g dependence becomes linear.

In Fig. 3.4, we examine the photoresponse of our device in order to confirm the appropriate photon energy (E) for efficient excitation of valley-polarized carriers^{3,10}. The change in conductivity with and without laser illumination $\Delta\sigma_{xx} = \sigma_{xx,light} - \sigma_{xx,dark}$ plotted as a function of E clearly shows the A (at $E \approx 1.9 \text{ eV}$) and B (at $E \approx 2.1 \text{ eV}$) resonances of monolayer MoS₂⁵. The A peak of $\sim 1.9 \text{ eV}$ is the (direct) band gap of monolayer MoS₂, and it is located at the K and K' valleys in the band structure (see both Figs. 2.1 and 3.1). Shown in the inset is the photocurrent ΔI_x as a function of V_x (at $V_g = 0 \text{ V}$) under various laser excitation intensities P . The inset data were taken with a laser centered at the A peak (1.9 eV) and focused at the center of the device. Similar to the effect of electrical gating (Fig. 3.3, inset), the effect of incident photons (Fig. 3.4, inset) is to increase the channel conductivity σ_{xx} , which indicates that photoconduction is the main mechanism driving the photoresponse in our device¹¹. Photocurrent generation under zero bias is negligible.

We note that with this geometry and fabrication recipe, the Hall probe typically picks up a background voltage of about 1 per 100 of V_x due to

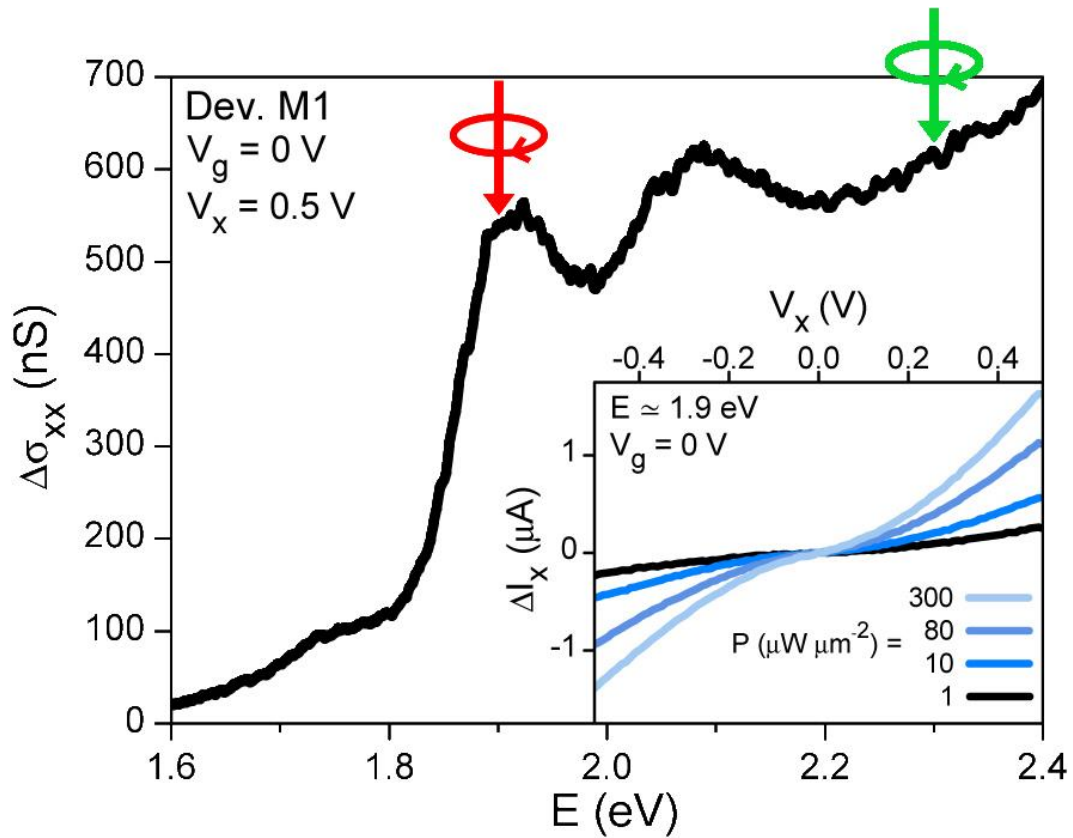


Figure 3.4: Typical photoconductivity of monolayer MoS₂ devices

(main) Energy E spectrum of the change in conductivity $\Delta\sigma_{xx}$ due to the photoexcitation of carriers. The peak indicated by the red arrow at 1.9 eV is the band gap of monolayer MoS₂; the green arrow indicates the off-resonance excitation of 2.3 eV used as a control for the photoexcitation of valley-specific carriers. (inset) Change in current ΔI_x as a function of bias voltage V_x for a variety of incident powers at 1.9 eV excitation. Similar to the inset of Fig. 3.3, the device is effectively gated by the incident light. Figure from Mak *et al.* (2014)¹.

remnant longitudinal-transverse coupling. This finite longitudinal-transverse coupling does not affect our AHE measurement, which is performed under modulations of the handedness of incident light (see Sec. 0).

3.5 Experiment setup

With our devices fabricated and characterized, we now describe our experimental setup, a schematic of which is shown in Fig. 3.5. All experiments were performed in a Janis cryostat cooled with liquid nitrogen, and, unless otherwise noted, all experiments were performed at 77 K.

To begin, we linearly polarize the light from a 1.9 eV diode laser, on resonance with the K and K' direct band gaps found in MoS₂. The light then passes through a photoelastic modulator (PEM), which is effectively a waveplate with adjustable phase delay $\Delta\lambda$, that can be synched to a lock-in amplifier for the detection of small voltage signals resulting from the photoexcited carriers. The angle θ between the initial linear polarizer and the PEM is set appropriately to produce circularly polarized light ($\theta = \pm 45^\circ$) in the quarter-wave ($\Delta\lambda = 1/4$) condition, while the half-wave ($\Delta\lambda = 1/2$) condition produces linearly polarized light. The PEM switches the circular polarization back and forth between right-handed ($\theta = 45^\circ$) and left-handed ($\theta = -45^\circ$) light at 50 kHz, and it switches the linear polarization back and

forth between θ and $\theta - 90^\circ$ at 100 kHz. We designate the case in which the circular polarization starts with $\theta = 45^\circ$ as “R-L” excitation, and the case in which it starts with $\theta = -45^\circ$ as “L-R” excitation. We denote linearly polarized light as “s-p” excitation.

As can be seen in Fig. 3.5, the laser reflects off of a scanning mirror and onto the device via a 40x microscope objective in an inverted microscope. The scanning mirror allows us to precisely position the laser on the center of the device; additionally, we can use it to produce raster-scan maps of the excitation information (for example, as shown Fig. 3.7). The spot diameter of the laser on the device is $\sim 1\text{-}3\ \mu\text{m}$, depending on the specific measurement, and the incident intensity is $\sim 100\text{-}150\ \mu\text{W}\ \mu\text{m}^{-2}$. We minimized effects from possible modulation of the beam position by control experiments using expanded illumination with a beam diameter of $\sim 5\ \mu\text{m}$. We were able to reduce undesirable power modulation to a level less than 10^{-4} at the sample, a level small enough to be negligible in our Hall voltage measurement.

In order to collect photo- and Hall conductivity spectra, we used a Fianium supercontinuum laser source immediately followed by a monochromator, selecting a line width of $\sim 5\ \text{nm}$ for each color. Device images were taken by collecting reflected (white) light on a silicon

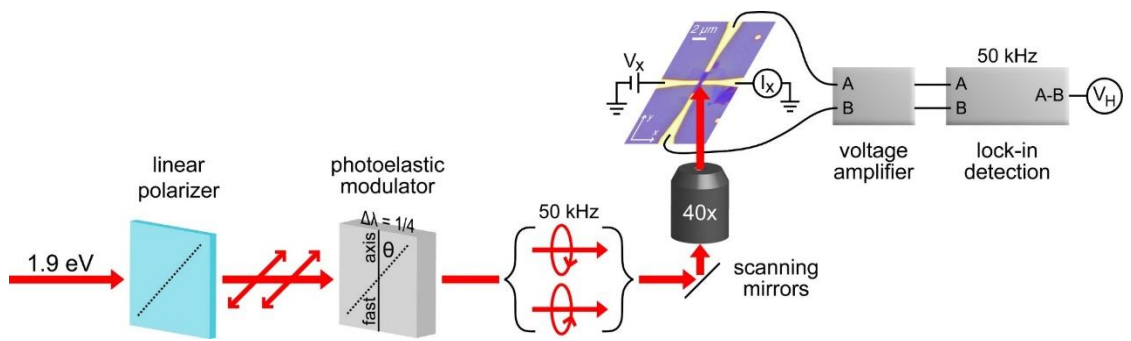


Figure 3.5: Schematic of the VHE experiment setup

We linearly polarize 1.9 eV light from a diode laser and pass it through a photoelastic modulator (PEM). The PEM allows us to alternatively generate right- and left-handed circularly polarized light at 50 kHz. We use a lock-in amplifier set to 50 kHz for detection of the Hall voltage signal.

photodiode. We collected electrical measurements by wiring our devices as shown in Fig. 3.5. We bias the device by a voltage V_x across the short channel, across which we also measure the current I_x . We measure the Hall voltage V_H across contacts A and B. This signal is pre-amplified before passing to the lock-in amplifier, which is synched to the frequency of the PEM. The final signal is recorded by a computer through a National Instruments data acquisition device (DAQ). The computer sets V_x and the gate voltage V_g and measures I_x .

3.6 The valley Hall voltage response of MoS₂ transistors

By parking the laser spot at the center of the device, we studied the Hall response under on-resonance excitation (centered at $E \approx 1.9$ eV). In Fig. 3.6(a), we show the V_x -dependence of the anomalous Hall voltage (V_H) at $V_g = 0$ V. We observe a small V_H that scales linearly with V_x under R-L modulation (Fig. 3.6(a), solid red line). This is the signature of a photoinduced AHE driven by a net valley polarization. Given the geometry of the electrical connections shown in Fig. 3.5, a positive Hall voltage under R-L modulation for a positive bias is observed. This is consistent with the prediction of a side-jump–dominated VHE (Eq. 2.10)^{2,12}. The sign of the signal is reversed when the excitation is changed to L-R modulation (Fig.

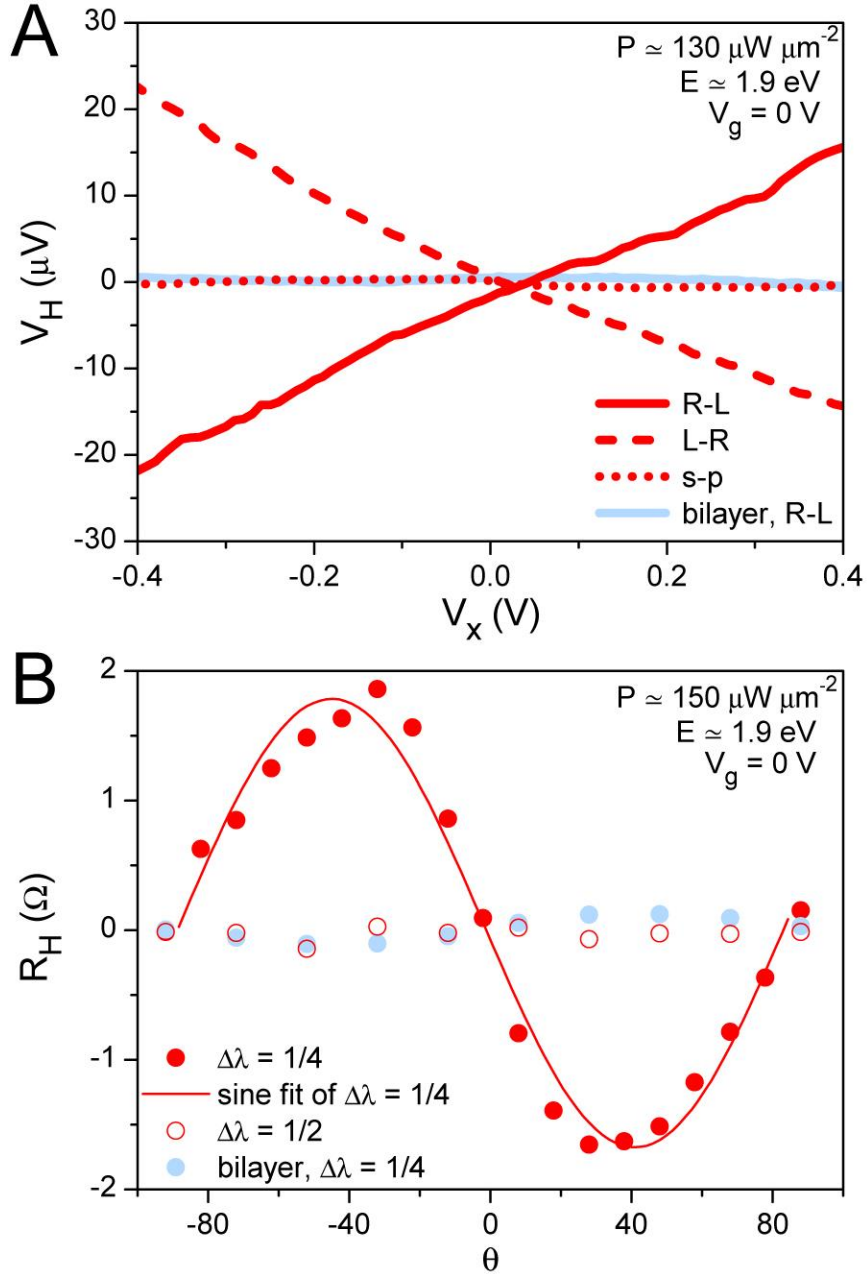


Figure 3.6: The VHE in monolayer MoS₂

(a) Valley Hall voltage V_H as a function of bias voltage V_x under 1.9 eV excitation at $130 \mu\text{W } \mu\text{m}^{-2}$. Red data from monolayer device M1; blue data from bilayer device B1. Solid/dashed line shows right-left handed (R-L)/left-right handed (L-R) modulation. Dotted line shows linear (s-p) modulation. Please refer to the text in Sec. 3.5 for a full explanation of modulation notation. (b) Hall resistance R_H as a function of incident angle θ for: (red filled dots) quarter-waveplate ($\Delta\lambda=1/4$), and (red open dots) half-waveplate ($\Delta\lambda=1/2$) modulation incident on monolayer device M1; (red line) sine fit of quarter-waveplate modulation data; (blue closed dots) quarter-waveplate modulation incident on bilayer device B1. Figure from Mak *et al.* (2014)¹.

3.6(a), dashed red line). In contrast, no net Hall voltage is seen when we switch to linear (s-p) modulation (Fig. 3.6(a), dotted red line). We observe identical patterns of behavior across all of our monolayer devices.

To study the polarization dependence carefully, the anomalous Hall resistance $R_H = V_H/I_x$ as a function of the angle θ is shown in Fig. 3.6(b) for both the quarter- and half-wave modulations. We see that the Hall resistance R_H exhibits a sinusoidal dependence on θ under quarter-wave modulation. A maximum Hall resistance of $\sim 2 \Omega$ is measured under an excitation intensity of $\sim 150 \text{ mW mm}^{-2}$. For comparison, zero Hall resistance is observed under half-wave modulation. Our results are consistent with recent experimental observations of a net valley polarization under the optical excitation of the A resonance with circularly polarized light^{3,4,13–15}.

3.7 Scanning Hall voltage microscopy

We spatially mapped the photocurrent and Hall voltage responses of our devices under illumination. All of the maps were recorded at $V_g = 0 \text{ V}$ and $V_x = 0.5 \text{ V}$, using a continuous-wave diode laser centered at 1.9 eV , with spot diameter $\sim 1 \mu\text{m}$, and incident power $\sim 50 \mu\text{W}$. Figure 3.7 shows scanning photocurrent images of several monolayer devices. The photocurrent is mainly generated at the center of the device when a source-

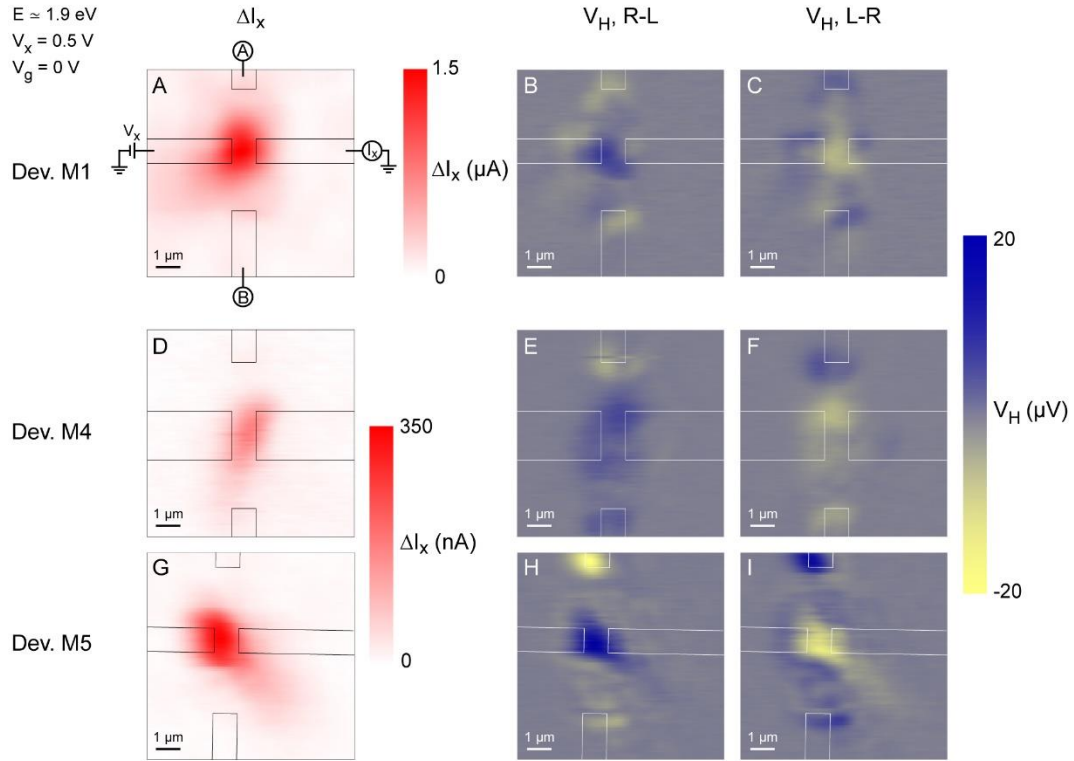


Figure 3.7: Scanning voltage microscopy of the VHE in monolayer MoS₂
 (left) Scanning photocurrent (ΔI_x) images for three monolayer devices, M1, M4, and M5. Contacts are outlined in black; measurement scheme depicted in upper left map. Photocurrent generation mainly occurs in the center of the device. (right) Scanning Hall voltage (V_H) images of the same devices under R-L and L-R modulation, as labeled. Contacts are outlined in thin white lines. Note that V_H changes sign from one modulation to the next. Please refer to Fig. 3.6 and Sec. 0 for a full explanation of modulation notation. All maps taken with $\sim 50 \mu\text{W}$ incident light at an energy $E=1.9 \text{ eV}$, bias voltage $V_x=0.5 \text{ V}$, and gate voltage $V_g=0 \text{ V}$. Figure from Mak *et al.* (2014)¹.

-drain bias voltage V_x is applied across the short channel. The corresponding scanning Hall voltage (V_H) images are shown to the right of the photocurrent maps for R-L and L-R modulations. We see that a finite Hall voltage is produced at the center of the monolayer devices, coinciding with the location of photocurrent production. Furthermore, in all devices, the sign of V_H reverses when the helicity of the modulation changes from R-L to L-R.

3.8 Control Experiments

As our first control experiment, we examine the Hall response of bilayer devices, beginning with their optoelectronic characterization. Figure 3.8(a) shows the 4-point conductivity as a function of back gate voltage for bilayer device B2. Similar to the monolayer devices, we only observe n-type behavior. This particular device has a 4-point mobility of $\sim 440 \text{ cm}^2 \text{ V}^{-1} \text{ s}^{-1}$. In general, bilayer devices have slightly higher electron mobilities (typically between 100 and 500 $\text{cm}^2 \text{ V}^{-1} \text{ s}^{-1}$) compared to their monolayer counterparts (typically between 50 and 300 $\text{cm}^2 \text{ V}^{-1} \text{ s}^{-1}$). Figure 3.8(b) shows the spectra of the change in photoconduction for monolayer device M2 (black) and bilayer device B2 (blue). The similar photoconduction spectra reflect their similar absorption spectra originating from direct optical transitions. This result is

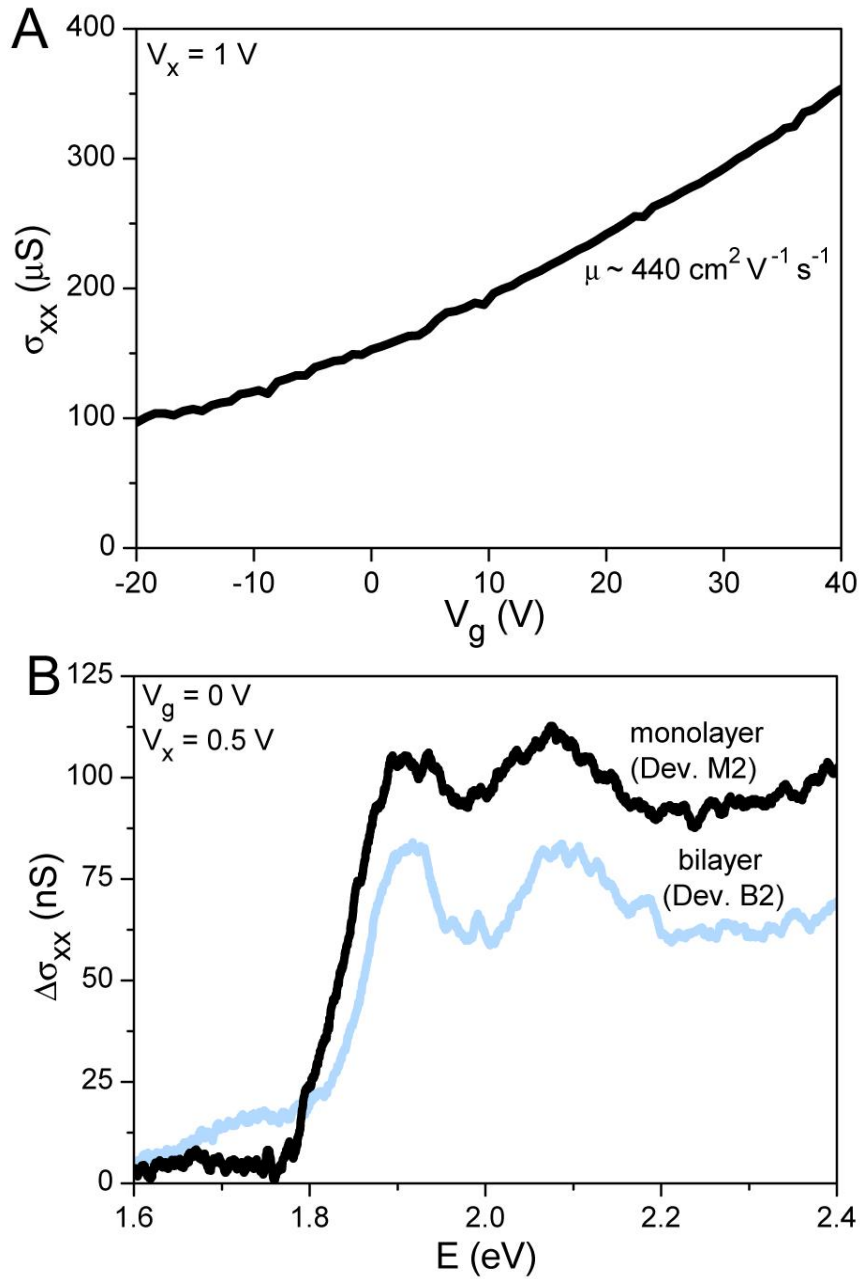


Figure 3.8: Characterization of bilayer MoS₂ devices

(a) Four-point conductivity σ_{xx} as a function of gate voltage V_g at a bias $V_x=1$ V. The mobility μ is about $440 \text{ cm}^2 \text{ V}^{-1} \text{ s}^{-1}$. (b) Change in conductivity $\Delta\sigma_{xx}$ due to photoexcitation as a function of incident light energy E for $V_g=0$ V and $V_x=0.5$ V. The spectrum from a monolayer device is shown in black; the spectrum from a bilayer device is in blue. Figure from Mak *et al.* (2014)¹.

consistent with recent optical studies of the absorption spectra of MoS₂ samples of varying thickness⁵.

In Fig. 3.9, we see that the bilayer device has a similar photocurrent map to those of the monolayer devices. However, the Hall voltage is much smaller – by about a factor of 10 – than that of the monolayer devices. We note that significant photovoltages (particularly in the bilayer device) are also observed at the metal-semiconductor contacts of the Hall probe (both at zero and finite bias along the short channel). These photovoltages probably arise from the modification of the polarization state by the metal contacts, leading to a corresponding power modulation. The absence of a Hall voltage response in the center of the bilayer device, in contrast to the significant response in the monolayer device, supports our expectation that the inversion-symmetric bilayer device *does not* exhibit a VHE while the broken inversion symmetry of the monolayer device *does* exhibit a VHE.

As a second straightforward control experiment, we compare the Hall voltage maps of monolayer devices excited both on-resonance at the A exciton (1.9 eV) with those of an off-resonance excitation of 2.3 eV in Fig. 3.10. While the device displays a similar photocurrent response under both the 1.9 eV and 2.3 eV excitation energies, we only observe a significant Hall voltage under R-L modulation when the device is excited at its band gap, 1.9

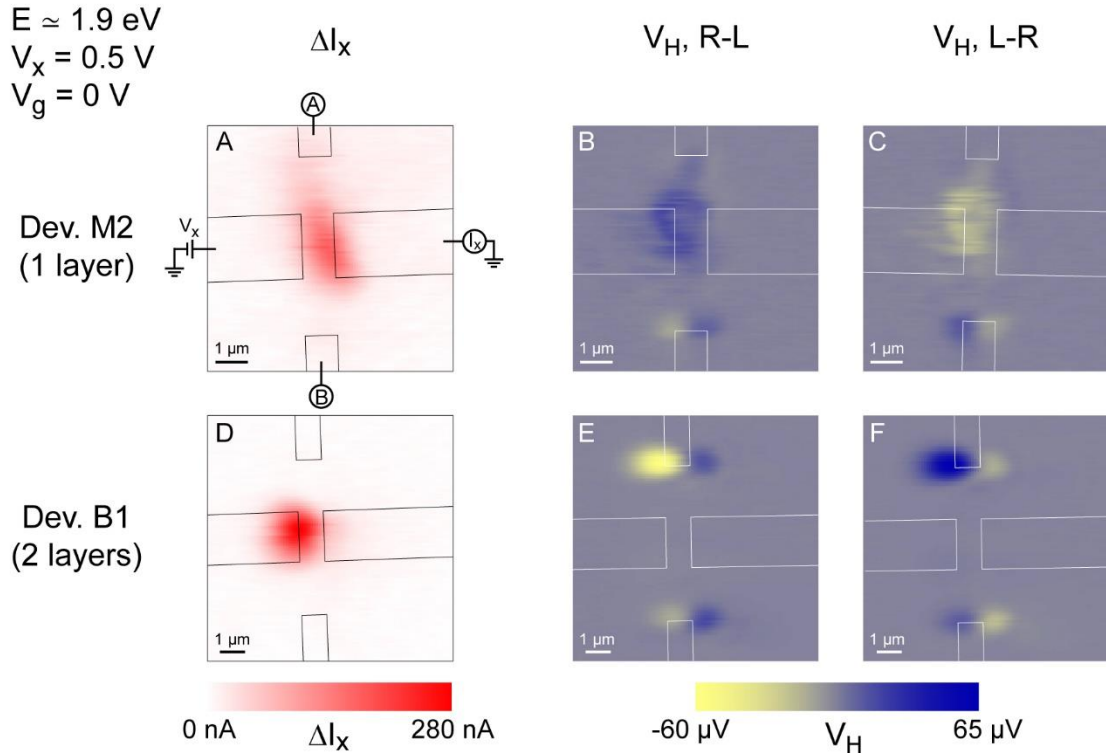


Figure 3.9: Response of monolayer vs. bilayer MoS₂ devices

(left) Scanning photocurrent (ΔI_x) map of monolayer device M2 and bilayer device B1. Contact pads indicated by black lines; measurement scheme depicted in upper left map. (right) Scanning Hall voltage (V_H) map under R-L and L-R modulation for a monolayer and bilayer devices, as labeled. Note that a Hall voltage is measured in the center of monolayer device M2 but not observed in bilayer device B1. All maps were taken on-resonance at incident light energy $E=1.9 \text{ eV}$, bias voltage $V_x=0.5 \text{ V}$, and gate voltage $V_g=0 \text{ V}$. Figure from Mak *et al.* (2014)¹.

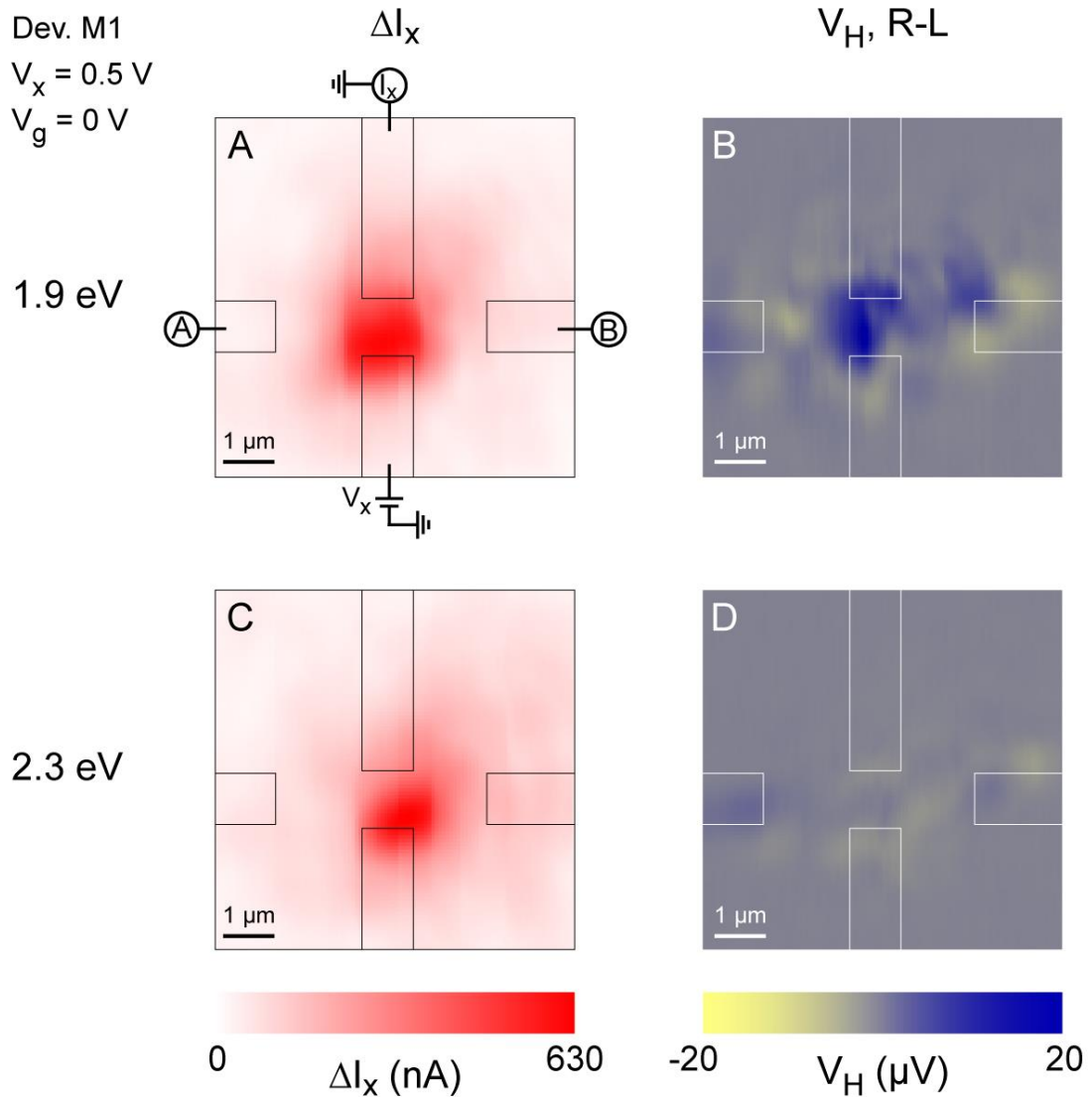


Figure 3.10: On- vs. off-resonance excitation in monolayer MoS₂ devices

(left) Scanning photocurrent (ΔI_x) map of monolayer device M1 under 1.9 and 2.3 eV excitation, as labeled. (right) Scanning Hall voltage (V_H) map under R-L modulation at 1.9 and 2.3 eV excitation, as labeled. Note that under off-resonance excitation (2.3 eV), the Hall voltage V_H vanishes. All maps taken at bias voltage $V_x=0.5 \text{ V}$ and gate voltage $V_g=0 \text{ V}$. Figure from Mak *et al.* (2014)¹.

eV. This supports our understanding that there *is* a carrier population imbalance generated by exciting monolayer devices with properly polarized light at the band gap, thereby selecting for one valley over the other, but that light (even with the same polarization) at higher energy does not significantly selectively populate one valley over the other.

3.9 Measurement of the Valley Hall Conductivity

In order to compare our results against the theoretical linear dependence of the valley Hall conductivity σ_H^v on the K and K' carrier imbalance δn_c (derived in App. C), we measure σ_H^v as a function of *the change in photoexcited carrier density* Δn_{ph} . We note that theoretically, if the change in conductivity is solely driven by the valley-polarized carriers excited by resonant, circularly polarized light, $\delta n_c = \Delta n_{ph}$; however, in a real system Δn_{ph} serves an upper bound on δn_c as it may include contributions from both valley-polarized *and* -unpolarized carriers. For reference, then, we are comparing our data to the slightly modified Eq. 2.10

$$\sigma_H^v = -\frac{e^2}{h} \frac{2\pi\hbar^2}{m_b E_g} \Delta n_{ph} \quad (3.1)$$

In order to estimate Δn_{ph} , we studied the laser intensity (P) dependence of the photoinduced AHE, as shown in Fig. 3.11. We first

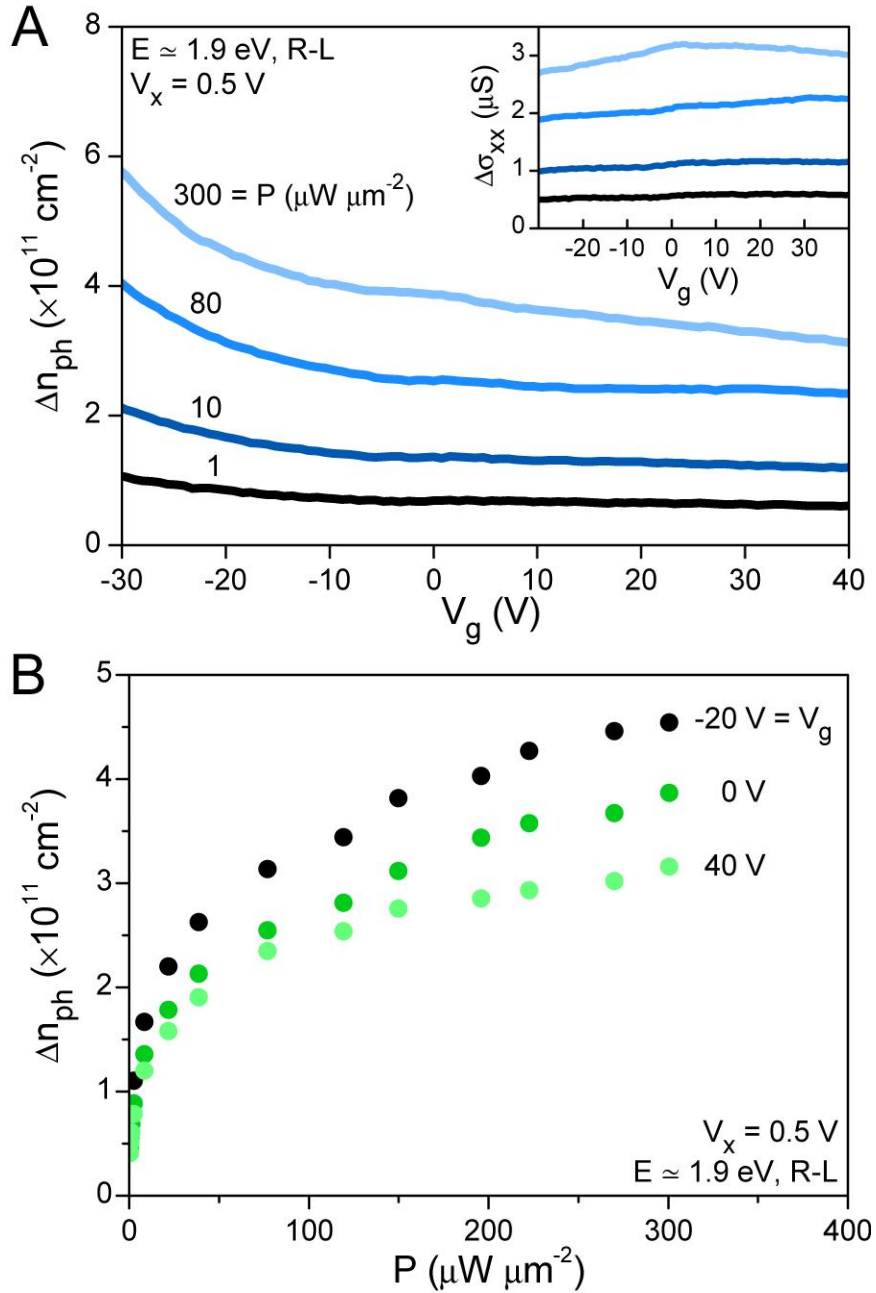


Figure 3.11: Photodoping dependence of monolayer MoS₂ devices

(a) (main) Photoexcited carrier density Δn_{ph} as a function of gate voltage V_g for various laser intensities P at a bias $V_x=0.5 \text{ V}$ and incident R-L illumination of energy $E=1.9 \text{ eV}$. (inset) The change in conductivity $\Delta\sigma_{xx}$ plotted against V_g at various intensities P . (b) Δn_{ph} as a function of P at various V_g , with the same excitation conditions as in (a). Figure from Mak *et al.* (2014)

measured the V_g dependence of the lateral conductivity $\Delta\sigma_{xx}$ under 1.9 eV R-L illumination of various intensities (inset, Fig. 3.11(a)). We then estimate the effective change in the photoexcited carrier density Δn_{ph} from the relation $\Delta\sigma_{xx} = e\mu\Delta n_{ph}$, where $\mu = \frac{1}{C_g} \frac{d\sigma_{xx}}{dV_g}$ is extracted from the dark electrical measurements presented in Fig. 3.3. The back-gate capacitance C_g is $\sim 1.2 \times 10^{-8} \text{F cm}^{-2}$. With these calculations, we are able to plot Δn_{ph} against V_g (main, Fig. 3.11(a)) at various illumination intensities. Likewise, we examine Δn_{ph} as a function of P at various V_g (Fig. 3.11(b)).

This analysis allows us to finally plot σ_H^v against Δn_{ph} at different values of V_g in Fig. 3.12 and to compare our results to the theory presented in Eq. 3.1, plotted in gray (in the limit $\delta n_c = \Delta n_{ph}$). For all gate voltages, σ_H^v increases linearly with Δn_{ph} , which is consistent with the theoretical prediction. The photoinduced anomalous Hall conductivity σ_H^v also has the right order of magnitude and approaches the theoretical value at high V_g . However, we do not currently understand the delayed onset discrepancy between our data and the theory. We also note that in the simplest case of $\delta n_c = \Delta n_{ph}$, we do not expect to observe a gate dependence as part of the relation (see Eq. 3.1), which is quite different from our experimental observations. One possible explanation of this discrepancy is the presence of

photoconduction mechanisms that are not due to the AHE, such as the relaxation of valley polarization in some of the carriers. Additionally, the slope of the σ_H^v versus Δn_{ph} curves keeps increasing with higher V_g and may go beyond the theoretical prediction. Unfortunately, the range of V_g applied in our experiment was limited by the breakdown of the back gate, so we were unable to explore this regime. A second possibility is a finite contribution from skew-scattering processes^{10,16}, which we neglected in Eq. 3.1 as negligible due to the non-pristine nature of our samples (see App. C). The relative importance of each of the intrinsic and extrinsic contributions depends on the sample quality (which in turn effects doping), so studies of the dependence on temperature and on disorder are therefore required to better understand the doping density dependence of the VHE.

3.10 Conclusions and research outlook

Our experimental results robustly support our interpretation of the measured Hall voltage as arising from the VHE. Briefly, the results are: (1) the sign of the Hall voltage corresponding to the handedness of the incident light; (2) the Hall resistance varying sinusoidally with the incident angle θ ; (3) the absence of a Hall voltage in inversion-symmetric bilayer devices; (4) the observation of a Hall voltage only for the on-resonance excitation energy of

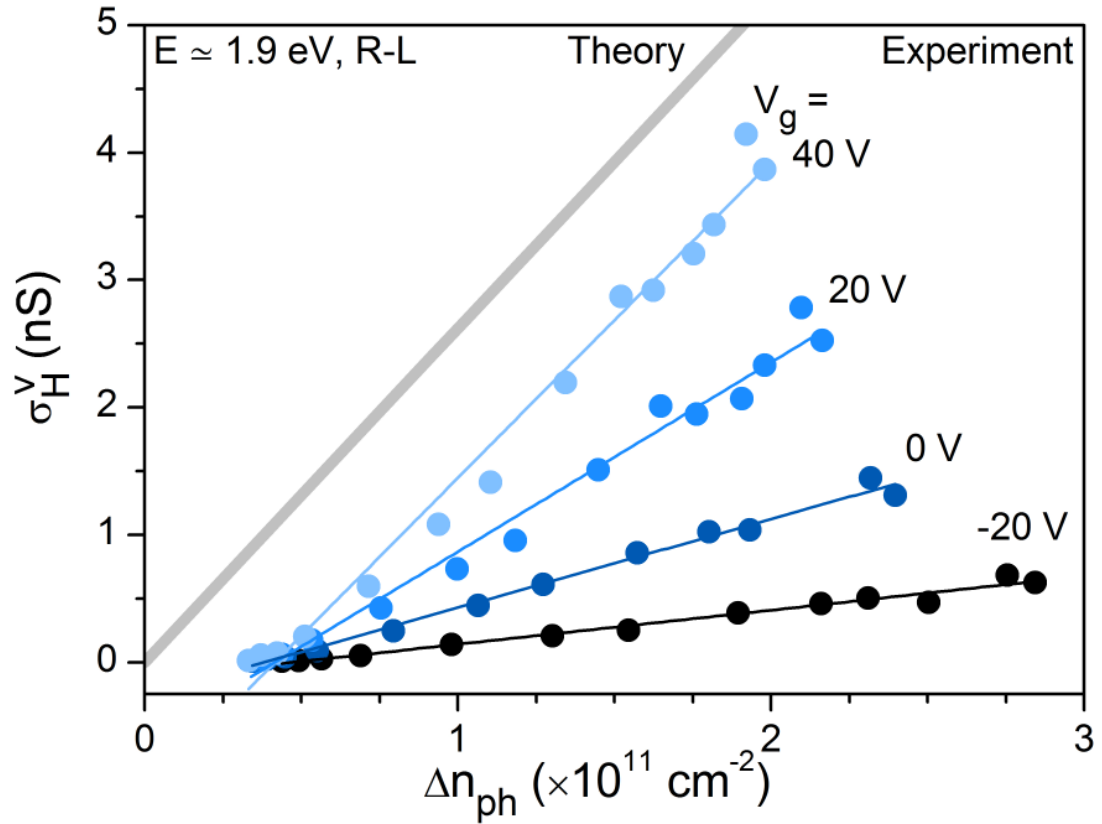


Figure 3.12: Comparison of experimental and theoretical Hall conductivity
Valley Hall conductivity σ_H^v as a function of the photoexcited carrier density Δn_{ph} in device M1 at a variety of gate voltages V_g . The theoretical prediction presented in Eq. 2.10 is graphed in gray. We note that at all gate voltages, $\sigma_H^v \propto \Delta n_{ph}$, with the slope for highly gated devices approaching that of the theoretical prediction. Unfortunately, due to dielectric breakdown, we were unable to push V_g higher than 40 V. Figure from Mak *et al.* (2014)³.

1.9 eV, which is the direct band-gap at the K and K' valleys of monolayer MoS₂; (5) the measurement of a valley Hall conductivity proportional to the density of excited carriers. The demonstration of a valley-sensitive photodetector represents an important advance for both fundamental condensed matter physics and the emerging area of valley-dependent electronics, which, since the 2014 publication of this work, includes the non-local detection of valley currents in graphene/hexagonal boron nitride (hBN) devices¹⁷, electrical control of the VHE in bilayer MoS₂¹⁸, and the engineering of ultralong lifetimes of valley-polarized carriers in tungsten diselenide (WSe₂)/MoS₂ heterostructures¹⁹. With these advances, “valleytronics” is a growing field that spans both the use of a new information carrier, the valley index, and the increasingly varied world of 2D materials as flexible optoelectronic devices.

References

1. Mak, K. F., McGill, K. L., Park, J. & McEuen, P. L. The valley Hall effect in MoS₂ transistors. *Science* **344**, 1489–1492 (2014).
2. Xiao, D., Liu, G.-B., Feng, W., Xu, X. & Yao, W. Coupled Spin and Valley Physics in Monolayers of MoS₂ and Other Group-VI Dichalcogenides. *Phys. Rev. Lett.* **108**, 196802 (2012).

3. Mak, K. F., He, K., Shan, J. & Heinz, T. F. Control of valley polarization in monolayer MoS₂ by optical helicity. *Nat. Nanotechnol.* **7**, 494–498 (2012).
4. Zeng, H., Dai, J., Yao, W., Xiao, D. & Cui, X. Valley polarization in MoS₂ monolayers by optical pumping. *Nat. Nanotechnol.* **7**, 490–493 (2012).
5. Mak, K. F., Lee, C., Hone, J., Shan, J. & Heinz, T. F. Atomically Thin MoS₂: A New Direct-Gap Semiconductor. *Phys. Rev. Lett.* **105**, 136805 (2010).
6. Baugher, B. W. H., Churchill, H. O. H., Yang, Y. & Jarillo-Herrero, P. Intrinsic Electronic Transport Properties of High-Quality Monolayer and Bilayer MoS₂. *Nano Lett.* **13**, 4212–4216 (2013).
7. Qiu, H. *et al.* Electrical characterization of back-gated bi-layer MoS₂ field-effect transistors and the effect of ambient on their performances. *Appl. Phys. Lett.* **100**, 123104 (2012).
8. Radisavljevic, B., Radenovic, A., Brivio, J., Giacometti, V. & Kis, A. Single-layer MoS₂ transistors. *Nat. Nanotechnol.* **6**, 147–150 (2011).
9. van der Pauw, L. J. A method of measuring the resistivity and Hall coefficient on lamellae of arbitrary shape. *Philips Tech. Rev.* **20**, 220–224 (1958).
10. Kioseoglou, G. *et al.* Valley polarization and intervalley scattering in monolayer MoS₂. *Appl. Phys. Lett.* **101**, 221907 (2012).
11. Lopez-Sanchez, O., Lembke, D., Kayci, M., Radenovic, A. & Kis, A. Ultrasensitive photodetectors based on monolayer MoS₂. *Nat. Nanotechnol.* **8**, 497–501 (2013).

12. Xiao, D., Yao, W. & Niu, Q. Valley-Contrasting Physics in Graphene: Magnetic Moment and Topological Transport. *Phys. Rev. Lett.* **99**, 236809 (2007).
13. Cao, T. *et al.* Valley-selective circular dichroism of monolayer molybdenum disulphide. *Nat. Commun.* **3**, 887 (2012).
14. Sallen, G. *et al.* Robust optical emission polarization in MoS₂ monolayers through selective valley excitation. *Phys. Rev. B* **86**, 081301 (2012).
15. Wu, S. *et al.* Electrical tuning of valley magnetic moment through symmetry control in bilayer MoS₂. *Nat. Phys.* **9**, 149–153 (2013).
16. Nagaosa, N., Sinova, J., Onoda, S., MacDonald, A. H. & Ong, N. P. Anomalous Hall effect. *Rev. Mod. Phys.* **82**, 1539–1592 (2010).
17. Gorbachev, R. V. *et al.* Detecting topological currents in graphene superlattices. *Science* **346**, 448–451 (2014).
18. Lee, J., Mak, K. F. & Shan, J. Electrical control of the valley Hall effect in bilayer MoS₂ transistors. *Nat. Nanotechnol.* **11**, 421–425 (2016).
19. Kim, J. *et al.* Observation of ultralong valley lifetime in WSe₂-MoS₂ heterostructures. *Sci. Adv.* **3**, e1700518 (2017).

CHAPTER 4

MEASURING THE BENDING STIFFNESS OF GRAPHENE

4.1 Introduction

In Ch. 3 we explored the experimental demonstration of the photoinduced anomalous Hall effect in the two-dimensional (2D) material monolayer molybdenum disulfide (MoS_2). In this chapter we are shifting our focus in both the physics and 2D material of interest from the AHE in MoS_2 to the mechanics of graphene. Specifically, we will be exploring two distinct approaches for directly measuring the bending stiffness of graphene fabricated into cantilevers: one taking advantage of the Brownian motion of the cantilever, and one using radiation pressure to obtain a force-distance curve. The methods here presented are refinements of those presented in Melina Bles's Ph.D. dissertation (2015)¹, and they were ultimately published as part of Bles *et al.* (2015)². As part of our analysis, we compare our measurements to measurements based on the force of gravity acting on the cantilever, which were initially presented in Bles (2015)¹ and published in Bles *et al.* (2015)². Note that the text of this chapter is an expansion of the bending stiffness section of Bles *et al.* (2015)².

4.2 Experimental approach to measuring the bending stiffness

In this section we describe our general approach to measuring the bending stiffness of graphene, leaving fabrication, setup, and measurement method details for Secs. 4.3-4.5. The graphene device release procedure detailed below makes it possible to freely manipulate graphene beyond its two-dimensional plane and into the third dimension, much as you can bend a piece of paper in three dimensions. By attaching gold (Au) pads to the ends of graphene strips to facilitate the movement of graphene in the third dimension, we can use several distinct techniques to measure the bending stiffness of graphene. Fig. 4.1(a) shows a labeled white light transmission image of graphene cantilevers resting on a fused silica substrate. The black rectangles are the Au pads, while the gray rectangles are the graphene.

To conduct our measurements, we push a microprobe into one of the gold pads on the graphene cantilever and peel or lift the device off the surface (Fig. 4.1(b)). (Even though the graphene crumples significantly during this process, it is almost entirely reversible in the presence of surfactants².) The device then hangs from the microprobe, primarily shaped by the force of gravity acting on the free gold pad (see Fig. 4.6(a)). From this initial position, we can obtain the spring constant k of a device by measuring the deflection caused by gravity, the radiation pressure needed to counteract

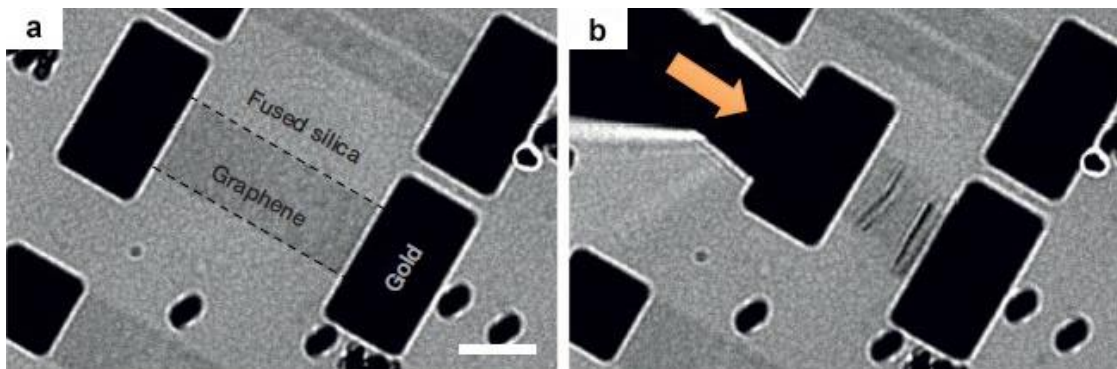


Figure 4.1: Release of graphene cantilevers from substrate

(a) An image of graphene cantilever devices resting on the fused silica surface after release, but before any attempt at pick-up. (b) We push on one of the gold pads with a microprobe (orange arrow) and scrunch up the device to further release it before picking it up off the surface. In the presence of surfactants, the effects of this motion are almost entirely reversible. Scale bar 10 μm . Figure from Blee *et al.* (2015)².

the force of gravity, or the Brownian motion of the free gold pad in the water.

Once we extract the spring constant k of the cantilever, we infer the bending stiffness κ by using the relation

$$\kappa = \frac{kL^3}{3W} \quad (4.1)$$

where L is the length of the cantilever and W is its width. Equation 4.1 is derived from the classical beam mechanics³ for a massless beam (the graphene) with a mass fixed on one end (the free gold pad) and the relationship

$$\kappa = \frac{Yt^3}{12(1 - \sigma^2)} \quad (4.2)$$

derived in Landau and Lifshitz (1986)⁴ by minimizing the free energy of a thin bent plate, and in which Y is the Young's modulus, t is the thickness of the cantilever, and σ is the Poisson's ratio of the cantilever material. (In the case of graphene, $\sigma = 0.17$ and is thus negligible⁵.)

4.3 Fabrication and characterization of graphene devices

We fabricate graphene cantilevers with lengths ranging from 8-80 μm and widths from 2-15 μm . We begin fabrication by growing polycrystalline monolayer graphene on copper foil via chemical vapor deposition (CVD)⁶.

We purchased the copper foil from Alpha Aesar, stock number 13382. After annealing the copper at 980 °C for 36 minutes in hydrogen gas (H₂) flowing at 60 sccm, graphene was grown at 980 °C for 20 min in a flow environment of 60 sccm H₂ and 36 sccm methane (CH₄). The foil was then cooled in the same environment as quickly as possible.

We use a variety of microscopies to characterize the graphene, and we present a typical scanning electron microscope (SEM) image, Raman spectrum, and bright- and dark-field transmission electron microscope (TEM) images in Fig. 4.2. The Raman spectrum was taken on CVD graphene that we transferred to a 285-nm-silicon-dioxide/silicon (SiO₂/Si) substrate. The spectrum shows graphene's characteristic G peak at 1,580 cm⁻¹ and two-dimensional (2D) peak at 2,700 cm⁻¹; the ratio between the two⁷ confirms that we used primarily monolayer graphene in the fabrication of our devices. Additionally, a small D peak at 1,350 cm⁻¹ indicates low disorder. (The small peak at 2,450 cm⁻¹ is background.) The high-contrast bright-field TEM image of graphene transferred over 10-nm-thick silicon nitride (Si₃N₄) windows confirms that we are working with continuous monolayer graphene. Dark-field TEM on a variety of growths revealed that typical grain sizes were on the order of hundreds of nanometers to microns (as seen Fig. 4.2(d)). (Larger-scale variations in contrast in the SEM image,

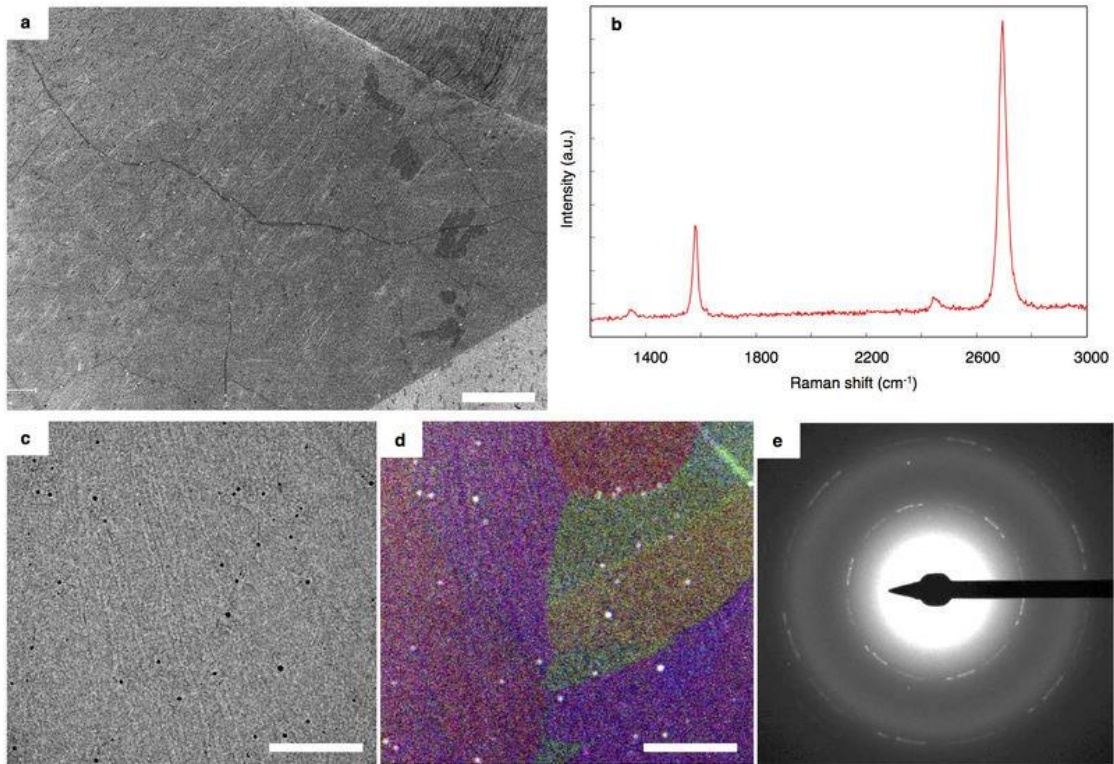


Figure 4.2: Graphene characterization

(a) SEM of CVD graphene on copper foil. Scale bar 10 μm . (b) Raman spectrum of CVD graphene transferred onto an SiO_2/Si substrate. We see graphene's characteristic G peak at $1,580\text{ cm}^{-1}$ and 2D peak at $2,700\text{ cm}^{-1}$, with their ratio indicating it is monolayer. (c) High-contrast bright-field TEM of graphene on a Si_3N_4 window showing continuous monolayer graphene. Scale bar 1 μm . (d) False-color composite dark-field TEM version of (c), showing graphene grain size and shape. Scale bar 1 μm . (e) TEM diffraction pattern for the region shown in (c) and (d). Figure from Blee *et al.* (2015)².

Fig. 4.2(a), are the copper grains present in the foil used for CVD growth.) All graphene used in the following experiments consisted of monolayer graphene with some small bilayer patches, similar to that shown in Fig. 4.2. We used standard graphene processing methods on top of fused silica chips that had a 40 nm-aluminum release layer evaporated onto them. We spin 2% poly(methyl methacrylate) onto the graphene to both protect and support it during transfer. After etching the copper away from the graphene in ferric chloride (Transene CE-200), we rinse the graphene in five consecutive deionized water baths before finally transferring it onto the aluminum-coated chips. We soak the chips in acetone overnight to remove the PMMA, leaving us with chips ready for cleanroom processing. We use photolithography to pattern the device pads and evaporate 50 nm of gold to form them. We then pattern the graphene strips and etch away the unwanted graphene in oxygen plasma for 25 seconds. Before conducting experiments, we soak the chip in a 10:1 deionized water:hydrochloric acid (HCl) solution until the aluminum release layer has completely disappeared. The graphene devices are now resting on the surface of the fused silica; after transferring the chips directly into deionized water, we are ready to conduct our experiments.

As shown by the atomic force microscope (AFM) images presented in

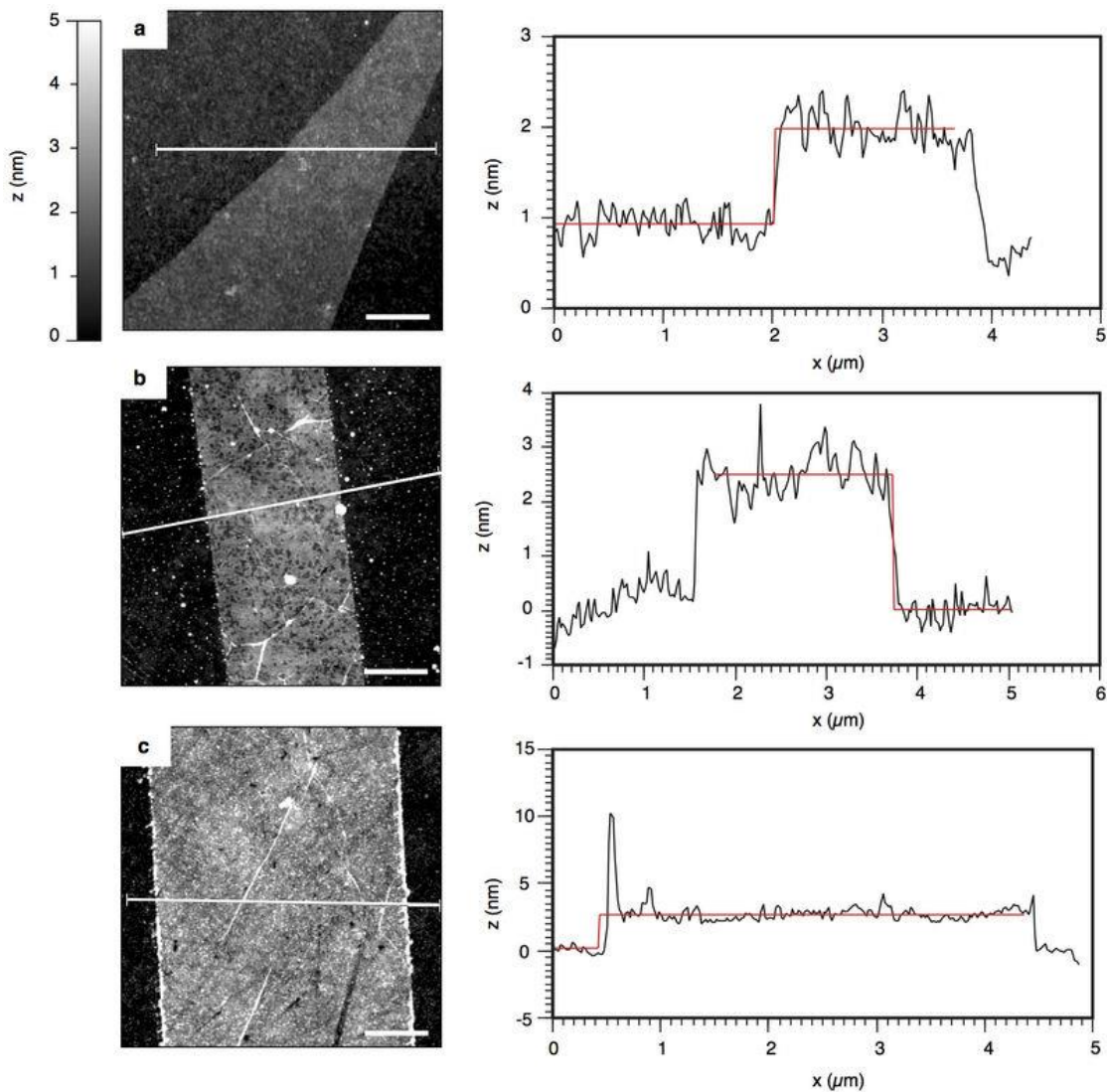


Figure 4.3: AFM of graphene samples

(a) AFM of a pristine exfoliated graphene sample. (b) and (c) Representative CVD graphene samples that have been through the entire device fabrication procedure (prior to release). AFM height in z for all images indicated to the left of (a). All scale bars $1 \mu\text{m}$. Figure from Bles *et al.* (2015)².

Fig. 4.3, it is impossible to completely avoid polymer residues from these standard transfer and fabrication methods. We measure a ~ 2 -nm-thick layer of PMMA on top of our graphene after processing. The stiffest PMMA⁸ has a Young's modulus $Y = 3.1$ GPa and a Poisson ratio $\sigma = 0.4$, adding only ~ 30 eV to the measured stiffness (since $\kappa = Yt^3/[12(1 - \sigma^2)]$), which is negligible compared to the measured values we present below.

4.4 Radiation pressure measurement method

The first method by which we measure the bending stiffness of graphene is by using the radiation pressure from a 1,064-nm infrared laser to counteract the buoyant force and the force of gravity acting on the free end of a suspended graphene cantilever. This schema is visualized in Fig. 4.4(a), in which the grey triangle represents the probe tip that holds the device above the substrate and the red triangle represents the focused laser beam. We calibrated the force produced by our laser by balancing the applied radiation pressure against the known weight and buoyancy of the cantilever's free gold pad. For our measurements, we focused the laser on the center of the free gold pad and adjusted its power with an acousto-optic modulator.

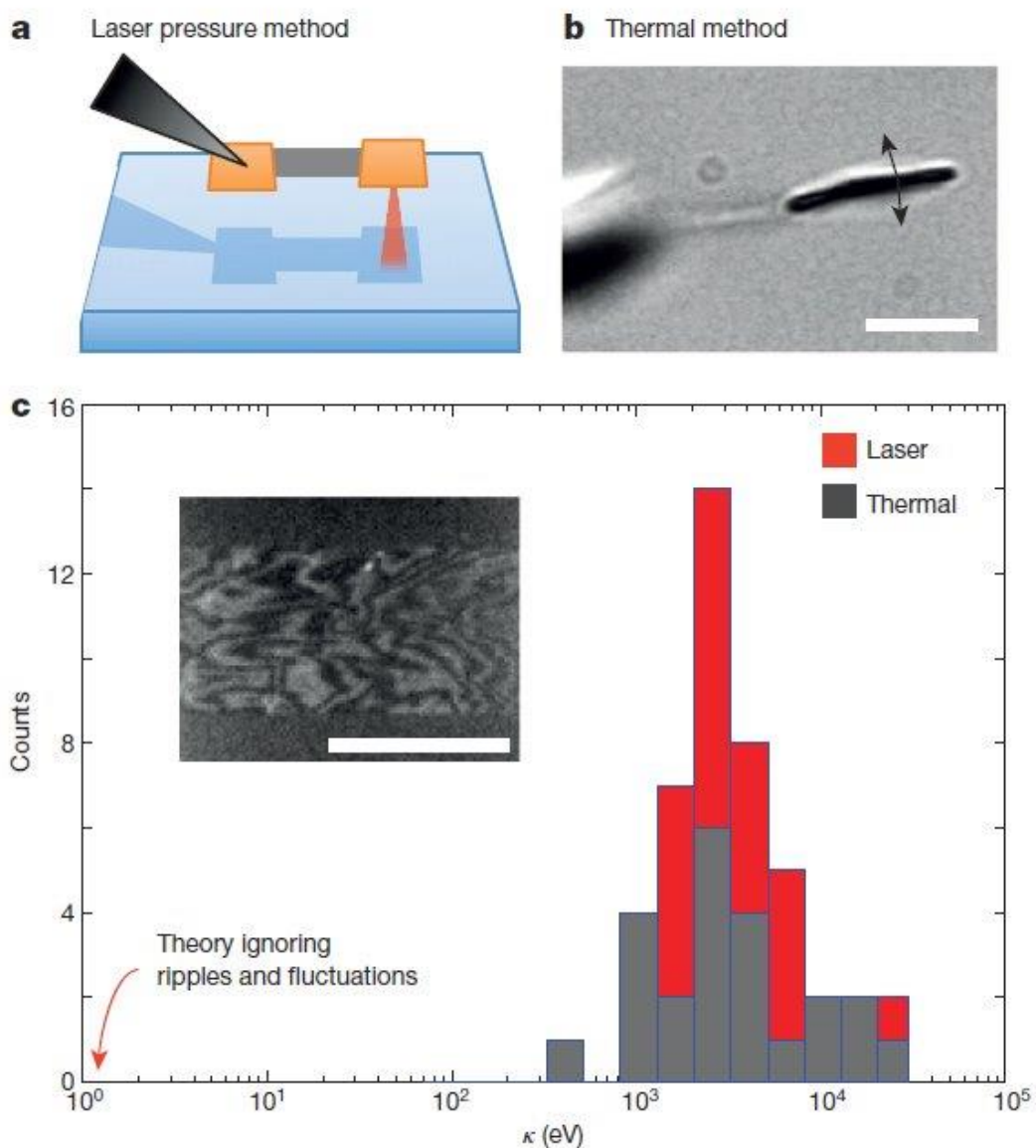


Figure 4.4: Measuring the bending stiffness of graphene

(a) Schematic demonstrating the laser pressure method for measuring the bending stiffness of graphene. (b) Image of a cantilever device turned on its side so that the camera can record its Brownian motion, from which we extract the bending stiffness of graphene. (c) Histogram of bending stiffness measurements from the laser (red) and thermal (grey) measurements. The theoretical bending stiffness for (flat) graphene is indicated at 1 eV. (inset) An interferometric image of graphene lying on a fused silica substrate after the Al release layer has been etched away, showing the static ripples present in the graphene. All scale bars are 10 μm . Figure from Blees *et al.* (2015)².

We were then able to record force-displacement curves for the cantilevers and determine k from the linear fits of the collected data. The z-displacement of the cantilevers was measured using a piezo attached to the objective of the optical microscope.

4.5 Thermal motion measurement method

We made an independent measurement of cantilever spring constants by capitalizing on the Brownian motion of the free gold pad. For these measurements, we rotated the microprobe until we could see the attached cantilever edge-on; this allowed us to record the thermal fluctuations of the free pad in the x - y plane, as shown in Fig. 4.4(b). (We note that, although the aqueous environment slows down the fluctuations, based on preliminary experiments, it does not change the spring constant of the cantilever.) We recorded the motion at 90 fps for ~ 20 min to ensure that we sampled the entire phase space of the cantilever's motion. The first 20 seconds from the trace of the free gold pad on a $40\ \mu\text{m} \times 10\ \mu\text{m}$ cantilever are shown in the Fig. 4.5(a). We tracked the motion of the pad centroid in a frame-by-frame image analysis to extract the x position of the pad over time, with the x direction taken as perpendicular to the profile of the free gold pad (see inset of Fig. 4.5(a)).

To extract the time-averaged square of the cantilever's thermal motion, $\langle x_{th}^2 \rangle$, we calculated the power spectral density (PSD) (the Fourier transform of the autocorrelation of the data) for each cantilever; a representative example is shown in Fig. 4.5(b). In all devices we observed low-frequency $1/f$ noise from the long-timescale motion of the supporting probe (shown in red). This low-frequency noise was excluded from further analysis. We fit the data plotted in blue, which resulted from the thermal motion of the free gold pad, with the theoretical one-sided PSD for Brownian thermal motion^{9,10} (dashed line):

$$S_{xx}(f) = \frac{S_o}{1 + \left(\frac{f}{f_c}\right)^2} \quad (4.3)$$

where S_o is the low-frequency value of the Brownian motion PSD, and f_c is the corner frequency. The integral of this fitting function gives us $\langle x_{th}^2 \rangle$:

$$\int_0^\infty S_{xx}(f) df = \langle x_{th}^2 \rangle \quad (4.4)$$

Finally, using the equipartition theorem (noting that we only have one degree of freedom for the cantilever motion), we calculate $k = k_B T / \langle x_{th}^2 \rangle$ where T is temperature and k_B is Boltzmann's constant.

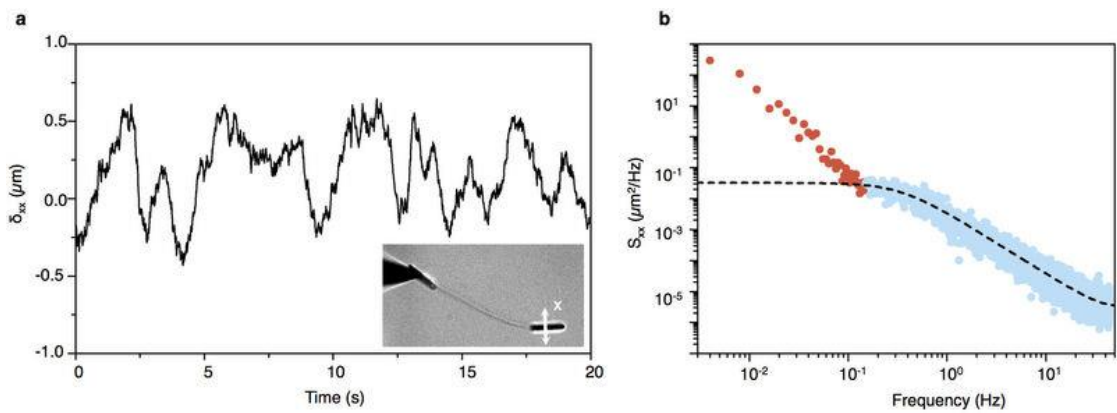


Figure 4.5: Thermal motion bending stiffness measurement

(a) A time trace from a typical device. The low-frequency fluctuations are due to the movement of the support probe; the high-frequency fluctuations are the Brownian motion of the pad. (inset) Image of the device recorded in the time trace. We extracted the fluctuations in the x direction (perpendicular to the plane of the pad) from the videos. (b) PSD of the data presented in (a). We exclude the low-frequency data plotted in red and fit the data in blue with Eq. 4.3. Figure from Blees *et al.* (2015)².

4.6 Comparison with gravitational measurement method

We compare our data with the gravitational measurements detailed in Bles (2015)², which consisted of rough measurements of k using the observed deflection of the cantilever from the forces acting on the gold pads (namely, gravity and the buoyant force; see Fig. 4.6(a)). These measurements were repeated for a variety of devices of varying length L and width $W = 10 \mu\text{m}$, as shown in Fig. 4.6(b). One important observation impacting the gravitational measurements was that the cantilevers would sometimes have a built-in curvature downwards, likely due to residual fabrication materials or strains in the graphene. As can be seen in the histogram (inset, Fig. 4.6(b)) comparing laser (red), thermal (black), and gravitational (blue) measurements, the extracted gravitational κ are systematically shifted below those of the laser and thermal κ . These results are consistent with our observations of pre-existing downward curvature in many of our devices, and are again highlighted by the starred data points in Fig. 4.6(b), which show the spring constant measured by each method on the same device.

4.7 Comparison with theoretical predictions

Measurements of the phonon modes in graphite¹¹ and simulations of bending graphene¹² predict the microscopic bending stiffness $\kappa_0 \approx 1.2 \text{ eV}$.

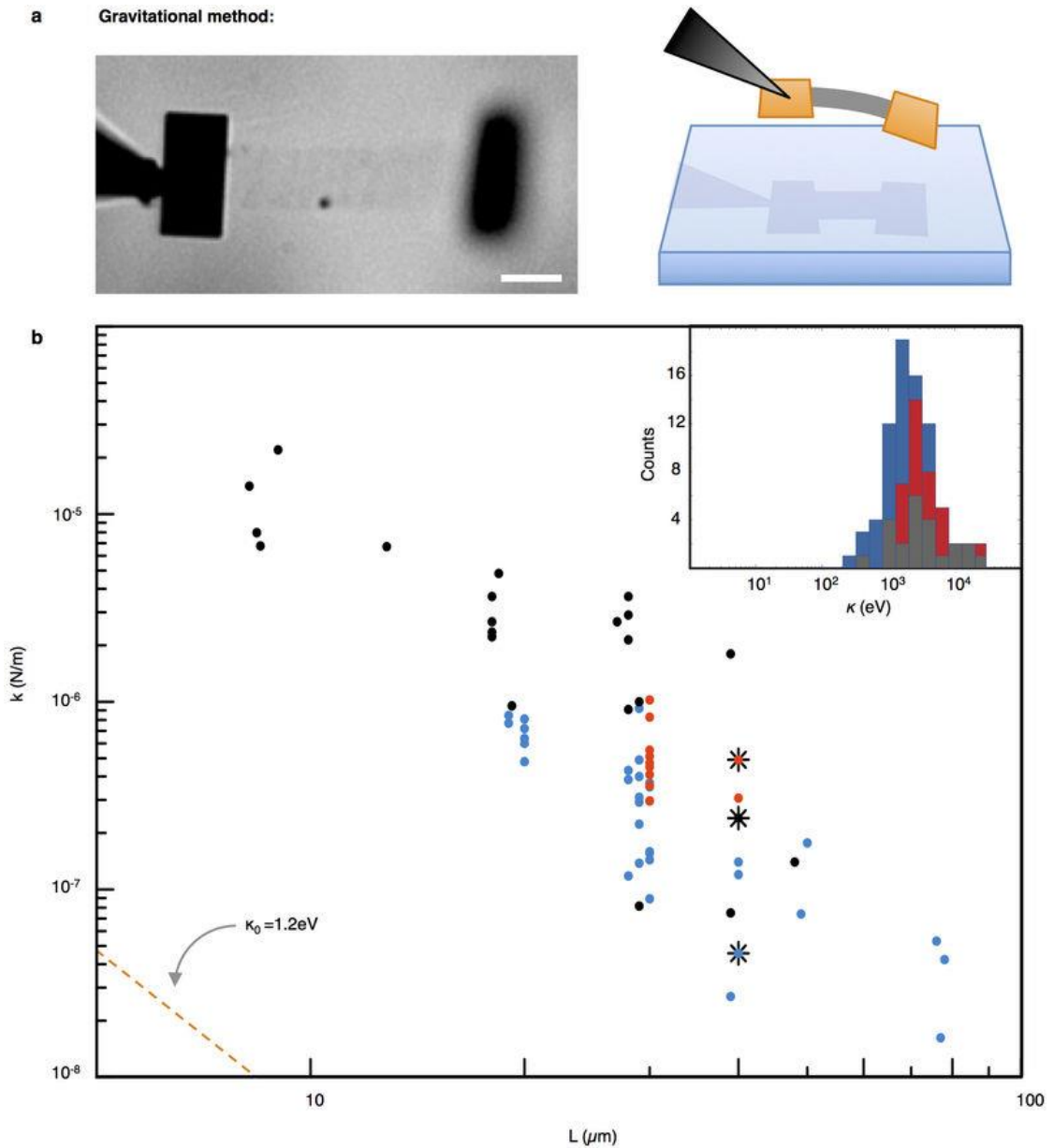


Figure 4.6: Comparison of bending stiffness measurement methods

(a) An image of a device hanging freely from the support probe under the force of gravity. The out-of-focus pad is below the in-focus support pad, as shown in the schematic version to the left. (b) Plot of spring constant k as a function of devices of various lengths L and width $W=10 \mu\text{m}$. Black dots: thermal measurements; Red dots: radiation pressure measurements; Blue dots: gravitational measurements; Stars: each measurement method used on the same device. (inset) Histogram of bending stiffness measurements from Fig. 4.4(c), including the gravitational measurements in blue. Note the displacement of the gravitational measurements relative to both the thermal and radiation pressure measurements. Figure from Blees *et al.* (2015)².

As can be seen in Fig. 4.6(b), our measurements of κ are a full three orders of magnitude higher than this prediction. Looking to the literature, we note that both thermal fluctuations and static ripples are predicted to notably stiffen ultrathin crystalline membranes^{13–19} by effectively thickening the membrane. (This is similar to how a crumpled sheet of paper is more rigid than an uncrumpled sheet.)

For static ripples, the effective bending stiffness is predicted to be¹³

$$\frac{\kappa_{eff}}{\kappa_o} = \sqrt{\frac{Y_{2D}\langle z_{eff}^2 \rangle}{\kappa_o}} \quad (4.5)$$

where $\langle z_{eff}^2 \rangle$ is the space-averaged square of the effective amplitude of the static ripples and $Y_{2D} = 340 \text{ N m}^{-1}$ is the two-dimensional Young's modulus²⁰. We look for static ripples in graphene cantilevers using interference microscopy²¹, as shown in the inset of Fig. 4.4(c). The black bands are regions of constant elevation, with the spacing between black and white bands corresponding to changes in z of $\lambda/4 = 82 \text{ nm}$ (where $\lambda = 436 \text{ nm}/1.33 = 327 \text{ nm}$ is the wavelength, corrected for the refractive index of water). We used a 10-nm full-width-at-half-maximum (FWHM) bandpass filter with a center wavelength of 430 nm on the 436-nm line of a mercury arc lamp for our interferometric measurements. Based on the thin-film equations, the reflectivity of the glass–water–graphene–water cavity changes

from 0.0026 to 0.0067 between dark and light bands. A single sheet of graphene in water has a reflectivity of 0.0002, so our geometry greatly enhances the visibility of graphene in this imaging mode. With $\langle z_{eff}^2 \rangle \approx (100 \text{ nm})^2$ a typical value from these measurements, we obtain an effective bending stiffness of $\kappa_{eff}/\kappa_o \approx 4,000$. We note that static ripples are present only after releasing graphene from the surface (inset of Fig. 4.4(c)), and likely to be sample-specific and influenced by growth, fabrication details, and release procedures. Other groups have observed ripples in suspended (strained) graphene membranes^{22,23}. However, they occur at a much smaller scale, and their origin remains a subject of debate.

For an initially flat membrane with thermal fluctuations, the stiffness is predicted to be

$$\frac{\kappa_{eff}}{\kappa_o} \approx \left(\frac{W}{l_c}\right)^\eta \quad (4.6)$$

where

$$l_c = \sqrt{\frac{32\pi^2\kappa_o^2}{3Y_{2D}k_B T}} \quad (4.7)$$

is the Ginzburg length¹⁸, and η is a scaling exponent. This thermal theory predicts a bending stiffness at room temperature due to thermal fluctuations of $\kappa_{eff}/\kappa_o \approx 1,000$ for an initially flat membrane. Taken with the possible influence of static wrinkles on graphene membrane stiffness, we cannot at

this time establish the relative contributions of each mechanism²⁴; we note that, however, both of these mechanisms result in contributions of order 10^3 times greater than κ_o , which agrees with our experimental findings.

4.8 Applications and future directions

Measuring the bending stiffness of graphene allows us to compare graphene as a microscopic membrane to macroscopic membranes such pieces of paper by making use of the Föppl-von Kármán number^{25,26} γ , a ratio relating the 2D Young's modulus Y_{2D} of a square membrane to its out-of-plane bending stiffness κ and scaled by its length L . Materials with similar Föppl-von Kármán numbers are expected to behave in mechanically similar ways. For graphene, based on our measurements and the proper scaling^{13,15} of $Y_{2D} \rightarrow Y_{eff}$, the effective Föppl-von Kármán number $\gamma_{eff} = Y_{eff}L^2/\kappa_{eff}$ is of order 10^5 - 10^7 for a $10 \mu\text{m} \times 10 \mu\text{m}$ graphene sheet. This is close to γ for a standard piece of printer paper, which means that we can get mechanical intuition for how various micropatterned forms will respond to manipulation by playing with identically shaped (macroscopic) pieces of paper.

Graphene is only one of several 2D materials of mechanical, electrical, and optical interest – along with, for example, molybdenum disulfide (MoS_2)

or boron nitride (BN), a semiconductor and insulator, respectively. Since the publication of Blees *et al.* (2015)², researchers have even created releasable ultrathin materials via atomic layer deposition (ALD)²⁷. The approach and techniques developed in measuring the bending stiffness of graphene apply to all such 2D materials and allow for the development of creative applications, such as environment-responsive bimorphs²⁸ or chemically-tagged devices²⁹. With actuation possibilities including the use of magnetic fields and light, 2D devices can be used for in, for example, sensing applications, and as the basis of micro- and/or nanorobotics.

References

1. Blees, M. K. Graphene as atomic paper: From bending stiffness to mechanical metamaterials. (Cornell University, 2015).
2. Blees, M. K. *et al.* Graphene kirigami. *Nature* **524**, 204–207 (2015).
3. Livermore, C. Course Materials for 6.777J / 2.372J Design and Fabrication of Microelectromechanical Devices, Spring 2007. *MIT OpenCourseWare* Available at: <http://ocw.mit.edu/>. (Accessed: 27th June 2018)
4. Landau, L. D. & Lifshitz, E. M. *Theory of Elasticity*. **7**, 38-86 (Elsevier, 1986).
5. Song, T. T. *et al.* The stability of aluminium oxide monolayer and its interface with two-dimensional materials. *Sci. Rep.* **6**, 29221 (2016).

6. Li, X. *et al.* Graphene Films with Large Domain Size by a Two-Step Chemical Vapor Deposition Process. *Nano Lett.* **10**, 4328–4334 (2010).
7. Ferrari, A. C. *et al.* Raman Spectrum of Graphene and Graphene Layers. *Phys. Rev. Lett.* **97**, 187401 (2006).
8. PMMA. *MIT Material Property Database* Available at: <http://www.mit.edu/~6.777/matprops/pmma.htm>. (Accessed: 1st June 2018)
9. te Velthuis, A. J. W., Kerssemakers, J. W. J., Lipfert, J. & Dekker, N. H. Quantitative Guidelines for Force Calibration through Spectral Analysis of Magnetic Tweezers Data. *Biophys. J.* **99**, 1292–1302 (2010).
10. Velasco, S. On the Brownian motion of a harmonically bound particle and the theory of a Wiener process. *Eur. J. Phys.* **6**, 259–265 (1985).
11. Nicklow, R., Wakabayashi, N. & Smith, H. G. Lattice Dynamics of Pyrolytic Graphite. *Phys. Rev. B* **5**, 4951–4962 (1972).
12. Fasolino, A., Los, J. H. & Katsnelson, M. I. Intrinsic ripples in graphene. *Nat. Mater.* **6**, 858–861 (2007).
13. Košmrlj, A. & Nelson, D. R. Mechanical properties of warped membranes. *Phys. Rev. E* **88**, 012136 (2013).
14. Nelson, D. R. & Peliti, L. Fluctuations in membranes with crystalline and hexatic order. *J. Phys.* **48**, 1085–1092 (1987).
15. Aronovitz, J. A. & Lubensky, T. C. Fluctuations of Solid Membranes. *Phys. Rev. Lett.* **60**, 2634–2637 (1988).
16. Le Doussal, P. & Radzihovsky, L. Self-consistent theory of polymerized membranes. *Phys. Rev. Lett.* **69**, 1209 (1992).

17. Los, J. H., Katsnelson, M. I., Yazyev, O. V., Zakharchenko, K. V. & Fasolino, A. Scaling properties of flexible membranes from atomistic simulations: Application to graphene. *Phys. Rev. B* **80**, 121405 (2009).
18. Roldán, R., Fasolino, A., Zakharchenko, K. V. & Katsnelson, M. I. Suppression of anharmonicities in crystalline membranes by external strain. *Phys. Rev. B* **83**, 174104 (2011).
19. Braghin, F. L. & Hasselmann, N. Thermal fluctuations of free-standing graphene. *Phys. Rev. B* **82**, 035407 (2010).
20. Lee, C., Wei, X., Kysar, J. W. & Hone, J. Measurement of the Elastic Properties and Intrinsic Strength of Monolayer Graphene. *Science* **321**, 385–388 (2008).
21. Georgiou, T. *et al.* Graphene bubbles with controllable curvature. *Appl. Phys. Lett.* **99**, 093103 (2011).
22. Meyer, J. C. *et al.* The structure of suspended graphene sheets. *Nature* **446**, 60–63 (2007).
23. Wang, W. L. *et al.* Direct Imaging of Atomic-Scale Ripples in Few-Layer Graphene. *Nano Lett.* **12**, 2278–2282 (2012).
24. Košmrlj, A. & Nelson, D. R. Thermal excitations of warped membranes. *Phys. Rev. E* **89**, 022126 (2014).
25. Föppl, A. *Vorlesungen über technische Mechanik*. (Leipzig, B. G. Teubner, 1897).
26. Von Kármán, T. *Festigkeitsprobleme im maschinenbau*. (1910).
27. Davami, K. *et al.* Ultralight shape-recovering plate mechanical metamaterials. *Nat. Commun.* **6**, 10019 (2015).

28. Miskin, M. Z. *et al.* Graphene-based bimorphs for micron-sized, autonomous origami machines. *Proc. Natl. Acad. Sci.* 201712889 (2018). doi:10.1073/pnas.1712889115

29. Miskin, M. Z., Sun, C., Cohen, I., Dichtel, W. R. & McEuen, P. L. Measuring and Manipulating the Adhesion of Graphene. *Nano Lett.* **18**, 449–454 (2018).

CHAPTER 5

ENCAPSULATION OF MICRODROPLETS WITH TWO-DIMENSIONAL MATERIALS

5.1 Introduction

In Ch. 4 we examined the bending stiffness of graphene by using a novel technique to pick up graphene sheets in water so that we could manipulate them in three dimensions, much like bending a sheet of paper^{1,2}. This technique allows us to start viewing graphene and other two-dimensional (2D) materials as not simply planar, but as potentially offering form and function in our fully three-dimensional (3D) world. In realizing this transition from 2D to 3D, the action of bending comes to mind as a typical 2D-to-3D manipulation. In considering other ways in which we interact with macroscopic planar sheets, the actions of folding and wrapping present themselves as further-refined versions of bending – i.e. to initiate either folding or wrapping, you must first bend your planar sheet.

In this chapter, we will examine the wrapping of microdroplets by atomically thin materials. For this endeavor we draw on the rich literature that explores wrapping^{3–7} and capillary origami^{8–12} at the macroscale. Here, “macroscopic” droplets are on the order of millimeters, with the wrapping materials as thin as tens of nanometers. In contrast, as we will see, our

experiment wraps droplets tens of *microns* in scale, with materials that are atomically thin.

At only a few atoms thick, these materials exist in the limit of high bendability: they will bend without stretching to minimize their surface energy^{3,6}. As we mentioned in Ch. 4, the bending energy κ is defined as¹³

$$\kappa = \frac{Yt^3}{12(1 - \sigma^2)} \quad (4.2)$$

where Y is the Young's modulus, t is the thickness of the sheet, and σ is the Poisson's ratio of the material. Paulsen *et al.* (2015)³ establish the high-bendability regime as

$$\frac{\kappa}{W^2} \ll \gamma \ll E \quad (5.1)$$

where W is the radius of the sheet, γ is the interfacial tension between the sheet and the wrapped material, and $E = Yt$ is the stretching modulus of the sheet. Combining the results of our graphene bending stiffness measurement² with theoretical work on the bending stiffness of monolayer molybdenum disulfide (MoS_2) indicating that the individual Mo and S layers have a similar bending stiffness to that of graphene¹⁴, we approximate the bending stiffness of atomically thin materials as $\sim 1 \text{ keV} \approx 10^{-16} \text{ J}$. For interfacial tensions $\gamma \sim \sigma(10^{-2}) \text{ N/m}$ and theoretical stretching moduli¹⁵

$E \sim \sigma(10^2)$ N/m, atomically thin materials with sheet radii $W \sim \sigma(10^1-10^2)$ μm are well within this high-bendability limit.

Given that we are operating in the same limit as macroscopic wrapping experiments^{3,4}, we can investigate whether or not similar wrapping states exist at the microscale as at the macroscale. An example of these macroscopic wrapped states is presented in Fig. 5.1, from Paulsen *et al.* (2015)³. One of the findings of this work, which placed highly-bendable polymer sheets on shrinking drops of water in a silicone oil environment, was that progressively-wrapped droplets morphed from spherical into prismatic shapes at complete wrapping.

With these experiments in mind, we proceed to describe the fabrication of our atomically thin sheets and our setup for observing microdroplet wrapping dynamics.

5.2 MoS₂ sheet fabrication

All microdroplets were wrapped with monolayer molybdenum disulfide (MoS₂) grown directly onto fused silica coverslips by collaborators using metal-organic chemical vapor deposition (MOCVD)¹⁶. For each photolithography step, a layer of poly(methyl methacrylate) (PMMA) was spun onto the MoS₂ in order to help it adhere to the chip during processing.

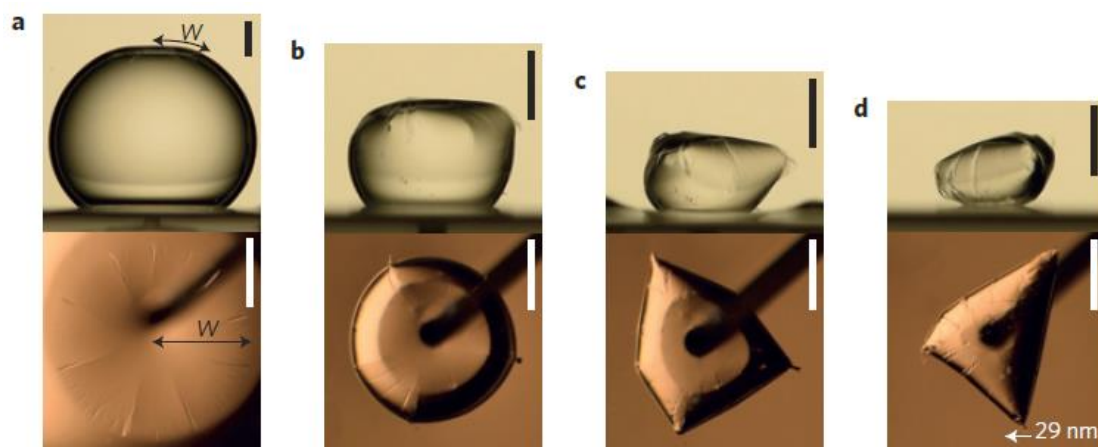


Figure 5.1: Macroscopic wrapping of liquid drop by highly-bendable sheet

Side (above) and top (below) views of a 29-nm-thick polystyrene sheet as it wraps a shrinking drop of water from beginning state (a) to ending state (d) in an environment of silicone oil. The initial shape of the droplet in (a) is mostly spherical, while the final, fully-wrapped drop is prismatic in shape. Scale bar 1 mm. Figure from Paulsen et al. (2015)³.

(In water, MoS₂ will delaminate from the fused silica if this extra layer is not used.) Standard photolithography techniques were used to pattern the MoS₂ into a variety of simple shapes on the scale of tens of microns (dark gray shapes in Fig. 5.2), and they were ultimately defined by a sulfur hexafluoride (SF₆) etch. (In the case of paneled devices, pictured in Fig. 5.2 as black shapes, we first pattern and deposit 100 nm of copper (Cu) onto the MoS₂, and then perform a second round of photolithography to etch the MoS₂ into the desired shapes.) In the final step, we soak the chips in acetone to remove the PMMA.

Right before experiments are conducted, we release the MoS₂ sheets from the chip by etching them for 20-90 s in hydrofluoric acid (HF, Sigma-Aldrich, 48% by weight in water) that has been diluted by a factor of 10:1. The HF etches the fused silica supporting the MoS₂, thereby releasing devices from the chip surface. The chip is then placed directly into a home-built cuvette (see Fig. 5.3), which is filled with deionized (DI) water. We exchange the liquid in the cuvette with DI water three times, at which point the HF concentration is low enough to safely use away from a chemical hood, as well as low enough that no significant etching of the cuvette glass occurs.

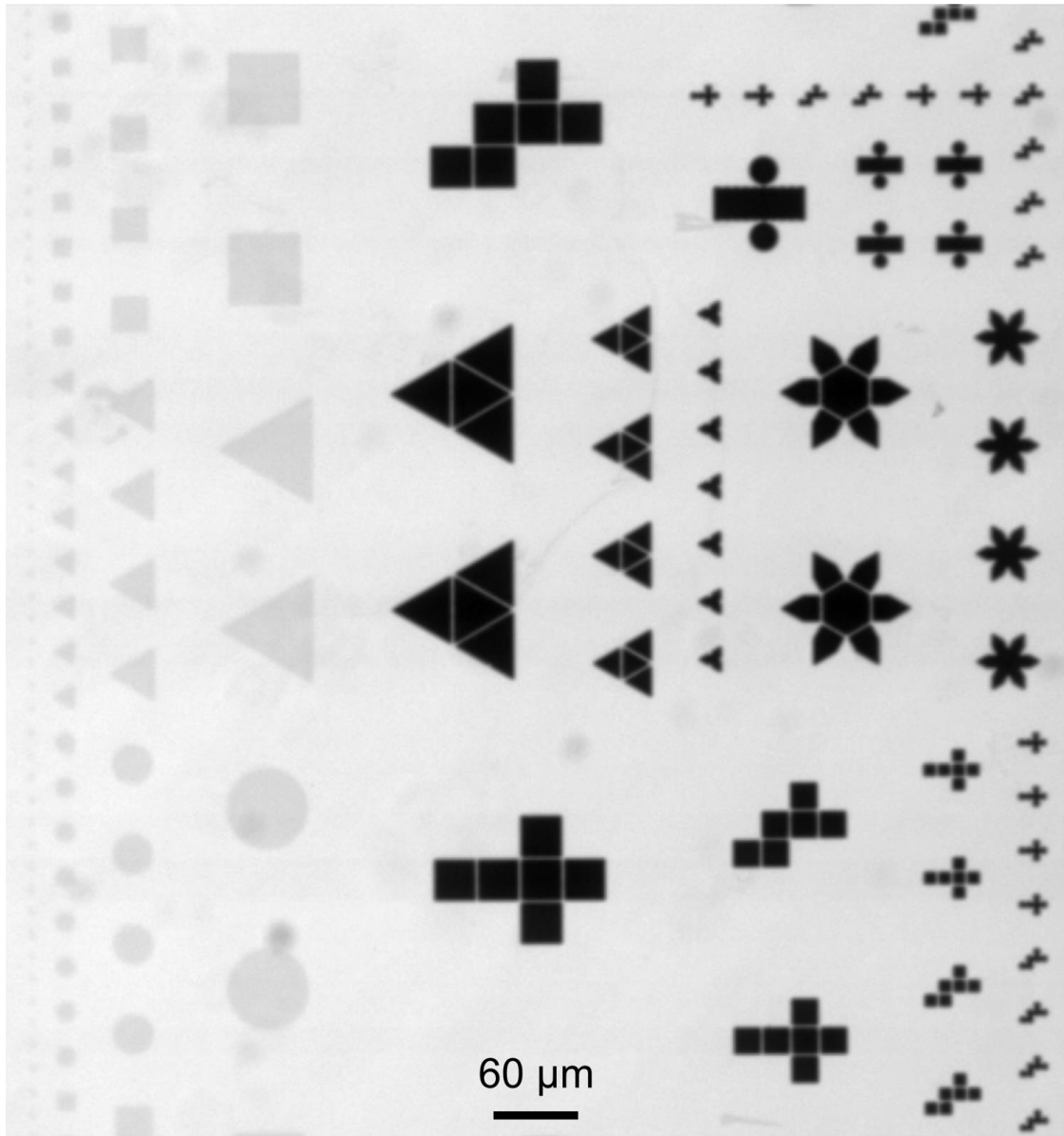


Figure 5.2: Image of initial wrapping sheet shapes

White-light transmission mode image of MoS₂ sheets prior to their release from the fused silica substrate. Dark gray shapes are bare MoS₂ while black shapes are the 100 nm of Cu deposited onto MoS₂ bases. In these paneled devices, the MoS₂ serves as a highly-bendable connecting hinge.

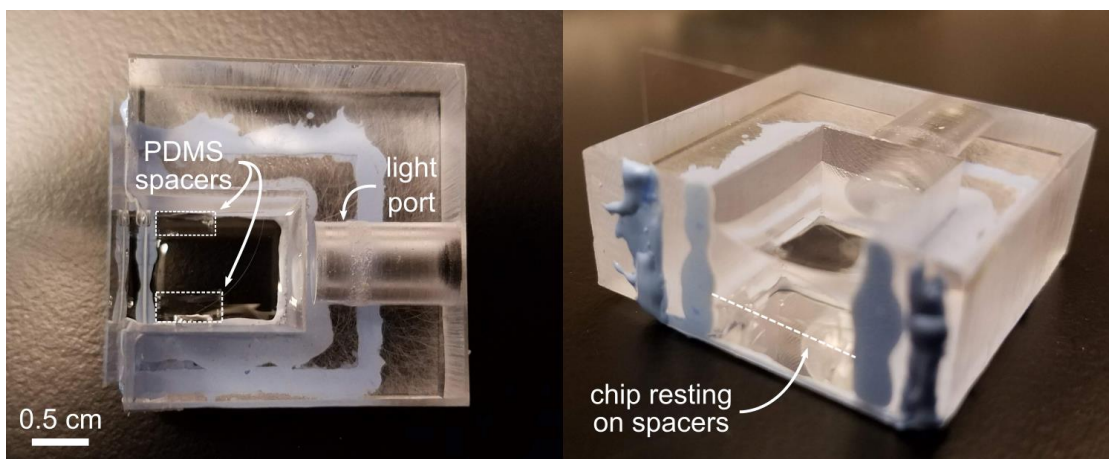


Figure 5.3: Cuvette for side and bottom co-viewing of wrapping events

Photographic views of our home-built cuvette allowing us to simultaneously view wrapping events from the side and from below. The indicated light port directs the side transmission light source; the transmission light source for the bottom view is that of the inverted microscope on which the cuvette rests. See Fig. 5.4 for a schematic of the setup.

5.3 Experiment setup

Our general approach to observing microdroplet dynamics is to work with MoS₂ sheets and oil droplets in a water bath. Any deviations from this setup are noted accordingly.

The experimental setup is shown schematically in Fig. 5.4. After conducting the liquid exchange with DI water as described in Sec. 5.3, we position the cuvette in an inverted microscope. Polydimethylsiloxane (PDMS) spacers lift the device chip up to the appropriate height for co-focusing the side and bottom view objectives. Unless otherwise noted, the chip remained in DI water throughout all experiments.

All imaging was conducted in transmission mode with white light. For the bottom view, this was accomplished with an inverted microscope lit from above. For the side view, we drilled a light port into the wall of our cuvette (see Fig. 5.3) to support a second, side-on light source, also operating in tandem with a side-on objective in transmission mode (see schematic in Fig. 5.4). For all co-focused observations, we used a 40x objective for the side view and a 10x objective for the bottom view. Both objectives had correction collars which were adjusted to account for the glass and water between the objective and the sample. We also collected data with the sole use of the inverted microscope, recording experiments from the bottom

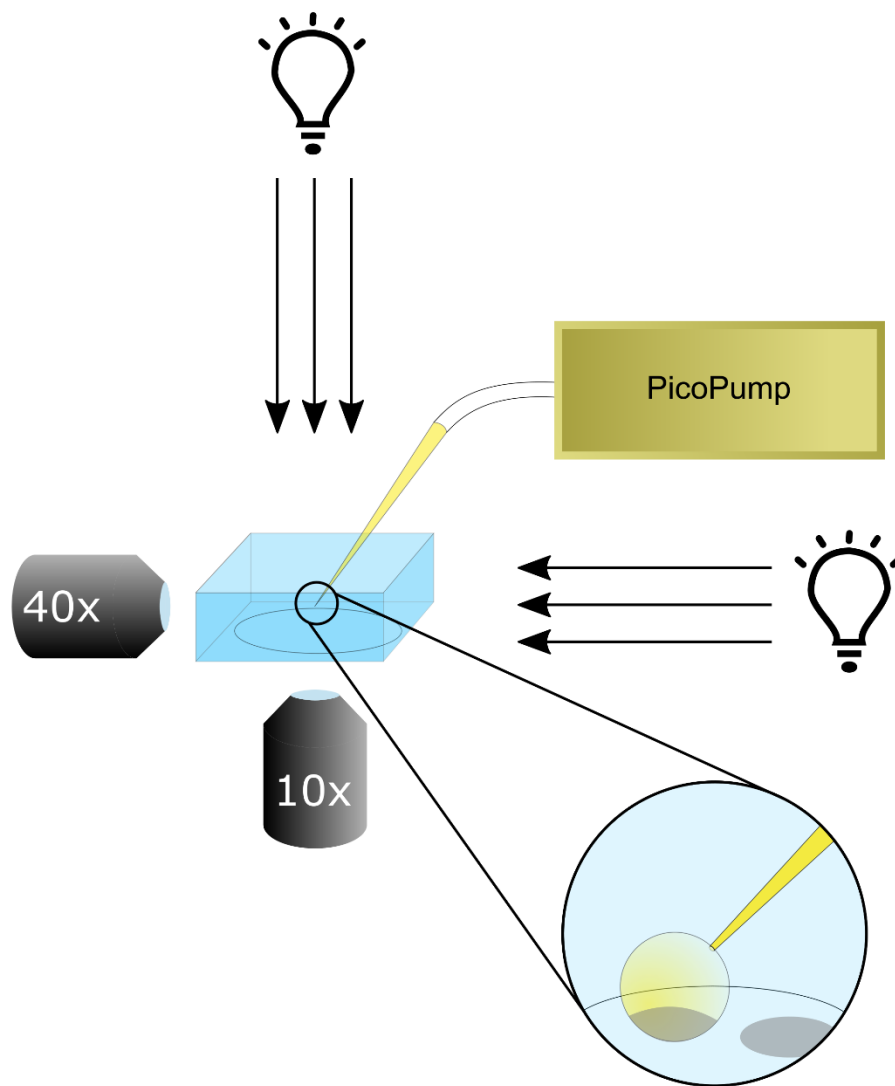


Figure 5.4: Setup for manipulating wrapped microdroplets

When viewing wrappings from both the side and bottom views, we use a 40x and a 10x objective, respectively. When only viewing wrappings from below the sample, we use a variety of objectives, depending on our specific imaging needs. Two separate white light sources illuminate the sample horizontally and vertically, as indicated by the white light bulb cartoons. As detailed in Sec. 5.4, a micropipette hooked up to a precision pump supports our droplets while we interact with the 2D materials.

view only. For these recordings, we used a variety of magnifications depending on our needs. Occasionally we did not use the cuvette, opting to place the chip in a glass-bottom petri dish filled with water on the inverted microscope platform. The captions for all white-light images state from which view they were taken.

Using an electronic micromanipulator (Sensapex), we positioned a glass micropipette (0.4-5 μm inner diameter, World Precision Instruments) under the water and over the MoS_2 devices, as shown in the exploded view in Fig. 5.4. Unless otherwise noted, the micropipette was filled with Fluorinert FC-70 (3M), an oil that is both denser than and index-matched to water. (This index-matching quality is helpful in obtaining minimally-distorted images of our wrapped microdroplets.) The interfacial energies are such that the lowest energy state involves the (released) MoS_2 sheets wrapping the surfaces of the Fluorinert microdroplets, which remain attached to the micropipette tip. (The exploded view in Fig. 5.4 shows a cartoon of this situation.)

We formed microdroplets tens of microns in diameter by applying pressure spikes (PicoPump, World Precision Instruments) to the micropipette. For appropriate ejection pressures and hold times (typically 20-45 psi and ~ 100 ms, respectively), droplets would remain attached to the

micropipette tip. This allowed us to precisely position the microdroplets above the patterned MoS₂ sheets and lower them down onto the sheets for pick-up. By using a combination of adjustments to the background holding pressure and the use of a vacuum pump, we could controllably shrink the droplets while recording the ensuing wrapping process.

5.4 Wrapping microdroplets with monolayer MoS₂

In Fig. 5.5 we present a time lapse of the wrapping of a Fluorinert microdroplet by a circular MoS₂ sheet showing both side and bottom views of the process. To accomplish this, we bring the droplet into contact with a given shape and then drag and lift it off of the surface. At this point the shape is wrapping the Fluorinert droplet surface, as can be most clearly seen in lower-left (bottom-view) panel of Fig. 5.5. By decreasing the size of the droplet, we can image the dynamics of the wrapping process as the sheet-radius-to-droplet-radius (W/R) ratio increases.

We first notice that as with the initial macroscopic wrapping depicted in Fig. 5.1(a), there is an initial flattening of the surface of our spherical droplet in contact with the MoS₂ sheet. This is most clearly seen in the upper-left (side-view) panel presented in Fig. 5.5. Likewise, as with the macroscopic end state presented in Fig. 5.1(d), we observe that our

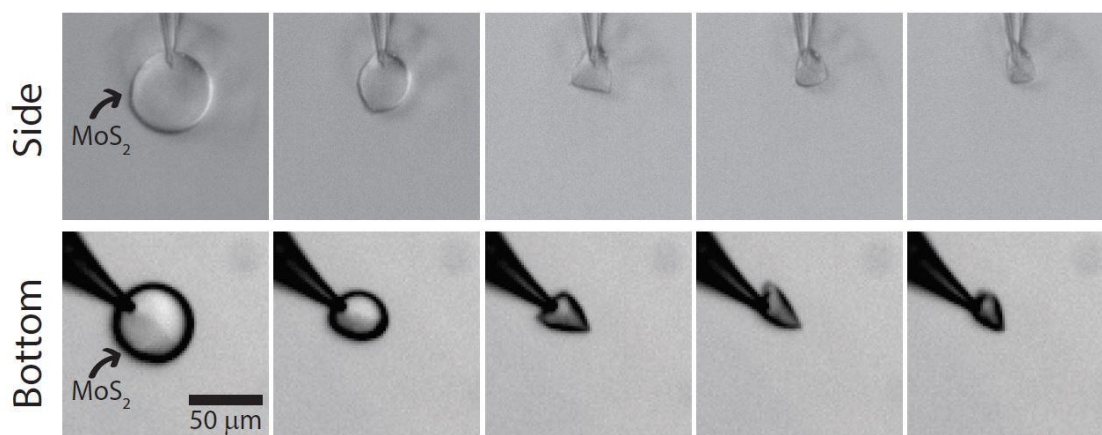


Figure 5.5: Time lapse of a wrapping event

Left-to-right time lapse of a wrapping event from both simultaneous side and bottom views. The initial MoS₂ sheet is circular in shape, and can be most clearly seen as the dark gray shape in the leftmost bottom view. In the leftmost side view, we know the location of the MoS₂ sheet both from the orientation of our setup and the slight deformation of the droplet from a perfect sphere most easily seen in the side view. There are artifacts in the side view images due to imperfect background subtraction, but the droplet is clearly seen in focus in all images.

microdroplet deforms into a fully-wrapped prismatic shape.

We further extend our experiments by picking up square and triangular sheets with the Fluorinert microdroplets. (The experiments of Paulsen et al. (2015)³ from which Fig. 5.1 is taken used only circular sheets.) After picking up tens of sheets spanning the range of circles, squares, and triangles, we have noticed that the final wrapped states tend towards specific prismatic shapes, as shown in Fig. 5.6. Both circular and triangular sheets wrap droplets into shapes resembling triangular prisms. (In addition to Fig. 5.6, see the final wrapped state of the circular sheet in Fig. 5.5.) In contrast, square sheets tend to wrap droplets into square packets with a corners-to-center fold. The non-spherical, defined-edge nature of these shapes agrees with the findings of Paulsen *et al.* (2015)³.

In order to better characterize the wrapping process, we calculate the Hausdorff distance, a measure of the degree to which two superimposed objects resemble one another¹⁷, for several droplet transformations. In the case of this experiment, the two objects are the perimeter of the projected area of the wrapping and a perfect circle of the same (effective) radius (a circle being the projected area of a sphere). This means that the Hausdorff distance increases as the wrapping becomes less and less spherical – or, in the context of our calculation, circular – in nature.

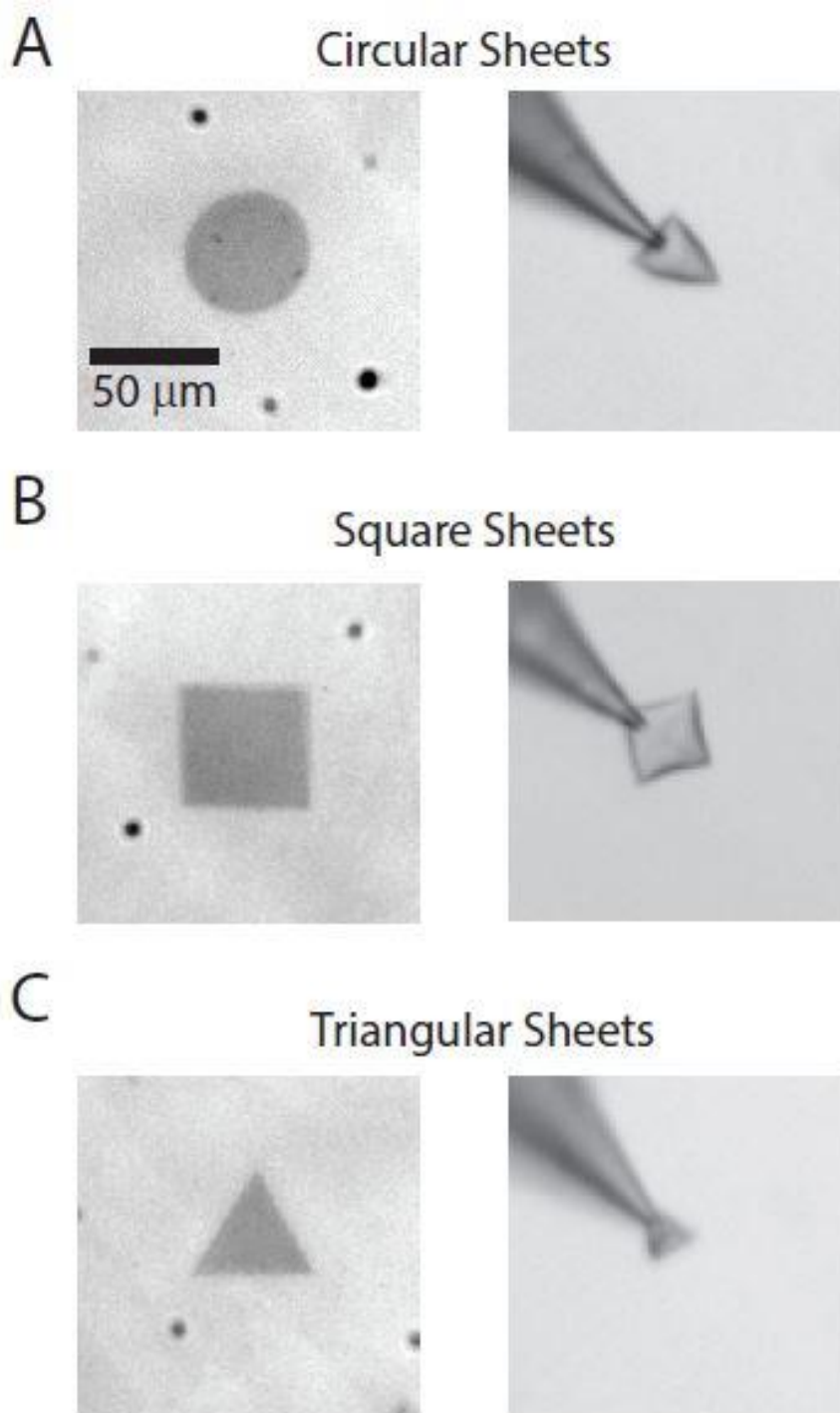


Figure 5.6: A variety of microdroplet wrappings

A catalog of the microdroplet wrappings resulting from (a) circular, (b) square, and (c) triangular planar sheets of monolayer MoS₂. In general the circular and triangular sheets result in roughly triangular prismatic wrappings, while square sheets tend to wrap into rectangular prisms.

The average Hausdorff distance d_H between two sets of points A and B is defined as

$$d_H(A, B) = \frac{1}{2} (h(A, B) + h(B, A)) \quad (5.2)$$

where the function h is defined as

$$h(A, B) = \max_{a \in A} \left\{ \min_{b \in B} \{d(a, b)\} \right\} \quad (5.3)$$

in which a and b are points in the set A and B , respectively, and the function d gives the distance between points a and b . More intuitively stated: for each point in set A , find the distance to the nearest point in set B (or vice versa); the Hausdorff distance h is then the maximum out of all of those distances.

In Fig. 5.7 we present a graph of d_H plotted against W_{eff}/R_{eff} , the ratio of the effective radius of the wrapping sheet to the effective radius of the fitted circle. Note that we have normalized d_H by the effective radius of the sheet, W_{eff} , and that the ratio W_{eff}/R_{eff} increases in time. The plot thus additionally represents the time evolution of d_H . Note also that we specify the *effective* radii for two reasons: (1) the true perimeter of the wrapping becomes less and less circular as the wrapping progresses; (2) the initial sheet shapes can be non-circular. In practice, we use an ImageJ script

Microencapsulation of Fluorinert with MoS₂

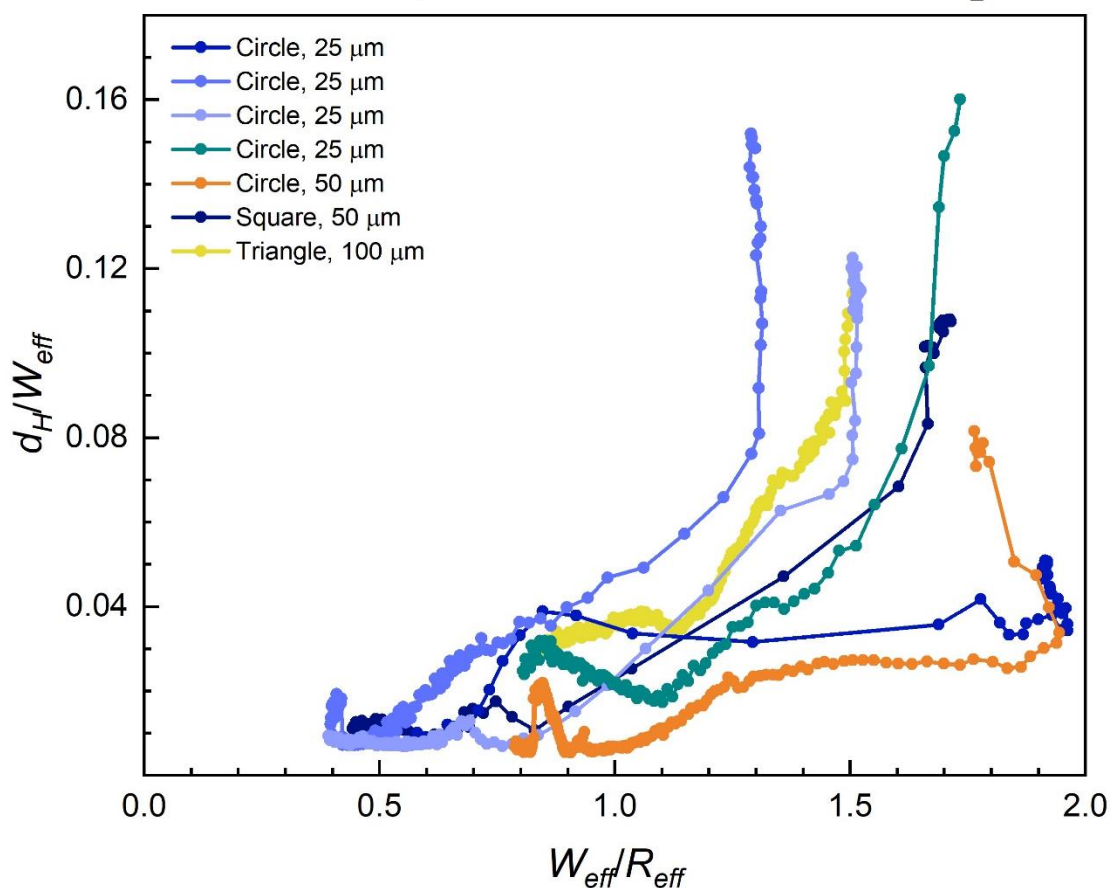


Figure 5.7: Hausdorff distance as a function of radius ratio

Hausdorff distance d_H normalized by the wrapping sheet effective radius W_{eff} plotted as a function of the ratio W_{eff}/R_{eff} , where R_{eff} is the effective radius of the shrinking droplet, for a variety of shapes and sizes of MoS₂ sheets. The legend records the diameter of the circular sheets and the edge length of the square and triangular sheets. All data on this graph is for MoS₂ sheets wrapping Fluorinert microdroplets in DI water. Time increases with W_{eff}/R_{eff} .

to find W_{eff} by calculating $W_{eff} = \sqrt{A/\pi}$, where A is the area of the wrapping shape. We fit the projected droplet area to recover R_{eff} and conduct the calculation of d_H in MATLAB.

Paulsen *et al.* (2015)³ also calculate d_H for their macroscopic wrappings, and they find that a folding pattern is clearly established by the time $W_{eff}/R_{eff} = 1.3$. From our data we agree that the onset of a folding pattern exists for $W_{eff}/R_{eff} \leq 1.3$, as some curves begin to increase in slope well before the ratio value of 1.3. Two curves in particular, one for a square sheet, and one for a circular sheet, noticeably vary from the rest of the data. We find that the backtracking of the data for the square sheet (Fig. 5.7, orange), upon examining the corresponding video, is due to a change in shape orientation. In examining the video for the 25 μm circle graphed in medium blue in Fig. 5.7, we find that the viewing angle captures a roughly circular projected droplet area until quite late in the wrapping process. In general, further work exploring a greater number of sheet shapes and sizes is required to refine our understanding of the onset of folding in the wrapping of a shrinking microdroplet.

5.5 Conclusions and research outlook

The procedures developed above are not restricted to the use of

Fluorinert as the microdroplet, DI water as the surrounding medium, and MoS₂ as the wrapping material of interest. Any fluid immiscible in water could be used (though we note that many oils, unlike Fluorinert, are less dense than water, and their use may pose additional experimental challenges), and it would be interesting to use other 2D materials, such as graphene, as the wrapping sheet. The droplet and medium could also be exchanged such that water microdroplets are formed in an oil bath. This configuration would allow us to use extremely thin atomic layer deposition (ALD) oxides¹⁸ as the wrapping sheets, materials that would preferentially wrap the water microdroplets, in contrast to our MoS₂ sheets preferentially wrapping oil. Another interesting possibility is to use phase change materials (PCMs) for the microdroplets¹⁹. In this case we imagine forming a liquid droplet of PCM, wrapping it with a 2D material, and pushing it through its phase change into its solid state. This would allow for the exploration of “freezing” the microencapsulated drop, a potentially useful microencapsulation application. Similarly, it would be fun to experiment with the magnetic control of microencapsulated ferrofluids²⁰.

This demonstration indicates a new route for making 3D microgeometries out of 2D materials by drawing on an existing literature of droplet wrapping. Moreover, future work can take advantage of the rich

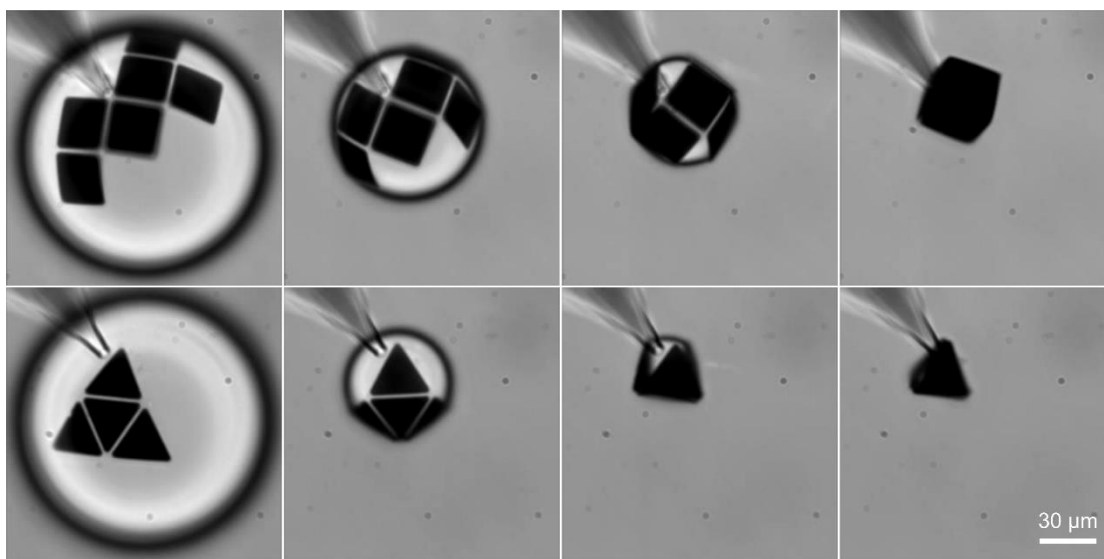


Figure 5.8: Folding via wrapping

Time sequence of (above) cubic and (below) triangular Cu-paneled devices with MoS₂ hinges folding into 3D shapes as they wrap a shrinking microdroplet.

literature exploring capillary origami, which could suggest new patterns with which to shape droplets. We have already begun exploring this world by using paneled shapes, as described in Sec. 5.3. As a closing visual, Fig. 5.8 showcases prisms folded via wrapping the surface of a shrinking droplet with panels of Cu linked by hinges of MoS₂.

References

1. Blees, M. K. Graphene as atomic paper: From bending stiffness to mechanical metamaterials. (Cornell University, 2015).
2. Blees, M. K. *et al.* Graphene kirigami. *Nature* **524**, 204–207 (2015).
3. Paulsen, J. D. *et al.* Optimal wrapping of liquid droplets with ultrathin sheets. *Nat. Mater.* **14**, 1206–1209 (2015).
4. Kumar, D., Paulsen, J. D., Russell, T. P. & Menon, N. Wrapping with a splash: High-speed encapsulation with ultrathin sheets. *Science* **359**, 775 (2018).
5. Huang, J. *et al.* Capillary wrinkling of floating thin polymer films. *Science* **317**, 650–653 (2007).
6. King, H., Schroll, R. D., Davidovitch, B. & Menon, N. Elastic sheet on a liquid drop reveals wrinkling and crumpling as distinct symmetry-breaking instabilities. *Proc. Natl. Acad. Sci.* **109**, 9716–9720 (2012).
7. Bae, J., Ouchi, T. & Hayward, R. C. Measuring the Elastic Modulus of Thin Polymer Sheets by Elastocapillary Bending. *ACS Appl. Mater. Interfaces* **7**, 14734–14742 (2015).

8. Boncheva, M., Bruzewicz, D. A. & Whitesides, G. M. Millimeter-scale self-assembly and its applications. *Pure Appl. Chem.* **75**, 621–630 (2003).
9. Py, C. *et al.* Capillary origami: spontaneous wrapping of a droplet with an elastic sheet. *Phys. Rev. Lett.* **98**, 156103 (2007).
10. Piñeirua, M., Bico, J. & Roman, B. Capillary origami controlled by an electric field. *Soft Matter* **6**, 4491 (2010).
11. McHale, G., Newton, M. I., Shirtcliffe, N. J. & Geraldi, N. R. Capillary origami: superhydrophobic ribbon surfaces and liquid marbles. *Beilstein J. Nanotechnol.* **2**, 145–151 (2011).
12. Geraldi, N. R., Ouali, F. F., Morris, R. H., McHale, G. & Newton, M. I. Capillary origami and superhydrophobic membrane surfaces. *Appl. Phys. Lett.* **102**, 214104 (2013).
13. Landau, L. D. & Lifshitz, E. M. *Theory of Elasticity.* **7**, 38-86 (Elsevier, 1986).
14. Jiang, J.-W., Qi, Z., Park, H. S. & Rabczuk, T. Elastic bending modulus of single-layer molybdenum disulfide (MoS₂): finite thickness effect. *Nanotechnology* **24**, 435705 (2013).
15. Andrew, R. C., Mapasha, R. E., Ukpong, A. M. & Chetty, N. Mechanical properties of graphene and boronitrene. *Phys. Rev. B* **85**, 125428 (2012).
16. Kang, K. *et al.* High-mobility three-atom-thick semiconducting films with wafer-scale homogeneity. *Nature* **520**, 656–660 (2015).
17. Huttenlocher, D. P., Klanderma, G. A. & Rucklidge, W. J. Comparing images using the Hausdorff distance. *IEEE Trans. Pattern Anal. Mach. Intell.* **15**, 850–863 (1993).

18. Davami, K. *et al.* Ultralight shape-recovering plate mechanical metamaterials. *Nat. Commun.* **6**, 10019 (2015).
19. Zhao, C. Y. & Zhang, G. H. Review on microencapsulated phase change materials (MEPCMs): Fabrication, characterization and applications. *Renew. Sustain. Energy Rev.* **15**, 3813–3832 (2011).
20. Raj, K., Moskowitz, B. & Casciari, R. Advances in ferrofluid technology. *J. Magn. Magn. Mater.* **149**, 174–180 (1995).

CHAPTER 6

OUTLOOK FOR TWO-DIMENSIONAL MATERIALS RESEARCH

In this dissertation we have explored a wide-ranging set of two-dimensional (2D) materials physics. While each chapter closes with an outlook of the field related to the content of that chapter, we will conclude here with a brief statement of the prospects of 2D materials research that the author finds most interesting and exciting.

First, in the world of “valleytronics”, valley-based detection of the valley index would be fascinating. To clarify, as stated in Ch. 3, we used the *charge* degree of freedom to infer the presence of the *valley* Hall effect. Modern electronics are highly developed for detecting and manipulating charges by using devices based on the charge degree of freedom. Likewise we have magnetic means of detecting electron spin. To fully realize “valleytronics” as a field, *valley*-based devices for detecting and manipulating the valley index should exist. One level above this goal is the combination of electronics, spintronics, and valleytronics into a grand system for studying materials in which all three degrees of freedom are active as long-lived information carriers.

Second, in the world of wrapping, the possibilities presented by microencapsulation for applications such as targeted drug delivery, oil spill

cleanup, and foldable devices with bistable physical states are particularly exciting. As micro-robotics makes research headway, the ability to encase materials without added bulk from the wrapper will be especially useful. Likewise, rigid microdevices, formed, for example, from panels such as those presented at the end of Ch. 5, that could selectively morph between two physical states may prove useful in micro-robotic actuation.

Much exciting progress has been made in 2D materials research since the isolation of atomic crystals in 2005¹. While this dissertation covers a very small segment of the 2D materials field, the author hopes that it leaves you with a sense of the breadth of the physics and applications accessible with atomically thin crystals.

References

1. Novoselov, K. S. *et al.* Two-dimensional atomic crystals. *Proc. Natl. Acad. Sci. U. S. A.* **102**, 10451–10453 (2005).

APPENDIX A

DERIVATION OF THE BERRY CURVATURE

A succinct understanding of the intrinsic contribution to the anomalous Hall effect (AHE) was presented by Sir Michael Berry in his 1984 paper on a quantum phase factor now known as the Berry phase. We will examine this Berry phase along with its associated quantity the Berry curvature in this appendix by following the presentation of Marder (2010)¹.

The Berry phase is a geometric phase that arises naturally in the wavefunctions of a quantum mechanical system that has been projected adiabatically forward in time. We begin by considering a Hamiltonian dependent on time through some parameters $\boldsymbol{\lambda}(t)$. Thus, $\hat{H} = \hat{H}(\boldsymbol{\lambda}(t))$, and we have an eigenvalue problem of

$$\hat{H}(\boldsymbol{\lambda}(t))|n(\boldsymbol{\lambda}(t))\rangle = \varepsilon_n(\boldsymbol{\lambda}(t))|n(\boldsymbol{\lambda}(t))\rangle$$

where eigenkets $|n\rangle$ have eigenenergies ε_n . We therefore expect general solutions $|\psi_n(t)\rangle$ of the time-dependent Schrödinger equation (TDSE) to have the form

$$|\psi_n(t)\rangle = e^{i\theta_n(t)} e^{i\gamma_n(t)} |n(\boldsymbol{\lambda}(t))\rangle \quad (\text{A.1})$$

where

$$\theta_n(t) = -\frac{1}{\hbar} \int_0^t \varepsilon_n(\boldsymbol{\lambda}(t')) dt'$$

is known as the dynamical phase (in the case of a time-independent eigenenergy, θ_n is the usual $-\varepsilon_n t/\hbar$), and $\gamma_n(t)$ is the geometric, or Berry, phase. If we plug the general wavefunctions of Eq. A.1 into the TDSE, we find

$$i\hbar \frac{\partial}{\partial t} |\psi_n(t)\rangle = \hat{H}(\boldsymbol{\lambda}(t)) |\psi_n(t)\rangle$$

$$\left(\varepsilon_n(\boldsymbol{\lambda}(t)) - \hbar \frac{\partial \gamma_n}{\partial t} + i\hbar \frac{\partial}{\partial t} \right) |n(\boldsymbol{\lambda}(t))\rangle = \varepsilon_n(\boldsymbol{\lambda}(t)) |n(\boldsymbol{\lambda}(t))\rangle$$

$$\langle n(\boldsymbol{\lambda}(t)) | \frac{\partial \gamma_n}{\partial t} | n(\boldsymbol{\lambda}(t)) \rangle = \langle n(\boldsymbol{\lambda}(t)) | i \frac{\partial}{\partial t} | n(\boldsymbol{\lambda}(t)) \rangle$$

$$\frac{\partial \gamma_n}{\partial t} = i \langle n(\boldsymbol{\lambda}(t)) | \frac{\partial}{\partial t} | n(\boldsymbol{\lambda}(t)) \rangle$$

Finally, using the chain rule, we write

$$\frac{\partial \gamma_n}{\partial t} = i \langle n(\boldsymbol{\lambda}(t)) | \nabla_{\boldsymbol{\lambda}} | n(\boldsymbol{\lambda}(t)) \rangle \cdot \frac{\partial \boldsymbol{\lambda}}{\partial t}$$

or

$$\gamma_n = i \int_{\boldsymbol{\lambda}(0)}^{\boldsymbol{\lambda}(t_f)} d\boldsymbol{\lambda} \cdot \langle n(\boldsymbol{\lambda}) | \nabla_{\boldsymbol{\lambda}} | n(\boldsymbol{\lambda}) \rangle \quad (\text{A.2})$$

In Eq. A.2 we now have a general definition of the Berry phase γ_n .

Notice that it is evaluated as a path integral in the $\boldsymbol{\lambda}$ parameter space; as long as the path is traced adiabatically in this parameter-space, γ_n only depends

on the starting and ending points. Furthermore, γ_n is a function of the eigenkets $|n(\boldsymbol{\lambda})\rangle$ of the system. Since γ_n arises from the underlying $\boldsymbol{\lambda}$ -geometry of the system, it was historically referred to as the geometric phase.

Typically, γ_n is expressed as

$$\gamma_n = \int_C d\boldsymbol{\lambda} \cdot \mathbf{A}_n(\boldsymbol{\lambda}) \quad (\text{A.3})$$

where

$$\mathbf{A}_n(\boldsymbol{\lambda}) = i\langle n(\boldsymbol{\lambda}) | \nabla_{\boldsymbol{\lambda}} | n(\boldsymbol{\lambda}) \rangle \quad (\text{A.4})$$

is referred to as the Berry connection and functions as a vector potential. As in classical electrodynamics, this vector potential is gauge-dependent: taking $|n(\boldsymbol{\lambda})\rangle \rightarrow e^{i\zeta(\boldsymbol{\lambda})} |n(\boldsymbol{\lambda})\rangle$ results in $\mathbf{A}_n(\boldsymbol{\lambda}) \rightarrow \mathbf{A}_n(\boldsymbol{\lambda}) - \nabla_{\boldsymbol{\lambda}}\zeta(\boldsymbol{\lambda})$. For this gauge γ_n will accumulate an additional quantity $\zeta(\boldsymbol{\lambda}(0)) - \zeta(\boldsymbol{\lambda}(t_f))$ while traveling the path C , but this quantity can generally be removed with a suitable gauge choice. Historically, then, this geometric phase was considered unimportant.

In 1984, Berry realized that γ_n cannot be ignored if the path C is a closed path in parameter space such that $\boldsymbol{\lambda}(t_f) = \boldsymbol{\lambda}(0)$. In this case γ_n will change under the above gauge transformation by $2\pi j$, where j is an integer. That is, effects based on γ_n cannot be ignored for systems traveling

adiabatically in closed loops around the $\boldsymbol{\lambda}$ parameter space.

Taking the analogy with electrodynamics a step further, we can define an effective magnetic field within the $\boldsymbol{\lambda}$ parameter space, called the Berry curvature $\boldsymbol{\Omega}_n(\boldsymbol{\lambda})$:

$$\boldsymbol{\Omega}_n(\boldsymbol{\lambda}) = \nabla_{\boldsymbol{\lambda}} \times \mathbf{A}_n(\boldsymbol{\lambda})$$

Using Stokes' Theorem we can thus define the Berry phase as

$$\gamma_n = \int_S d\mathbf{S} \cdot \boldsymbol{\Omega}_n(\boldsymbol{\lambda})$$

where S is an arbitrary surface in $\boldsymbol{\lambda}$ -space enclosed by the loop C .

Viewed in this formulation, the Berry curvature can be taken as the more fundamental quantity. This concept was explored more broadly by Kuratsuji and Iida in 1985, who showed that the Berry curvature directly participates in the dynamics of the $\boldsymbol{\lambda}$ parameters².

References

1. Marder, M. P. *Condensed Matter Physics*. (John Wiley & Sons, Inc., 2010).
2. Kuratsuji, H. & Iida, S. Effective Action for Adiabatic Process: Dynamical Meaning of Berry and Simon's Phase. *Progress of Theoretical Physics* **74**, 439–445 (1985).

APPENDIX B

DERIVATION OF THE INTRINSIC ANOMALOUS HALL EFFECT IN CRYSTALLINE SOLIDS

Here we outline the semiclassical approach to deriving the intrinsic contribution to the AHE. This method is based on wave packet dynamics and follows the presentation of Nagaosa *et al.*, (2010)¹.

First, we note that in a perfect crystal, wave packets maintain their integrity over long time periods and behave in many respects like classical particles. We thus substitute the study of Bloch electron dynamics with that of wave packet dynamics, defining our wave packet $|\Psi_{n,\mathbf{k}_c,\mathbf{r}_c}(\mathbf{r}, t)\rangle$, centered at position \mathbf{r}_c and with average momentum $\hbar\mathbf{k}_c$, as

$$|\Psi_{n,\mathbf{k}_c,\mathbf{r}_c}(\mathbf{r}, t)\rangle = \frac{1}{\sqrt{V}} \sum_{\mathbf{k}} w_{\mathbf{k}_c,\mathbf{r}_c}(\mathbf{k}) e^{i\mathbf{k}\cdot(\mathbf{r}-\mathbf{r}_c)} |u_{n,\mathbf{k}}(\mathbf{r})\rangle \quad (\text{B.1})$$

where Sundaram and Niu (1999)^{2,3} have shown that

$$w_{\mathbf{k}_c,\mathbf{r}_c}(\mathbf{k}) = |w_{\mathbf{k}_c,\mathbf{r}_c}(\mathbf{k})| e^{i(\mathbf{k}-\mathbf{k}_c)\cdot\mathbf{A}_n(\mathbf{k})} \quad (\text{B.2})$$

with $\mathbf{A}_n(\mathbf{k})$ the Berry connection defined in Eq. 2.2 of Sec. 2.3. Note that the time-dependence of $|\Psi_{n,\mathbf{k}_c,\mathbf{r}_c}(\mathbf{r}, t)\rangle$ is implicitly contained in \mathbf{k}_c and \mathbf{r}_c . Perturbing our system with a weak electric field defined by the potential $\varphi(\mathbf{r})$, we can generate the wave packet dynamics by constructing a

semiclassical Lagrangian from the wavefunctions defined in Eq. B.1:

$$\mathcal{L} = \left\langle \Psi_{n,\mathbf{k}_c,r_c}(\mathbf{r}, t) \left| i\hbar \frac{d}{dt} - \hat{H} \right| \Psi_{n,\mathbf{k}_c,r_c}(\mathbf{r}, t) \right\rangle \quad (\text{B.3})$$

where

$$\hat{H} = \frac{\hat{\mathbf{p}}^2}{2m} + V(\mathbf{r}) - e\varphi(\mathbf{r}) \quad (\text{B.4})$$

Keeping in mind the implicit time dependence found in \mathbf{k}_c and \mathbf{r}_c , Eq. B.3

can be written as

$$\mathcal{L} = \hbar \mathbf{k}_c \dot{\mathbf{r}}_c + \hbar \dot{\mathbf{k}}_c \cdot \mathbf{A}_n(\mathbf{k}_c) - \varepsilon_n(\mathbf{k}_c, \mathbf{r}_c) + e\varphi(\mathbf{r}_c) \quad (\text{B.5})$$

The first two terms in Eq. B.5 arise from the time-dependent term in Eq.

B.3, while the last two terms arise from the Hamiltonian. In particular, note

that the Berry connection arises naturally in this semiclassical approach.

Applying the Euler-Lagrange equations to Eq. B.5, we find that

$$\dot{\mathbf{r}}_c = \frac{\partial \varepsilon_n(\mathbf{k}_c)}{\hbar \partial \mathbf{k}_c} - \hbar \dot{\mathbf{k}}_c \times \boldsymbol{\Omega}_n(\mathbf{k}) \quad (\text{B.6})$$

$$\dot{\mathbf{k}}_c = -\frac{e}{\hbar} \mathbf{E}$$

Taking the velocity of the wave packet defined in Eq. B.6 as the velocity of

our Bloch electrons, we find that

$$\mathbf{v}_n(\mathbf{k}) = \frac{\partial \varepsilon_n(\mathbf{k})}{\hbar \partial \mathbf{k}} + \frac{e}{\hbar} \mathbf{E} \times \boldsymbol{\Omega}_n(\mathbf{k}) \quad (\text{B.7})$$

The second term in Eq. B.7, dependent on the Berry curvature $\boldsymbol{\Omega}_n(\mathbf{k})$

(defined in Eq. 2.3), is always transverse to the applied electric field \mathbf{E} and will give rise to a Hall current in materials for which $\mathbf{\Omega}_n(\mathbf{k})$ is nonzero.

References

1. Nagaosa, N., Sinova, J., Onoda, S., MacDonald, A. H. & Ong, N. P. Anomalous Hall effect. *Rev. Mod. Phys.* **82**, 1539–1592 (2010).
2. Sundaram, G. & Niu, Q. Wave-packet dynamics in slowly perturbed crystals: Gradient corrections and Berry-phase effects. *Phys. Rev. B* **59**, 14915 (1999).
3. Marder, M. P. *Condensed Matter Physics*. (John Wiley & Sons, Inc., 2010).

APPENDIX C

DERIVATION OF THE VALLEY HALL CONDUCTIVITY IN MONOLAYER MOLYBDENUM DISULFIDE

As described in Sec. 2.3, the valley Hall conductivity σ_H^v in monolayer MoS₂ is composed of three components:

$$\sigma_H^v = \sigma_H^{in} + \sigma_H^{sk} + \sigma_H^{sj} \quad (2.4)$$

where σ_H^{in} is the intrinsic contribution, σ_H^{sk} the skew scattering contribution, and σ_H^{sj} the side-jump contribution. The skew scattering contribution is inversely proportional to the impurity concentration in the sample¹. After device fabrication, our MoS₂ is far from pristine, and we assume σ_H^{sk} is thus negligible. It is experimentally challenging to separate the side jump contribution from the intrinsic contribution as the side jump contribution only diminishes at very low carrier densities². In our experiment, which will involve relatively high carrier densities, we expect both σ_H^{in} and σ_H^{sj} to be important components of σ_H^v . According to Nagaosa *et al.* (2010)¹, and based on the work of Sinitsyn *et al.* (2007)³, $\sigma_H^{sj} = -2\sigma_H^{in}$ in band structures where the Berry curvature is constant, as is the case in our experiment. This means that $\sigma_H^v = -\sigma_H^{in}$, and we that we can proceed with only the derivation of the intrinsic contribution to σ_H^v .

We begin our derivation by inspecting the Hamiltonian for monolayer MoS₂, ignoring spin-orbit coupling⁴:

$$\hat{H} = at(\tau_z k_x \hat{\sigma}_x + k_y \hat{\sigma}_y) + \frac{E_g}{2} \hat{\sigma}_z$$

Here, a is the lattice constant of MoS₂, t is the hopping integral for electrons hopping between nearest molybdenum neighbors (see Fig. 3.1 in Sec. 3.2), and E_g is the (direct) band gap. The wavevector \mathbf{k} is measured from the conduction band minimum of the K(K') valley, and τ_z is the valley index, with $\tau_z = 1(-1)$ for the K(K') valley. The energy eigenvalues are

$$\varepsilon_{\pm}(\mathbf{k}) = \pm \sqrt{\left(\frac{E_g}{2}\right)^2 + a^2 t^2 k^2} \quad (\text{C.1})$$

for both the K and the K' valleys. The Berry curvature in the conduction band is⁴

$$\begin{aligned} \boldsymbol{\Omega}_c(\mathbf{k}) &= -\tau_z \frac{2a^2 t^2 E_g}{(E_g^2 + 4a^2 t^2 k^2)^{3/2}} \hat{\mathbf{z}} \\ \boldsymbol{\Omega}_c(\varepsilon(\mathbf{k})) &= -\tau_z \frac{a^2 t^2 E_g}{4\varepsilon(\mathbf{k})^3} \hat{\mathbf{z}} \end{aligned} \quad (\text{C.2})$$

For the valence band, $\boldsymbol{\Omega}_v(\mathbf{k}) = -\boldsymbol{\Omega}_c(\mathbf{k})$.

We calculate the intrinsic part of the valley Hall conductivity in the conduction band of the K valley as²

$$\sigma_{c,K}^{in}(\varepsilon_F) = -\frac{e^2}{h} \int_K \frac{d\mathbf{k}}{2\pi} f(\varepsilon(\mathbf{k})) \Omega_{c,K}(\mathbf{k})$$

where $f(\varepsilon(\mathbf{k}))$ is the Fermi-Dirac distribution function, and the integral is over the first Brillouin zone. Recalling that $d\mathbf{k} = kdkd\varphi$, we integrate over φ space to find:

$$\sigma_{c,K}^{in}(\varepsilon_F) = -\frac{e^2}{h} \int_0^{k_F} kdk f(\varepsilon(k)) \Omega_{c,K}(k) \quad (\text{C.3})$$

(Note that because the conduction band is symmetric in k -space about the K -point, we can take $\mathbf{k} \rightarrow k$ without loss of generality.) In order to write our valley Hall conductivity as an integral over energies, we examine our dispersion relation from Eq. C.1:

$$\varepsilon^2(k) = \left(\frac{E_g}{2}\right)^2 + a^2 t^2 k^2$$

$$2\varepsilon d\varepsilon = 2a^2 t^2 kdk$$

$$kdk = \frac{\varepsilon d\varepsilon}{a^2 t^2}$$

Noting that we are only filling states up to the Fermi level ε_F , we plug our result back into Eq. C.3 to convert our k -space integral into an ε -space integral. We also plug in Eq. 2.5 for the Berry curvature so that we can write our conductivity as

$$\sigma_{c,K}^{in}(\varepsilon_F) = \frac{e^2 E_g}{h} \frac{1}{4} \int_{E_g/2}^{\varepsilon_F} \frac{f(\varepsilon) d\varepsilon}{\varepsilon^2}$$

where $\varepsilon_F = E_g/2 + \delta\varepsilon$ because we are just barely photoexciting carriers across the band gap. At the Fermi energy, $f(\varepsilon_F) = 1/2$, and since we are integrating within the vicinity of ε_F , we can safely pull the Fermi-Dirac distribution function out of the integral as a constant. Thus, we have

$$\begin{aligned} \sigma_{c,K}^{in}(\varepsilon_F) &\approx \frac{e^2 E_g}{h} \frac{1}{4} \left(-\frac{1}{\varepsilon} \Big|_{E_g/2}^{\varepsilon_F} \right) \\ &= \frac{e^2}{4h} \left(2 - \frac{E_g}{\varepsilon_F} \right) \end{aligned} \quad (\text{C.4})$$

Since we are photoexciting our carriers, $\sigma_{c,K}^{in}(\varepsilon_F)$ is, most precisely, the photoinduced anomalous Hall conductivity. We treat the valley-selective photoexcitation as a small Fermi-level shift $\delta\varepsilon$ in that valley (because we are only just barely exciting carriers into the conduction band in our experiment), noting that valley carrier lifetimes are much greater than their recombination time⁵. We write the resulting change in the intrinsic conductivity as

$$\delta\sigma_c^{in} = \sigma_c^K(\varepsilon_F + \delta\varepsilon) + \sigma_c^{K'}(\varepsilon_F) \quad (\text{C.5})$$

Noting that $\sigma_c^{K'} = -\sigma_c^K$, we see that $\delta\sigma_c^{in}$ vanishes when $\delta\varepsilon = 0$, and is non-zero when $\delta\varepsilon \neq 0$. Plugging Eq. C.4 into Eq. C.5, we find

$$\begin{aligned}
\delta\sigma_c^{in} &= \frac{e^2}{4h} \left(2 - \frac{E_g}{\varepsilon_F + \delta\varepsilon} \right) - \frac{e^2}{4h} \left(2 - \frac{E_g}{\varepsilon_F} \right) \\
&= \frac{e^2 E_g}{4h} \left(\frac{1}{\varepsilon_F} - \frac{1}{\varepsilon_F + \delta\varepsilon} \right) \\
&= \frac{e^2 E_g}{4h\varepsilon_F^2} \delta\varepsilon
\end{aligned}$$

where the denominator $\varepsilon_F(\varepsilon_F + \delta\varepsilon) \approx \varepsilon_F^2$. Recalling that the carrier density in the conduction band $n_c(\varepsilon_F) = k_F^2/4\pi$, and using Eq. C.1, we find that

$$n_c(\varepsilon_F) = \frac{\varepsilon_F^2 - \left(\frac{E_g}{2}\right)^2}{4\pi a^2 t^2}$$

The difference in carrier densities between the K and K' valleys

$\delta n_c = \delta n_c(\varepsilon_F + \delta\varepsilon) - \delta n_c(\varepsilon_F)$, so

$$\delta n_c = \frac{2\varepsilon_F \delta\varepsilon + \delta\varepsilon^2}{4\pi a^2 t^2} \delta\varepsilon$$

For $\delta\varepsilon \ll \varepsilon_F$, we find

$$\delta\varepsilon = \frac{2\pi a^2 t^2}{\varepsilon_F} \delta n_c$$

allowing us to write $\delta\sigma_c^{in}$ in terms of the carrier density imbalance:

$$\delta\sigma_c^{in} = \frac{e^2 E_g \pi a^2 t^2}{h 2\varepsilon_F^3} \delta n_c$$

Recalling that $at = \hbar v_F$ and that $\frac{1}{2} m_b v_F^2 = \varepsilon_F$, we have

$$\delta\sigma_c^{in} = \frac{e^2 E_g \pi \hbar^2}{h 2m_b \varepsilon_F^2} \delta n_c$$

However, $\varepsilon_F \approx E_g/2$, so

$$\delta\sigma_c^{in} = \frac{e^2 2\pi \hbar^2}{h m_b E_g} \delta n_c$$

Returning to the issue of the total anomalous Hall conductivity, and recalling that, according to Nagaosa *et al.* (2010)¹, $\delta\sigma^{sj} = -2\delta\sigma_c^{in}$, we find

$$\begin{aligned} \delta\sigma_H^v &= \delta\sigma_c^{in} + \delta\sigma^{sj} \\ \delta\sigma_H^v &= -\frac{e^2 2\pi \hbar^2}{h m_b E_g} \delta n_c \end{aligned} \quad (\text{C.6})$$

Equation C.6, then, is Eq. 2.10 presented in Sec. 2.8 and which is compared to experimental data in Fig. 3.12.

References

1. Nagaosa, N., Sinova, J., Onoda, S., MacDonald, A. H. & Ong, N. P. Anomalous Hall effect. *Rev. Mod. Phys.* **82**, 1539–1592 (2010).
2. Olsen, T. & Souza, I. Valley Hall effect in disordered monolayer MoS₂ from first principles. *Phys. Rev. B* **92**, 125146 (2015).
3. Sinitsyn, N. A., MacDonald, A. H., Jungwirth, T., Dugaev, V. K. & Sinova, J. Anomalous Hall effect in a two-dimensional Dirac band: The link between the Kubo-Streda formula and the semiclassical Boltzmann equation approach. *Phys. Rev. B* **75**, 045315 (2007).

4. Xiao, D., Liu, G.-B., Feng, W., Xu, X. & Yao, W. Coupled Spin and Valley Physics in Monolayers of MoS₂ and Other Group-VI Dichalcogenides. *Phys. Rev. Lett.* **108**, 196802 (2012).
5. Cao, T. *et al.* Valley-selective circular dichroism of monolayer molybdenum disulphide. *Nature Communications* **3**, 887 (2012).

BIBLIOGRAPHY

- Allwood, D. A., Xiong, G., Cooke, M. D., & Cowburn, R. P. (2003). Magneto-optical Kerr effect analysis of magnetic nanostructures. *Journal of Physics D: Applied Physics*, *36*(18), 2175–2182.
- Andrew, R. C., Mapasha, R. E., Ukpong, A. M., & Chetty, N. (2012). Mechanical properties of graphene and boronitrene. *Physical Review B*, *85*, 125428.
- Aronovitz, J. A., & Lubensky, T. C. (1988). Fluctuations of Solid Membranes. *Physical Review Letters*, *60*(25), 2634–2637.
- Ashcroft, N. W., & Mermin, N. D. (1976). *Solid State Physics*. Brooks/Cole, Cengage Learning.
- Bae, J., Ouchi, T., & Hayward, R. C. (2015). Measuring the Elastic Modulus of Thin Polymer Sheets by Elastocapillary Bending. *ACS Applied Materials & Interfaces*, *7*(27), 14734–14742.
- Baughner, B. W. H., Churchill, H. O. H., Yang, Y., & Jarillo-Herrero, P. (2013). Intrinsic Electronic Transport Properties of High-Quality Monolayer and Bilayer MoS₂. *Nano Letters*, *13*(9), 4212–4216.
- Berger, L. (1970). Side-jump mechanism for the Hall effect of ferromagnets. *Physical Review B*, *2*(11), 4559–4566.
- Berry, M. V. (1984). Quantal Phase Factors Accompanying Adiabatic Changes. *Proceedings of the Royal Society A: Mathematical, Physical and Engineering Sciences*, *392*(1802), 45–57.
- Blakslee, O. L., Proctor, D. G., Seldin, E. J., Spence, G. B., & Weng, T. (1970). Elastic Constants of Compression-Annealed Pyrolytic Graphite. *Journal of Applied Physics*, *41*(8), 3373–3382.

- Blees, Melina K., Barnard, A. W., Rose, P. A., Roberts, S. P., McGill, K. L., Huang, P. Y., ... McEuen, P. L. (2015). Graphene kirigami. *Nature*, 524(7564), 204–207.
- Blees, Melina Katherine. (2015). *Graphene as atomic paper: From bending stiffness to mechanical metamaterials*. Cornell University.
- Bonaccorso, F., Sun, Z., Hasan, T., & Ferrari, A. C. (2010). Graphene photonics and optoelectronics. *Nature Photonics*, 4(9), 611–622.
- Boncheva, M., Andreev, S. A., Mahadevan, L., Winkleman, A., Reichman, D. R., Prentiss, M. G., ... Whitesides, G. M. (2005). Magnetic self-assembly of three-dimensional surfaces from planar sheets. *Proceedings of the National Academy of Sciences of the United States of America*, 102(11), 3924–3929.
- Boncheva, M., Bruzewicz, D. A., & Whitesides, G. M. (2003). Millimeter-scale self-assembly and its applications. *Pure and Applied Chemistry*, 75(5), 621–630.
- Braghin, F. L., & Hasselmann, N. (2010). Thermal fluctuations of free-standing graphene. *Physical Review B*, 82, 035407.
- Cao, T., Wang, G., Han, W., Ye, H., Zhu, C., Shi, J., ... Feng, J. (2012). Valley-selective circular dichroism of monolayer molybdenum disulphide. *Nature Communications*, 3, 887.
- Castro Neto, A. H., Guinea, F., Peres, N. M. R., Novoselov, K. S., & Geim, A. K. (2009). The electronic properties of graphene. *Reviews of Modern Physics*, 81(1), 109–162.
- Checkelsky, J. G., Lee, M., Morosan, E., Cava, R. J., & Ong, N. P. (2008). Anomalous Hall effect and magnetoresistance in the layered ferromagnet $\text{Fe}_{1/4}\text{TaS}_2$: The inelastic regime. *Physical Review B*, 77, 014433.

- Chen, L., Wang, X., Wen, W., & Li, Z. (2010). Critical droplet volume for spontaneous capillary wrapping. *Applied Physics Letters*, *97*(12), 124103.
- Cleveland, J. P., Manne, S., Bocek, D., & Hansma, P. K. (1993). A nondestructive method for determining the spring constant of cantilevers for scanning force microscopy. *Review of Scientific Instruments*, *64*(2), 403–405.
- Davami, K., Zhao, L., Lu, E., Cortes, J., Lin, C., Lilley, D. E., ... Bargatin, I. (2015). Ultralight shape-recovering plate mechanical metamaterials. *Nature Communications*, *6*, 10019.
- de Groot, B. G. (1999). A simple model for Brownian motion leading to the Langevin equation. *American Journal of Physics*, *67*(12), 1248–1252.
- Fasolino, A., Los, J. H., & Katsnelson, M. I. (2007). Intrinsic ripples in graphene. *Nature Materials*, *6*(11), 858–861.
- Ferrari, A. C., Meyer, J. C., Scardaci, V., Casiraghi, C., Lazzeri, M., Mauri, F., ... Geim, A. K. (2006). Raman Spectrum of Graphene and Graphene Layers. *Physical Review Letters*, *97*, 187401.
- Föppl, A. (1897). *Vorlesungen über technische Mechanik*. Leipzig, B. G. Teubner. Retrieved from <http://archive.org/details/vorlesungenbert26fpgoog>
- Georgiou, T., Britnell, L., Blake, P., Gorbachev, R. V., Gholinia, A., Geim, A. K., ... Novoselov, K. S. (2011). Graphene bubbles with controllable curvature. *Applied Physics Letters*, *99*(9), 093103.
- Geraldi, N. R., Ouali, F. F., Morris, R. H., McHale, G., & Newton, M. I. (2013). Capillary origami and superhydrophobic membrane surfaces. *Applied Physics Letters*, *102*(21), 214104.

- Gorbachev, R. V., Song, J. C. W., Yu, G. L., Kretinin, A. V., Withers, F., Cao, Y., ... Geim, A. K. (2014). Detecting topological currents in graphene superlattices. *Science*, 346(6208), 448–451.
- Hall, E. H. (1879). On a New Action of the Magnet on Electric Currents. *American Journal of Mathematics*, 2(3), 287.
- Hall, E. H. (1880). XXXVIII On the new action of magnetism on a permanent electric current. *Philosophical Magazine Series 5*, 10(63), 301–328.
- Hall, E. H. (1881). XVIII On the “Rotational Coefficient” in nickel and cobalt. *Philosophical Magazine Series 5*, 12(74), 157–172.
- Huang, J., Juskiewicz, M., De Jeu, W. H., Cerda, E., Emrick, T., Menon, N., & Russell, T. P. (2007). Capillary wrinkling of floating thin polymer films. *Science*, 317(5838), 650–653.
- Huttenlocher, D. P., Klanderman, G. A., & Rucklidge, W. J. (1993). Comparing images using the Hausdorff distance. *IEEE Transactions on Pattern Analysis and Machine Intelligence*, 15(9), 850–863.
- Jiang, J.-W., Qi, Z., Park, H. S., & Rabczuk, T. (2013). Elastic bending modulus of single-layer molybdenum disulfide (MoS_2): finite thickness effect. *Nanotechnology*, 24(43), 435705.
- Kang, K., Xie, S., Huang, L., Han, Y., Huang, P. Y., Mak, K. F., ... Park, J. (2015). High-mobility three-atom-thick semiconducting films with wafer-scale homogeneity. *Nature*, 520(7549), 656–660.
- Kim, J., Jin, C., Chen, B., Cai, H., Zhao, T., Lee, P., ... Wang, F. (2017). Observation of ultralong valley lifetime in WSe_2 - MoS_2 heterostructures. *Science Advances*, 3(7), e1700518.
- King, H., Schroll, R. D., Davidovitch, B., & Menon, N. (2012). Elastic sheet on a liquid drop reveals wrinkling and crumpling as distinct symmetry-

- breaking instabilities. *Proceedings of the National Academy of Sciences*, 109(25), 9716–9720.
- Kioseoglou, G., Hanbicki, A. T., Currie, M., Friedman, A. L., Gunlycke, D., & Jonker, B. T. (2012). Valley polarization and intervalley scattering in monolayer MoS₂. *Applied Physics Letters*, 101(22), 221907.
- Kittel, C. (2005). *Introduction to Solid State Physics* (8th Edition). John Wiley & Sons, Inc.
- Košmrlj, A., & Nelson, D. R. (2013). Mechanical properties of warped membranes. *Physical Review E*, 88, 012136.
- Košmrlj, A., & Nelson, D. R. (2014). Thermal excitations of warped membranes. *Physical Review E*, 89, 022126.
- Kumar, D., Paulsen, J. D., Russell, T. P., & Menon, N. (2018). Wrapping with a splash: High-speed encapsulation with ultrathin sheets. *Science*, 359(6377), 775.
- Kuratsuji, H., & Iida, S. (1985). Effective Action for Adiabatic Process Dynamical Meaning of Berry and Simon's Phase. *Progress of Theoretical Physics*, 74(3), 439–445.
- Landau, L. D., & Lifshitz, E. M. (1986). *Theory of Elasticity*. (E. M. Lifshitz, A. M. Kosevich, & L. P. Pitaevskii, Eds., J. B. Sykes & W. H. Reid, Trans.) (3rd English Edition, Vol. 7). Elsevier.
- Le Doussal, P., & Radzihovsky, L. (1992). Self-consistent theory of polymerized membranes. *Physical Review Letters*, 69(8), 1209.
- Lee, C., Wei, X., Kysar, J. W., & Hone, J. (2008). Measurement of the Elastic Properties and Intrinsic Strength of Monolayer Graphene. *Science*, 321(5887), 385–388.

- Lee, J., Mak, K. F., & Shan, J. (2016). Electrical control of the valley Hall effect in bilayer MoS₂ transistors. *Nature Nanotechnology*, *11*(5), 421–425.
- Li, X., Magnuson, C. W., Venugopal, A., An, J., Suk, J. W., Han, B., ... Ruoff, R. S. (2010). Graphene Films with Large Domain Size by a Two-Step Chemical Vapor Deposition Process. *Nano Letters*, *10*(11), 4328–4334.
- Livermore, C. (n.d.). Course Materials for 6.777J / 2.372J Design and Fabrication of Microelectromechanical Devices, Spring 2007. Retrieved June 27, 2018, from <http://ocw.mit.edu/>
- Lopez-Sanchez, O., Lembke, D., Kayci, M., Radenovic, A., & Kis, A. (2013). Ultrasensitive photodetectors based on monolayer MoS₂. *Nature Nanotechnology*, *8*(7), 497–501.
- Los, J. H., Katsnelson, M. I., Yazyev, O. V., Zakharchenko, K. V., & Fasolino, A. (2009). Scaling properties of flexible membranes from atomistic simulations: Application to graphene. *Physical Review B*, *80*, 121405.
- Mak, K. F., McGill, K. L., Park, J., & McEuen, P. L. (2014). The valley Hall effect in MoS₂ transistors. *Science*, *344*(6191), 1489–1492.
- Mak, Kin Fai, He, K., Shan, J., & Heinz, T. F. (2012). Control of valley polarization in monolayer MoS₂ by optical helicity. *Nature Nanotechnology*, *7*(8), 494–498.
- Mak, Kin Fai, Lee, C., Hone, J., Shan, J., & Heinz, T. F. (2010). Atomically Thin MoS₂: A New Direct-Gap Semiconductor. *Physical Review Letters*, *105*, 136805.
- Marder, M. P. (2010). *Condensed Matter Physics* (2nd ed.). Hoboken, NJ: John Wiley & Sons, Inc.

- McHale, G., Newton, M. I., Shirtcliffe, N. J., & Gherali, N. R. (2011). Capillary origami: superhydrophobic ribbon surfaces and liquid marbles. *Beilstein Journal of Nanotechnology*, 2, 145–151.
- Meyer, J. C., Geim, A. K., Katsnelson, M. I., Novoselov, K. S., Booth, T. J., & Roth, S. (2007). The structure of suspended graphene sheets. *Nature*, 446(7131), 60–63.
- Miskin, M. Z., Dorsey, K. J., Bircan, B., Han, Y., Muller, D. A., McEuen, P. L., & Cohen, I. (2018). Graphene-based bimorphs for micron-sized, autonomous origami machines. *Proceedings of the National Academy of Sciences*, 201712889.
- Miskin, M. Z., Sun, C., Cohen, I., Dichtel, W. R., & McEuen, P. L. (2018). Measuring and Manipulating the Adhesion of Graphene. *Nano Letters*, 18(1), 449–454.
- Nagaosa, N., Sinova, J., Onoda, S., MacDonald, A. H., & Ong, N. P. (2010). Anomalous Hall effect. *Reviews of Modern Physics*, 82(2), 1539–1592.
- Nelson, D. R., & Peliti, L. (1987). Fluctuations in membranes with crystalline and hexatic order. *Journal de Physique*, 48(7), 1085–1092.
- Nicklow, R., Wakabayashi, N., & Smith, H. G. (1972). Lattice Dynamics of Pyrolytic Graphite. *Physical Review B*, 5(12), 4951–4962.
- Novoselov, K. S., Jiang, D., Schedin, F., Booth, T. J., Khotkevich, V. V., Morozov, S. V., & Geim, A. K. (2005). Two-dimensional atomic crystals. *Proceedings of the National Academy of Sciences of the United States of America*, 102(30), 10451–10453.
- Olsen, T., & Souza, I. (2015). Valley Hall effect in disordered monolayer MoS₂ from first principles. *Physical Review B*, 92, 125146.

- Paulsen, J. D., Démercy, V., Santangelo, C. D., Russell, T. P., Davidovitch, B., & Menon, N. (2015). Optimal wrapping of liquid droplets with ultrathin sheets. *Nature Materials*, *14*(12), 1206–1209.
- Piñeirua, M., Bico, J., & Roman, B. (2010). Capillary origami controlled by an electric field. *Soft Matter*, *6*(18), 4491.
- PMMA. (n.d.). Retrieved June 1, 2018, from <http://www.mit.edu/~6.777/matprops/pmma.htm>
- Py, C., Reverdy, P., Doppler, L., Bico, J., Roman, B., & Baroud, C. N. (2007). Capillary origami: spontaneous wrapping of a droplet with an elastic sheet. arXiv:cond-mat/0611682 [cond-mat.soft].
- Py, Charlotte, Reverdy, P., Doppler, L., Bico, J., Roman, B., & Baroud, C. N. (2007). Capillary Origami: Spontaneous Wrapping of a Droplet with an Elastic Sheet. *Physical Review Letters*, *98*, 156103.
- Qiu, H., Pan, L., Yao, Z., Li, J., Shi, Y., & Wang, X. (2012). Electrical characterization of back-gated bi-layer MoS₂ field-effect transistors and the effect of ambient on their performances. *Applied Physics Letters*, *100*(12), 123104.
- Radisavljevic, B., Radenovic, A., Brivio, J., Giacometti, V., & Kis, A. (2011). Single-layer MoS₂ transistors. *Nature Nanotechnology*, *6*(3), 147–150.
- Raj, K., Moskowitz, B., & Casciari, R. (1995). Advances in ferrofluid technology. *Journal of Magnetism and Magnetic Materials*, *149*(1–2), 174–180.
- Roldán, R., Fasolino, A., Zakharchenko, K. V., & Katsnelson, M. I. (2011). Suppression of anharmonicities in crystalline membranes by external strain. *Physical Review B*, *83*(17), 174104.
- Sallen, G., Bouet, L., Marie, X., Wang, G., Zhu, C. R., Han, W. P., ... Urbaszek, B. (2012). Robust optical emission polarization in MoS₂

- monolayers through selective valley excitation. *Physical Review B*, 86(8), 081301.
- Sánchez-Portal, D., Artacho, E., Soler, J. M., Rubio, A., & Ordejón, P. (1999). Ab initio structural, elastic, and vibrational properties of carbon nanotubes. *Physical Review B*, 59(19), 12678–12688.
- Sengupta, P., Tan, Y., Klimeck, G., & Shi, J. (2017). Low-temperature thermal transport and thermopower of monolayer transition metal dichalcogenide semiconductors. *Journal of Physics: Condensed Matter*, 29(40), 405701.
- Sinitsyn, N. A., MacDonald, A. H., Jungwirth, T., Dugaev, V. K., & Sinova, J. (2007). Anomalous Hall effect in a two-dimensional Dirac band: The link between the Kubo-Streda formula and the semiclassical Boltzmann equation approach. *Physical Review B*, 75, 045315.
- Smit, J. (1958). The spontaneous Hall effect in ferromagnetics II. *Physica*, 24(1–5), 39–51.
- Song, T. T., Yang, M., Chai, J. W., Callsen, M., Zhou, J., Yang, T., ... Wang, S. J. (2016). The stability of aluminium oxide monolayer and its interface with two-dimensional materials. *Scientific Reports*, 6, 29221.
- Splendiani, A., Sun, L., Zhang, Y., Li, T., Kim, J., Chim, C.-Y., ... Wang, F. (2010). Emerging Photoluminescence in Monolayer MoS₂. *Nano Letters*, 10(4), 1271–1275.
- Sundaram, G., & Niu, Q. (1999). Wave-packet dynamics in slowly perturbed crystals: Gradient corrections and Berry-phase effects. *Physical Review B*, 59(23), 14915.
- te Velthuis, A. J. W., Kerssemakers, J. W. J., Lipfert, J., & Dekker, N. H. (2010). Quantitative Guidelines for Force Calibration through Spectral Analysis of Magnetic Tweezers Data. *Biophysical Journal*, 99(4), 1292–1302.

- van der Pauw, L. J. (1958). A method of measuring the resistivity and Hall coefficient on lamellae of arbitrary shape. *Philips Technical Review*, 20(8), 220–224.
- Velasco, S. (1985). On the Brownian motion of a harmonically bound particle and the theory of a Wiener process. *European Journal of Physics*, 6(4), 259–265.
- Von Kármán, T. (1910). *Festigkeitsprobleme im maschinenbau*. Leipzig.
- Wang, M. C., & Uhlenbeck, G. E. (1945). On the Theory of the Brownian Motion II. *Reviews of Modern Physics*, 17(2–3), 323–342.
- Wang, Q. H., Kalantar-Zadeh, K., Kis, A., Coleman, J. N., & Strano, M. S. (2012). Electronics and optoelectronics of two-dimensional transition metal dichalcogenides. *Nature Nanotechnology*, 7(11), 699–712.
- Wang, W. L., Bhandari, S., Yi, W., Bell, D. C., Westervelt, R., & Kaxiras, E. (2012). Direct Imaging of Atomic-Scale Ripples in Few-Layer Graphene. *Nano Letters*, 12(5), 2278–2282.
- Wu, S., Ross, J. S., Liu, G.-B., Aivazian, G., Jones, A., Fei, Z., ... Xu, X. (2013). Electrical tuning of valley magnetic moment through symmetry control in bilayer MoS₂. *Nature Physics*, 9(3), 149–153.
- Xiao, D., Chang, M.-C., & Niu, Q. (2010). Berry phase effects on electronic properties. *Reviews of Modern Physics*, 82(3), 1959–2007.
- Xiao, D., Liu, G.-B., Feng, W., Xu, X., & Yao, W. (2012). Coupled Spin and Valley Physics in Monolayers of MoS₂ and Other Group-VI Dichalcogenides. *Physical Review Letters*, 108, 196802.
- Xiao, D., Yao, W., & Niu, Q. (2007). Valley-Contrasting Physics in Graphene: Magnetic Moment and Topological Transport. *Physical Review Letters*, 99, 236809.

Zeng, H., Dai, J., Yao, W., Xiao, D., & Cui, X. (2012). Valley polarization in MoS₂ monolayers by optical pumping. *Nature Nanotechnology*, 7(8), 490–493.

Zhao, C. Y., & Zhang, G. H. (2011). Review on microencapsulated phase change materials (MEPCMs): Fabrication, characterization and applications. *Renewable and Sustainable Energy Reviews*, 15(8), 3813–3832.